DENSITY AND TEMPERATURE IN QUANTUM NUCLEAR SYSTEMS

A Dissertation

by

HUA ZHENG

Submitted to the Office of Graduate and Professional Studies of
Texas A&M University
in partial fulfillment of the requirements for the degree of

DOCTOR OF PHILOSOPHY

Chair of Committee,	Robert Tribble
Co-Chair of Committee,	Aldo Bonasera
Committee Members,	Joseph Natowitz
	Che-Ming Ko
	Saskia Mioduszewski
Head of Department,	George R. Welch

December 2014

Major Subject: Physics

ABSTRACT

One of the goals of nuclear physics is to study the Equation of State (EOS) of nuclear matter. In order to create the nuclear matter at different densities, we collide different nuclei and detect the fragments after the collisions with different beam energies in the laboratory. Then we extract information about finite nuclei by analyzing the collected data with different assumptions.

As we know, quantum effects play an important role in many systems: the Cosmic Microwave Background (CMB) radiation, the specific heat of different metals, the suppression of density fluctuations in a trapped Fermi gas, the enhancement of density fluctuations in a trapped Bose gas, the observation of Fermi pressure in trapped mixed Fermi and Bose gases, etc. The nucleus is a quantum many body system made of strongly interacting fermions, protons and neutrons (nucleons). Therefore, we are dealing with fermions and bosons in the nucleus-nucleus collisions. It is clear that we need to take into account the genuine quantum nature of particles when we extract the physical quantities for the EOS. In the past, some methods have employed the classical limit of low density and high temperature, e.g. double ratio thermometer, while other methods (e.g. two particle correlation) implement some quantum effects but they are only able to calculate one physical quantity, i.e. density ρ or temperature T.

We would like to develop a method which takes into account the quantum nature of particles to extract the temperature and density of nuclear matter created in heavy-ion collisions. In this dissertation, we propose a new thermometer which includes quantum effects as manifested in quadrupole momentum fluctuations and multiplicity fluctuations of the detected particles. In the same framework, we are

able to calculate the density of the studied particles. To test our method, we use the Constrained Molecular Dynamics (CoMD) model, which incorporates the Pauli principle, and we simulate the $^{40}Ca + ^{40}Ca$ collisions at different beam energies at impact parameter $b = 1$ fm up to 1000 fm/c. Later, we apply our method to do data analysis and extract the temperatures and densities for fermions and bosons respectively. The Fermi quenching for fermions is found in the simulation data. It has been confirmed in different experimental data. We also studied the possible Bose-Einstein condensate (BEC) for bosons in the same framework with CoMD and CoMD$_\alpha$ which includes the boson correlations. Comparing the results with neutron case, we can see that the Coulomb effects play a role in the data analysis. To explore our method even further, we introduce the Coulomb correction for charged particles (both fermions and bosons). A method borrowed from electron scattering was adopted and applied to classical as well as quantum systems. In the model calculations, it was observed that when taking into account those effects, the T of p and n (as well as composite fermions in the classical case) are very similar, while the densities are not affected by the corrections. But for bosons, the temperatures and densities are very similar to the neutron case.

ACKNOWLEDGEMENTS

I am profoundly grateful to conduct my graduate studies at the Cyclotron Institute Texas A&M University. People are awesome here.

I would like to thank my supervisor, Prof. Aldo Bonasera, for his patience, guidance, support and dedication during my research and writing of this dissertation. He has set an example for me as a scientist. He is not only my supervisor, but also one of my best friends. He will continue playing an important role in my life. I look forward to our continuing collaboration.

I would like to express my gratitude to Prof. Joseph Natowitz and all the members in his group. They allowed me to get involved to their experiments and group meetings. They taught me how the experiments work and showed me how the raw data becomes real data. I also learned a lot from the group meeting discussions. I, a theorist, have the privileges that many theorists don't have.

Prof. Robert Tribble, Prof. Che-Ming Ko and Prof. Saskia Mioduszewski deserve my special thanks as my dissertation committee members. Prof. Rainer Fries also deserves my special thanks for his kindness.

I would like to thank my family and girlfriend for their love, support and encouragement.

I also would like to thank Dr. Gianluca Giuliani, Dr. Justin Mabiala, Dr. Xingbo Zhao and Dr. Meirong Huang for their fruitful discussions.

NOMENCLATURE

E	Total energy
E/A	Energy per nucleon
P	Pressure
T	Temperature
ρ	Number density
ϵ	Energy density
μ	Chemical potential
p_f	Fermi momentum
p_{f0}	Fermi momentum at ρ_0
ε_f	Fermi energy
ε_{f0}	Fermi energy at ρ_0

TABLE OF CONTENTS

LIST OF FIGURES

FIGURE Page

LIST OF TABLES

TABLE Page

1. INTRODUCTION*

1.1 Nuclear Equation of State

Many aspects of the Nuclear Equation of State (NEOS) have been studied in great detail in the past years. Finite nuclei resemble classical liquid drops, the crucial difference is that the nucleus in its ground state, or at zero temperature, does not 'solidify' in the same way as a drop at low temperatures [1, 2, 3, 4, 5, 6, 7]. This is due to the quantum nature of the nucleus: more specifically its constituents, neutrons (n) and protons (p), are fermions. They obey the Pauli principle which forbids two identical fermions, two protons with the same spin or two neutrons with the same spin (either both up or both down), to occupy the same quantum state. Thus at zero temperature, two or more fermions cannot be at rest (a solid) when confined in a finite volume. In intuitive terms, we can express the Pauli principle by saying that a phase space of size $h^3 = (2\pi\hbar)^3$ can at most contain $g = (2s+1)(2\tau+1)$ nucleons, where $\hbar = 197.3$ MeV·fm is the Planck constant, s and τ are the spin and isospin of the considered fermion respectively. Thus a volume $V = \frac{4\pi}{3}R^3$ in coordinate space and $V_p = \frac{4\pi}{3}p_f^3$ in momentum space can contain $\frac{A}{g}$ nucleons, i.e.,

$$\frac{\frac{4\pi}{3}R^3\frac{4\pi}{3}p_f^3}{h^3} = \frac{A}{g}. \tag{1.1}$$

Since the number density (we will use density to mean number density in the following) is given by $\rho = \frac{A}{V}$, where $A = Z + N$ is the total number of nucleons (protons+neutrons), we can easily invert Eq. (1.1) and express the Fermi momentum p_f

*The major part of this chapter is reprinted with permission from "The many facets of the (non-relativistic) Nuclear Equation of State" by G. Giuliani, H. Zheng, A. Bonasera, 2014. Progress in Particle and Nuclear Physics 76, 116-164, Copyright 2014 by Elsevier B.V.

as function of density [4, 8, 9]:

$$p_f = (\frac{3\rho}{4\pi g})^{1/3} h. \tag{1.2}$$

For a nucleus in the ground state $\rho_0 = 0.165$ fm^{-3}, we have $p_f = p_{f0} = 265$ MeV/c. This means that the nucleons in the nucleus are moving, even at zero temperature, with a maximum momentum p_{f0} corresponding to a Fermi energy $\varepsilon_{f0} = \frac{p_{f0}^2}{2m} = 37.5$ MeV. Because of the Fermi energy, the nucleus or any fermionic system would expand if there is no confining external potential or interactions among them. Since the total energy of a nucleus in its ground state is about $E \approx -8A$ MeV and the average kinetic energy from Fermi motion is $\frac{3}{5}\varepsilon_{f0} = 22.5$ MeV/A, then the interaction must account for an average -30 MeV/A, which is a large value. Because of the relentless motion of the nucleons in the nuclei confined to a finite space due to the nuclear force, we can compare the nucleus to a drop or a liquid. Similar to a drop, we can compress it and it will oscillate with a typical frequency known as the Isoscalar Giant Monopole Resonance (ISGMR) [10, 11, 12, 13, 14, 15, 16, 17, 18, 19, 20, 21]:

$$E_{GMR} = 80A^{-1/3} \approx \hbar\sqrt{\frac{K_A}{m\langle r^2\rangle}}, \tag{1.3}$$

where $K_A = K$+surface, Coulomb, symmetry and pairing corrections [21], $\langle r^2\rangle = \frac{3}{5}R^2$, $R = r_0 A^{1/3} = 1.14A^{1/3}$ fm is the average radius of a nucleus of mass A, and K is the nuclear incompressibility which could be derived from the NEOS if known. From experiments and comparison to theory we know that $K = 250 \pm 25$ MeV which implies that the nucleus is quite 'incompressible'. Other nuclear modes such as shape oscillations are possible which the volume of the nucleus remains constant. A significant example of shape oscillation is the Isoscalar Giant Quadrupole Resonance

(ISGQR) mode. Most of these oscillations can be described quantum mechanically, but also, in some limit, using hydrodynamics [16, 22, 23]. An important and maybe crucial feature of nuclei is the fact that its constituents, protons and neutrons, can be described as two different quantum fluids. The fluids might behave as one fluid, such as in the Giant Resonance (GR) cases we briefly discussed before and therefore called Isoscalar GR (ISGR). There are resonances where n and p oscillate against each other and these are called Isovector GR (IVGR). An important example of this is the Isovector Giant Dipole Resonance (IVGDR).

The situations discussed above apply to the nucleus near its ground state. However, important phenomena and objects in the universe, such as the Big-Bang (BB) [24, 25, 26, 27, 28], Supernovae explosions (SN) [28, 29, 30, 31] or Neutron Stars (NS) [28, 31, 32, 33, 34, 35, 36, 37, 38, 39, 40, 41, 42, 43, 44] require the knowledge of the nuclear interactions in extreme situations, this means we need to pin down the NEOS not only near ρ_0 but also at very high or very low densities and/or temperatures. Because of the liquid drop analogy, we expect that if we decrease the density and increase the temperature, the system will become unstable and we will get a "quantum liquid gas" (QLG) phase transition. Not only because the nucleus is a quantum system, but also because it is made of two strongly interacting fluids, thus the "symmetry energy", i.e. the energy of interaction between n and p, will be crucial. At very high densities, even at zero temperature, the nucleons will break into their constituents, quarks and gluons, and we get a state of matter called Quark-Gluon Plasma (QGP). Such a state occurred at the very beginning of the BB [24, 25, 26, 27, 28], at very high temperature, and it might occur in the centeral part of massive stars including neutron stars [28, 31, 32, 33, 34, 35, 36, 37, 38, 39, 40, 41, 42, 43, 44] as well as in heavy-ion collisions at relativistic energies [45, 46, 47, 48, 49, 50]. It is very surprising that slightly changing the symmetry energy we can get at zero temperature

either a QLG phase transition or a QGP by increasing the neutron concentration. In section 1.3, we will assume *for illustration* that at $T = 0$, nuclear matter undergoes a second order phase transition at large concentration of neutrons, such as in a neutron star. Assuming that the ground state symmetry energy $E_{sym} = S(\rho_0) = 32$ MeV (following the literature we use different symbols for the symmetry energy and we hope it will not create confusion) and imposing the relevant conditions on pressure and incompressibility [1, 7, 51], we will get two solutions for the critical density: one solution indicates a QLG and the other a QGP!

It is clear that because of this extreme sensitivity of the NEOS to the symmetry energy, a large effort, both experimental and theoretical, must be pursued [52, 53]. It is naive to think that we can constrain the NEOS through astrophysical observations alone [36, 54, 55], since celestial objects are so complex and observations are rare and sometimes difficult to interpret. The NEOS must also be constrained by laboratory experiments in such a way that our understanding of the universe can steadily improve. New laboratories producing exotic nuclei, either neutron rich or poor, are being built or in operation and this will have a large impact not only on our studies of the NEOS [56] but also on practical applications such as medicine.

Past studies have been rather effective in constraining the isoscalar part of the NEOS and this will be our starting point. We learned a lot from those studies about the NEOS of finite systems. We have some ideas on how to deal with the Coulomb field which is present in nuclei and it is a very important ingredient even though sometimes difficult to treat. Adding to the wealth of information coming from nuclear physics studies, is the fact that the nucleons can form very stable systems some of which are bosons, for instance α particles [57, 58]. In some situations it seems that the nucleus can be thought as formed of α particles. Classic examples are the decay of ^{12}C into 3α, or the α decay of radioactive nuclei. This might suggest that in

some situations nuclei can form a Bose-Einstein condensate (BEC) as proposed by many authors [59, 60, 61, 62, 63, 64, 65, 66, 67, 68, 69]. If these conjectures will be experimentally confirmed, we will have the smallest BEC made at most of $10 \sim 20$ bosons. As we will briefly discuss later, the Coulomb repulsion might help in forming a condensate but it hinders the possibility of having large BEC made of α particles (or deuterons) [70, 71]. Thus the NEOS can be discussed not only in terms of the mixture of n and p, but also as a mixture of bosons and fermions. Clearly, quantum tools must be used to unveil these features. Using classical mechanics and some free parameters can be misleading. BEC or fermion quenching (FQ) [72, 73, 74, 75] are not classical phenomena!

In order to constrain the NEOS, we need to use thermodynamical concepts, therefore we need to create in laboratory equilibrated systems at different temperatures T and densities ρ. This is an important task when dealing with finite systems, not impossible, as we have seen already in the past. Since we would like to study the finest details of the NEOS, we need to determine precisely the source size, i.e. the number of n and p, which means that we have to detect, event by event, $A_s = N_s + Z_s$ and its excitation energy, which requires the measurement of the kinetic energies of the fragments, their charges and masses with good precision. This can be accomplished both by a suitable choice of the colliding nuclei and beam energy, and a careful isolation of the equilibrated source, thus eliminating particles emitted before equilibrium is reached. Information about the neutrons emitted during the process is also crucial and usually hard to have because of experimental difficulties, thus sophisticated models must be implemented. Careful analysis must be able to distinguish between dynamical and equilibrium effects but it is important to stress that dynamical effects also give very important information about the NEOS, usually through comparison to models. These dynamical effects include observed collective flows, π, γ, kaon and

other particle productions which give information about the time development of the reactions and the sensitivity to different ingredients of the NEOS. In this dissertation we will not discuss the dynamical effects and we will refer to the literature to have more pieces of the NEOS puzzle [8, 76, 77, 78, 79, 80, 81, 82, 83, 84, 85, 86, 87, 88, 89].

Once an isolated and approximately equilibrated hot source is determined, there are different methods proposed in the literature to obtain the temperature T, the density ρ, the pressure P, the entropy S and the energy density ϵ. Those methods could be based on classical or quantum assumptions. We know that the nucleus is a quantum system, but, in some conditions, classical approximations could be valid or simply used as a guidance. At the end of the day the validity of classical approximations must be confirmed by the quantum treatment. The reason why the classical approximation might give a good description of nuclear phenomena is due to the use of parameters, fitted to experiments, but also to the fact that densities are rather low and temperatures high, i.e. high entropy, where classical approximations are valid. Of course we might claim that we have reached a good understanding of nuclear phenomena only when we can describe them through quantum mechanics.

The starting point of the NEOS is the understanding of the nucleus in its ground state. Usually, we study the NEOS as a function of density ρ. Sometimes, it is also written as a function of Fermi momentum p_f. Before we go into details, we derive the general expressions for the basic quantities (pressure P, incompressibility K and speed of sound $\frac{v}{c}$) related to the NEOS.

1.1.1 Pressure P

From the first law of thermodynamics [1, 7, 51], we know

$$dE = TdS - PdV + \mu dN, \tag{1.4}$$

where T is the temperature, P is the pressure and μ is the chemical potential. From Eq. (1.4) one can obtain

$$\begin{aligned} P &= -\left(\frac{\partial E}{\partial V}\right)_{S,N} \\ &= -\left(\frac{\partial E}{\partial \rho}\frac{\partial \rho}{\partial V}\right)_{S,N} \\ &= -N\left[\frac{\partial (E/A)_{rel}}{\partial \rho}\frac{\partial \rho}{\partial V}\right]_{S,N}. \end{aligned} \tag{1.5}$$

The subscript 'rel' means relativistic. According to the definition of density $\rho = \frac{N}{V}$, one can obtain

$$\left(\frac{\partial \rho}{\partial V}\right)_{S,N} = -\left(\frac{N}{V^2}\right)_{S,N}. \tag{1.6}$$

Substituting Eq. (1.6) into Eq. (1.5), the pressure is

$$\begin{aligned} P &= -N\left[\frac{\partial (E/A)_{rel}}{\partial \rho}\frac{\partial \rho}{\partial V}\right]_{S,N} \\ &= \left[\left(\frac{N}{V}\right)^2 \frac{\partial (E/A)_{rel}}{\partial \rho}\right]_{S,N} \\ &= \left[\rho^2 \frac{\partial (E/A)_{rel}}{\partial \rho}\right]_{S,N} \\ &= \left\{\rho^2 \frac{\partial \left[(E/A)_{nonrel} + m\right]}{\partial \rho}\right\}_{S,N} \\ &= \left[\rho^2 \frac{\partial (E/A)_{nonrel}}{\partial \rho}\right]_{S,N}. \end{aligned} \tag{1.7}$$

The subscript 'nonrel' means nonrelativisitic. We have used the relation $(E/A)_{rel} = (E/A)_{nonrel} + m$ in Eq. (1.7) which is often adopted in literature and reasonable in low energy nuclear physics.

1.1.2 *Incompressibility K*

The original definition of incompressibility K (or sometimes called compressibility in literature) is [90]

$$K = k_f^2 \frac{\partial^2 (E/A)_{rel}}{\partial k_f^2}\bigg|_{k_f=k_{f0}} = p_f^2 \frac{\partial^2 (E/A)_{rel}}{\partial p_f^2}\bigg|_{p_f=p_{f0}}, \tag{1.8}$$

where $p_f = \hbar k_f$ is Fermi momentum at density ρ. p_{f0} is the Fermi momentum at normal density ρ_0 where the pressure $P|_{\rho=\rho_0} = 0$. Since $(E/A)_{rel}$ is a function of density, we need to apply the derivative chain rule to Eq. (1.8) in order to calculate K. For an ideal Fermi gas, we have

$$\rho = \frac{g}{6\pi^2\hbar^3} p_f^3 = w p_f^3, \tag{1.9}$$

where $w = \frac{g}{6\pi^2\hbar^3}$. The detailed derivation of this equation is given in appendix A. We can obtain the same result from Eq. (1.1) with a simple calculation. Therefore

$$\begin{aligned}
K &= p_f^2 \frac{\partial^2 (E/A)_{rel}}{\partial p_f^2}\bigg|_{p_f=p_{f0}} \\
&= p_f^2 \frac{\partial}{\partial p_f}\left[\frac{\partial (E/A)_{rel}}{\partial \rho}\frac{\partial \rho}{\partial p_f}\right] \\
&= p_f^2 \frac{\partial}{\partial p_f}\left[\frac{\partial (E/A)_{rel}}{\partial \rho} 3 w p_f^2\right] \\
&= 3 w p_f^4 \frac{\partial}{\partial p_f}\left[\frac{\partial (E/A)_{rel}}{\partial \rho}\right] + p_f^2 \frac{\partial (E/A)_{rel}}{\partial \rho} 6 w p_f \\
&= 3 w p_f^4 \frac{\partial}{\partial \rho}\left[\frac{\partial (E/A)_{rel}}{\partial \rho}\right]\frac{\partial \rho}{\partial p_f} + 6\rho \frac{\partial (E/A)_{rel}}{\partial \rho} \\
&= 9 w^2 p_f^6 \frac{\partial^2 (E/A)_{rel}}{\partial \rho^2} + 6\rho \frac{\partial (E/A)_{rel}}{\partial \rho} \\
&= 9\rho^2 \frac{\partial^2 (E/A)_{rel}}{\partial \rho^2} + 6\rho \frac{\partial (E/A)_{rel}}{\partial \rho}
\end{aligned}$$

$$
\begin{aligned}
&= \Big[9\rho^2\frac{\partial^2(E/A)_{rel}}{\partial\rho^2} + 18\rho\frac{\partial(E/A)_{rel}}{\partial\rho}\Big]\Big|_{\rho=\rho_0} \\
&= 9\frac{\partial}{\partial\rho}[\rho^2\frac{\partial(E/A)_{rel}}{\partial\rho}]\Big|_{\rho=\rho_0} \\
&= 9\frac{\partial}{\partial\rho}[\rho^2\frac{\partial(E/A)_{nonrel}}{\partial\rho}]\Big|_{\rho=\rho_0} \\
&= 9\frac{\partial P}{\partial\rho}\Big|_{\rho=\rho_0}. \qquad (1.10)
\end{aligned}
$$

We have applied the condition

$$\rho\frac{\partial(E/A)_{rel}}{\partial\rho}\Big|_{\rho=\rho_0} = 0, \qquad (1.11)$$

in Eq. (1.10) since we have

$$P|_{\rho=\rho_0} = \rho^2\frac{\partial(E/A)_{rel}}{\partial\rho}\Big|_{\rho=\rho_0} = 0. \qquad (1.12)$$

The often used definition of incompressibility K in literature is

$$K = 9\frac{\partial P}{\partial\rho}\Big|_{\rho=\rho_0}. \qquad (1.13)$$

1.1.3 Speed of Sound $\frac{v}{c}$

The definition of speed of sound is [22]

$$\frac{v}{c} = \sqrt{\frac{\partial P}{\partial\epsilon}}, \qquad (1.14)$$

where ϵ is energy density,

$$\epsilon = \frac{E}{V} = \frac{N}{V}(E/A)_{rel} = \rho(E/A)_{rel} = \rho[(E/A)_{nonrel} + m]. \qquad (1.15)$$

Therefore the speed of sound becomes

$$\begin{aligned}
\frac{v}{c} &= \sqrt{\frac{\partial P}{\partial \epsilon}} \\
&= \sqrt{\left(\frac{\partial P}{\partial \rho}\right) \Big/ \left(\frac{\partial \epsilon}{\partial \rho}\right)} \\
&= \sqrt{\frac{1}{\frac{\partial[\rho(E/A)_{rel}]}{\partial \rho}} \frac{\partial P}{\partial \rho}} \qquad (1.16) \\
&= \sqrt{\frac{1}{\frac{\partial[\rho(E/A)_{nonrel}]}{\partial \rho} + m} \frac{\partial P}{\partial \rho}}. \qquad (1.17)
\end{aligned}$$

Eqs. (1.16, 1.17) are used for the relativistic and the nonrelativistic case respectively. For the nonrelativistic case, when the density is low, the condition $\frac{\partial[\rho(E/A)_{nonrel}]}{\partial \rho} << m$ is satisfied, then

$$\frac{v}{c} \approx \sqrt{\frac{1}{m} \frac{\partial P}{\partial \rho}}. \qquad (1.18)$$

The speed of light is the velocity limit. Therefore, the speed of sound $\frac{v}{c}$ should be less than 1 which can be used as one of the criteria to check the validity of NEOS.

1.2 Pressure, Incompressibility and Speed of Sound of Free Fermi Gas at $T = 0$

We derive the expressions for pressure, incompressibility and speed of sound of free Fermi gas at $T = 0$ as an example. For completeness, we consider the non-relativistic free Fermi gas, the relativistic free Fermi gas and the ultra-relativistic free Fermi gas. The detailed derivation is reported in appendix A. We just show the results here.

1. Non-relativistic free Fermi gas (mixed protons and neutrons with same concentration)

$$P = \frac{2}{3} \rho_0 \bar{\varepsilon}_{f0} \tilde{\rho}^{\frac{5}{3}}, \qquad (1.19)$$

$$K = 10\bar{\varepsilon}_{f0}\tilde{\rho}^{\frac{2}{3}}\Big|_{\rho=\rho_0}, \tag{1.20}$$

$$\frac{v}{c} = \sqrt{\frac{\frac{10}{9}\bar{\varepsilon}_{f0}\tilde{\rho}^{\frac{2}{3}}}{\frac{5}{3}\bar{\varepsilon}_{f0}\tilde{\rho}^{\frac{2}{3}} + m}}, \tag{1.21}$$

where $\bar{\varepsilon}_{f0} = 22.5$ MeV is the average Fermi energy at normal density ρ_0, $\tilde{\rho} = \frac{\rho}{\rho_0}$ is the reduced density and m is the mass of nucleon.

2. Relativistic free Fermi gas

$$P = \frac{g}{16\pi^2\hbar^3}\left[p_f(\frac{2}{3}p_f^2 - m^2)\sqrt{p_f^2 + m^2} + m^4 \ln\frac{p_f + \sqrt{m^2 + p_f^2}}{m}\right], \tag{1.22}$$

$$K = 3\frac{p_f^2}{\sqrt{p_f^2 + m^2}}\Bigg|_{p_f=p_{f0}}, \tag{1.23}$$

$$\frac{v}{c} = \sqrt{\frac{p_f^2}{3(p_f^2 + m^2)}}, \tag{1.24}$$

where g is the degeneracy of the free Fermi gas.

3. Ultra-relativistic free Fermi gas

$$P = \frac{g}{24\pi^2\hbar^3}p_f^4, \tag{1.25}$$

$$K = 3p_f|_{p_f=p_{f0}}, \tag{1.26}$$

$$\frac{v}{c} = \sqrt{\frac{1}{3}}. \tag{1.27}$$

1.3 The Nuclear Equation of State at Zero Temperature

1.3.1 Momentum Independent NEOS

For a system interacting through two body forces having a short-range repulsion and a longer-range attraction, the EOS resembles a Van Der Waals one. This is indeed the case for nuclear matter [8, 78, 79, 91, 92]. With increasing density, the effects of N-body correlations become more and more important. This is especially true near a phase transition. Furthermore, nucleons are not elementary particles but they are made of quarks and gluons, thus N-body forces are expected to be stronger at high densities where the nucleon wave functions strongly overlap.

The results discussed in the previous sections refer to properties of nuclei in their ground state or at small excitation energies. In nuclear astrophysics it is necessary to know nuclear properties not only at different densities, but at different temperatures as well. We have already seen the density dependence of the energy of a nucleus in the simple Fermi gas model. On similar grounds we need to introduce the density dependence, the momentum dependence of the interactions among nucleons and we need to distinguish between protons and neutrons. A simple approximation to the nuclear interaction was proposed by Skyrme [93] and it is widely used in the literature [10, 94, 95, 96, 97, 98, 99, 100, 101, 102, 103, 104, 105, 106, 107, 108, 109, 110, 111, 112, 113, 114, 115, 116, 117, 118, 119, 120, 121, 122, 123, 124, 125, 126, 127, 128, 129, 130, 131, 132, 133, 134, 135, 136, 137, 138, 139, 140, 141, 142]. Hundreds of interactions have been proposed but stringent experimental quantities are also available which should, in principle, reduce this huge explosion of the number of interactions. The knowledge of the kinetic and potential energies of nucleons leads to the Nuclear Equation of State (NEOS). In heavy-ion collisions, highly excited systems may be formed and, under some conditions, a temperature and a density

may be recovered from experimental observations or models. In this way it is possible to investigate the NEOS at finite temperature. First we will discuss the NEOS at zero temperature and we will assume that the interaction among nucleons is local.

A popular approach is to postulate an equation of state which satisfies known properties of nuclei. We can introduce the density dependence or the momentum dependence of the interactions among nucleons and we need to distinguish between protons and neutrons. It is possible to write the energy per nucleon as:

$$\frac{E}{A}(\rho, m_\chi) = (1 + \frac{5}{9}m_\chi^2)\bar{\varepsilon}_{f0}\tilde{\rho}^{2/3} + (1 + c_1 m_\chi^2)\frac{A_1}{2}\tilde{\rho} + (1 + c_2 m_\chi^2)\frac{B_1}{1+\sigma}\tilde{\rho}^{\sigma}, \qquad (1.28)$$

where $\tilde{\rho} = \frac{\rho}{\rho_0}$, $\bar{\varepsilon}_{f0}$ is the average Fermi energy at ρ_0, A_1, B_1, σ, c_1 and c_2 are the parameters to be determined in order to reproduce some properties of infinite nuclear matter (INM). This NEOS is dubbed modified CK225. The assumed form for the energy per nucleon in Eq. (1.28) is for guidance only and many different forms can be found in the literature [10, 58, 76, 92, 94, 95, 96, 97, 143, 144]. It is a simple expansion to second order in $m_\chi = \frac{N-Z}{A}$, and higher order terms might be added once more constraints to the NEOS are determined.

This equation refers to an hypothetical infinite nuclear system with N neutrons and Z protons without Coulomb interaction. In order to fix the parameters entering Eq. (1.28), we impose some constraints coming from observations. In particular for symmetric nuclear matter we require that:

$$\begin{cases} \frac{E}{A}(\rho, m_\chi = 0)\Big|_{\rho=\rho_0} = -15 \text{ MeV}, \\ P|_{\rho=\rho_0} = \rho^2 \frac{\partial[\frac{E}{A}(\rho, m_\chi=0)]}{\partial\rho}\Big|_{\rho=\rho_0} = 0, \\ K = 9\frac{\partial P}{\partial\rho}\Big|_{\rho=\rho_0} = 225 \text{ MeV}. \end{cases} \qquad (1.29)$$

Where the pressure must be zero for a system in the ground state and the incom-

pressibility is fixed by the ISGMR [10, 11, 12, 13, 14, 15, 16, 17, 18, 19, 20, 21]. There is a general consensus that $K = 250 \pm 25$ MeV, here we assume $K = 225$ MeV which is the same value obtained in a simple Fermi gas [145]. The latter condition implies that interactions give no contribution to the incompressibility at ground state density. Solving equations (1.29) gives: $A_1 = -210$ MeV, $B_1 = 157.5$ MeV and $\sigma = \frac{4}{3}$. We recall that the repulsive higher order density dependence is needed in order to get nuclear saturation. Once the interaction is known, it is easy to calculate the forces acting on a particle from the gradient of the mean field with respect to $\mathbf{r}$ [8, 76, 78, 80, 81].

The value of the ground state energy is obtained from the mass formula and precisely from the volume term [3, 4, 5, 6, 146]. In order to fix the parameters for the asymmetric NEOS we need to know the value of the symmetry energy that, as we have discussed in [147], is somehow constrained between 20 MeV and 40 MeV. The definition of symmetry energy $S(\rho)$ to order m_χ^2 is

$$\begin{aligned} \frac{E}{A}(\rho, m_\chi) - \frac{E}{A}(\rho, 0) &= (\frac{5}{9}\bar{\varepsilon}_{f0}\tilde{\rho}^{2/3} + c_1\frac{A_1}{2}\tilde{\rho} + c_2\frac{B_1}{1+\sigma}\tilde{\rho}^\sigma)m_\chi^2 \\ &= S(\rho)m_\chi^2. \end{aligned} \tag{1.30}$$

Therefore

$$S(\rho) = \frac{5}{9}\bar{\varepsilon}_{f0}\tilde{\rho}^{2/3} + c_1\frac{A_1}{2}\tilde{\rho} + c_2\frac{B_1}{1+\sigma}\tilde{\rho}^\sigma. \tag{1.31}$$

Similar to the pressure and incompressibility defined in section 1.1, we can define the following quantities:

$$\begin{aligned} L(\rho) &= 3\rho_0\frac{\partial S(\rho)}{\partial \rho} \\ &= 3[\frac{10}{27}\bar{\varepsilon}_{f0}\tilde{\rho}^{-1/3} + c_1\frac{A_1}{2} + c_2\frac{B_1\sigma}{1+\sigma}\tilde{\rho}^{\sigma-1}], \end{aligned} \tag{1.32}$$

$$
\begin{aligned}
K_{sym}(\rho) &= 9\rho_0^2 \frac{\partial^2 S(\rho)}{\partial \rho^2} \\
&= 9[-\frac{10}{81}\bar{\varepsilon}_{f0}\tilde{\rho}^{-4/3} + c_2 \frac{B_1\sigma(\sigma-1)}{1+\sigma}\tilde{\rho}^{\sigma-2}]. \qquad (1.33)
\end{aligned}
$$

The definitions above help in understanding the sensitivity of different observables to each of them. For instance, we have seen that the ISGMR is sensitive to the incompressibility, on similar grounds we might expect that the IVGDR is sensitive to $K_{sym} = K_{sym}(\rho_0)$. Furthermore, they might be useful when comparing different forms of proposed nuclear interactions. However, we can only constrain Eq. (1.31) from properties of finite nuclei. To have a better grasp of the symmetry energy we need more constraints to fix the values of c_1, c_2.

It is instructive to calculate the values of $L = L(\rho_0)$ and K_{sym}. Simple calculations give:

$$L = L(\rho_0) = 3[\frac{10}{27}\bar{\varepsilon}_{f0} + c_1\frac{A_1}{2} + c_2\frac{B_1\sigma}{1+\sigma}], \qquad (1.34)$$

$$K_{sym} = K_{sym}(\rho_0) = 9[-\frac{10}{81}\bar{\varepsilon}_{f0} + c_2\frac{B_1\sigma(\sigma-1)}{1+\sigma}]. \qquad (1.35)$$

Substituting Eqs. (1.34, 1.35) into the symmetry energy Eq. (1.31):

$$E_{sym} = S(\rho_0) = \frac{5}{27}\bar{\varepsilon}_{f0} - \frac{10}{81}\frac{\bar{\varepsilon}_{f0}}{\sigma} + \frac{L}{3} - \frac{K_{sym}}{9\sigma}. \qquad (1.36)$$

The latter equation links the values of L and K_{sym} to the symmetry energy value and to σ. Recall that the value of σ is connected to the nuclear incompressibility K and it is greater than 1 in order to get nuclear saturation. For $\sigma = 2$ we have $K = 380$ MeV. From Eq. (1.36) we can estimate $K_{sym} = -159$ MeV, for $S(\rho_0) = 32$ MeV, $L = 50$ MeV, $\sigma = \frac{4}{3}$; and $K_{sym} = -226$ MeV if $\sigma = 2$, which shows the sensitivity of K_{sym} to the incompressibility. Thus it is difficult to find physical quantities which depend on one ingredient rather than another one. Of course Eqs. (1.34, 1.35, 1.36)

refer to the particular NEOS we are using and these relations will change for different choices such as including momentum dependent forces. In the latter case we will still obtain similar relations with the addition of a new ingredient, the effective mass, which we will define in the following section 1.3.2.

Table 1.1: Values of the parameters assuming a second order phase transition. Cases (8) and (9) refer respectively, to Eq. (1.28) and a free Fermi gas approximation. For cases (5) (QLG) and (6) (QGP), two different critical densities are obtained for the same concentration and symmetry energy. The incompressibility is $K = 225$ MeV for all cases.

	$S(\rho_0)$ (MeV)	$\tilde{\rho}_c$	m_c	c_1	c_2	L (MeV)	K_{sym} (MeV)
1	23.2	0.216256	0.92	-0.492449	-0.607513	16.0929	-189.028
2	23.2	0.331363	0.92	-0.583811	-0.749632	6.49982	-227.401
3	32	0.188629	0.78	-0.730633	-0.847651	26.2835	-253.866
4	32	0.0715581	0.94	-0.164079	0.0336557	85.7718	-15.913
5	32	0.0638193	0.98	-0.0898674	0.149095	93.5639	15.2557
6	32	4.43276	0.98	-0.809792	-0.970788	17.9718	-287.113
7	32	18.4109	1.1	-0.701832	-0.80285	29.3076	-241.769
8	12.5	-	-	0.0	0.0	25	-25
9	12.5	-	-	$(A_1 = B_1 = 0)$ 0.0	0.0	25	-25

In order to illustrate the importance of the symmetry energy and its relevance,

for instance to understand neutron stars, we will assume that asymmetric nuclear matter undergoes a second order phase transition already at zero temperature. This is fulfilled by solving the equations:

$$\begin{cases} S(\rho_0) = E_{sym}, \\ \frac{\partial P}{\partial \rho}\Big|_{\rho=\rho_c} = 0, \\ \frac{\partial^2 P}{\partial \rho^2}\Big|_{\rho=\rho_c} = 0. \end{cases} \tag{1.37}$$

We fix $m_\chi = m_c$ (for a second order phase transition) close to 1, then we solve for c_1, c_2 and ρ_c. Typical results are included in table 1.1.

Let us start from the easiest cases (8) and (9) in table 1.1. Case (9) refers to a pure Fermi gas, while case (8) refers to Eq. (1.28) when $c_1 = c_2 = 0$. Those two cases have exactly the same values of the physical quantities defined in Eqs. (1.31, 1.32, 1.33), but differ for the ground state binding energy and pressure. All the other cases display a second order phase transition at low densities for $S(\rho_0) = 23.2$ MeV and at very high densities for $S(\rho_0) = 32$ MeV. It is very surprising such a sensitivity of the NEOS by just changing the value of the symmetry energy obtained from the mass formula. This gives two completely different scenarios for our equation of state. For the lower symmetry energy value, we can think of a quantum liquid-gas (QLG) phase transition (see next section) occurring already at zero temperature but for almost pure neutron matter. On the other hand, the values obtained for the larger symmetry energy could be associated to a phase transition at high densities, from neutron matter to the quark-gluon plasma (QGP). Case (7) gives a second order phase transition for $m_c = 1.1$ which is unphysical and we used to mimic a cross-over to the QGP at high densities. At present there is no universal consensus on the values of L and K_{sym}, if we use a 'popular' value for $L = 50 \pm 40$ MeV, we see that

most values reported in the table could be accepted. The value for K_{sym} is even less determined.

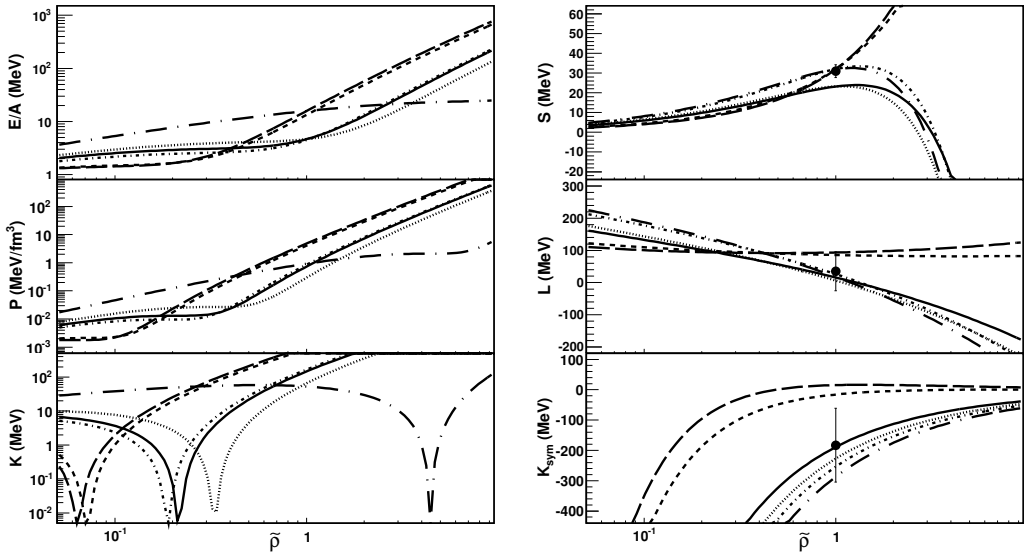

Figure 1.1: The E/A, P, K, S, L and K_{sym}, for cases (1-6) in table 1.1. The solid line refers to case (1), dotted line refers to case (2), the dash-dotted line refers to case (3), the dashed line refers to case (4), the long dashed line refers to case (5) and the long dash-dotted line refers to case (6).

In Fig. 1.1 we plot the different physical quantities described above versus densities for cases (1-6) from table 1.1. The critical densities are easily recognized and on the right panels we have indicated some 'current' estimates of S, L and K_{sym}. We stress that the speed of sound is always less than c the speed of light for the cases reported in the figure, in particular it is zero at the phase transition densities, which is especially relevant for those NEOS exhibiting a second order phase transition at high densities. From these simple estimates we hope we have further highlighted the

importance of determining the symmetry energy.

1.3.2 Momentum Dependent NEOS

An important ingredient of the NEOS is its momentum dependence. Most experimental data require a non local potential due to the fact that nucleons are not elementary particles [148, 149, 150, 151, 152, 153]. A large variety of momentum dependent interactions have been proposed, especially to reproduce low excitation energy phenomena such as giant resonances. Most of those interactions are valid for relative momenta of the order of the Fermi momenta. The phenomenology of high energy heavy-ion collisions requires that the momentum dependence should not diverge for relative momenta higher than the Fermi one. Several momentum dependent NEOS (MNEOS) have been proposed [8, 76, 78, 80, 87, 154, 155, 156, 157, 158, 159]. For instance, following [8, 154], the potential energy density is

$$V(\rho) = \frac{a\rho^2}{2\rho_0} + \frac{b\rho^{\sigma+1}}{(\sigma+1)\rho_0^{\sigma}} + c\frac{\rho}{\rho_0}\int \frac{f(\mathbf{r},\mathbf{p})}{1+(\frac{\mathbf{p}-\langle\mathbf{p}\rangle}{\Lambda})^2}d^3p, \tag{1.38}$$

where Λ is a constant, $\langle\mathbf{p}\rangle$ is the average momentum at position $\mathbf{r}$. $f(\mathbf{r},\mathbf{p})$ is the nucleon density in the phase space. When $T = 0$,

$$f(\mathbf{r},\mathbf{p}) = \frac{g}{h^3}\Theta(p_f - p)\Theta(R - r), \tag{1.39}$$

where Θ is the step function. According to the definition of $f(\mathbf{r},\mathbf{p})$,

$$\int d^3x d^3p f(\mathbf{r},\mathbf{p}) = A, \tag{1.40}$$

then we have

$$\frac{g}{h^3} = \frac{3}{4\pi}\frac{\rho}{p_f^3}, \quad p_f = (\frac{3}{4\pi}\frac{h^3}{g})^{1/3}\rho^{1/3} = d\rho^{1/3}, \tag{1.41}$$

where $\rho = \frac{A}{V}$, $d = (\frac{3}{4\pi}\frac{h^3}{g})^{1/3}$. Therefore

$$\begin{aligned} f(\mathbf{r},\mathbf{p}) &= \frac{g}{h^3}\Theta(p_f - p)\Theta(R - r) \\ &= \frac{3}{4\pi}\frac{\rho}{p_f^3}\Theta(p_f - p) \\ &= \rho\frac{3}{4\pi p_f^3}\Theta(p_f - p) \\ &= \rho f(\mathbf{p}), \end{aligned} \tag{1.42}$$

where $f(\mathbf{p}) = \frac{3}{4\pi p_f^3}\Theta(p_f - p)$ and $\rho = \int d^3p f(\mathbf{r},\mathbf{p})$.

The corresponding one body potential $U(\rho,\mathbf{p}) = \partial V(\rho)/\partial\rho_p$, which will be used to calculate the effective mass, is

$$\begin{aligned} U(\rho,\mathbf{p}) &= \frac{\delta V(\rho)}{\delta\rho_p} \\ &= \frac{\frac{\delta V(\rho)}{\delta f(\mathbf{r},\mathbf{p})}}{\frac{\delta\rho}{\delta f(\mathbf{r},\mathbf{p})}} \\ &= a\frac{\rho}{\rho_0} + b(\frac{\rho}{\rho_0})^\sigma + c\frac{1}{\rho_0}\int\frac{f(\mathbf{r},\mathbf{p})d^3p}{1+(\frac{\mathbf{p}-<\mathbf{p}>}{\Lambda})^2} + \frac{c\rho}{\rho_0}\frac{1}{1+(\frac{\mathbf{p}-<\mathbf{p}>}{\Lambda})^2} \\ &= a\frac{\rho}{\rho_0} + b(\frac{\rho}{\rho_0})^\sigma + c\frac{\rho}{\rho_0}\langle\frac{1}{1+(\frac{\mathbf{p}-<\mathbf{p}>}{\Lambda})^2}\rangle + \frac{c\rho}{\rho_0}\frac{1}{1+(\frac{\mathbf{p}-<\mathbf{p}>}{\Lambda})^2}, \end{aligned} \tag{1.43}$$

where $\langle\frac{1}{1+(\frac{\mathbf{p}-<\mathbf{p}>}{\Lambda})^2}\rangle = \int\frac{f(\mathbf{p})d^3p}{1+(\frac{\mathbf{p}-<\mathbf{p}>}{\Lambda})^2}$. We have used the functional variation

$$\frac{\delta f(x)}{\delta f(x')} = \delta(x - x'). \tag{1.44}$$

For static nuclear matter, $\langle\mathbf{p}\rangle = 0$. Therefore

$$\begin{aligned} \langle\frac{1}{1+(\frac{p-\langle\mathbf{p}\rangle}{\Lambda})^2}\rangle &= \int\frac{f(\mathbf{p})}{1+(\frac{\mathbf{p}-\langle\mathbf{p}\rangle}{\Lambda})^2}d^3p \\ &= \frac{3}{4\pi p_f^3}\int_0^{p_f}\frac{4\pi p^2}{1+(\frac{p}{\Lambda})^2}dp \end{aligned}$$

$$= 3(\frac{\Lambda}{p_f})^3[\frac{p_f}{\Lambda} - \tan^{-1}(\frac{p_f}{\Lambda})]. \quad (1.45)$$

The energy per nucleon is:

$$\begin{aligned}
\frac{E}{A} &= \frac{3}{5}\frac{p_f^2}{2m} + \frac{V(\rho)}{\rho} \\
&= \frac{3}{5}\frac{p_f^2}{2m} + \frac{a}{2}\frac{\rho}{\rho_0} + \frac{b}{\sigma+1}(\frac{\rho}{\rho_0})^\sigma + c\frac{\rho}{\rho_0}\langle\frac{1}{1+(\frac{p-\langle\mathbf{p}\rangle}{\Lambda})^2}\rangle \\
&= \frac{3}{5}\frac{p_f^2}{2m} + \frac{a}{2}\frac{\rho}{\rho_0} + \frac{b}{\sigma+1}(\frac{\rho}{\rho_0})^\sigma + c\frac{\rho}{\rho_0}3(\frac{\Lambda}{p_f})^3[\frac{p_f}{\Lambda} - \tan^{-1}(\frac{p_f}{\Lambda})]. \quad (1.46)
\end{aligned}$$

Thus the pressure is given by:

$$\begin{aligned}
P &= \rho^2\frac{\partial(\frac{E}{A})}{\partial\rho} \\
&= \frac{2}{5}\frac{d^2}{2m}\rho^{5/3} + \frac{a}{2}\frac{\rho^2}{\rho_0} + \frac{b\sigma}{1+\sigma}\frac{\rho^{\sigma+1}}{\rho_0^\sigma} + c\frac{\rho^2}{\rho_0}\frac{1}{1+(\frac{p_F}{\Lambda})^2} \\
&= \frac{2}{5}\frac{p_F^2}{2m}\rho + \frac{a}{2}\frac{\rho^2}{\rho_0} + \frac{b\sigma}{1+\sigma}\frac{\rho^{\sigma+1}}{\rho_0^\sigma} + c\frac{\rho^2}{\rho_0}\frac{1}{1+(\frac{p_f}{\Lambda})^2}, \quad (1.47)
\end{aligned}$$

and the incompressibility:

$$\begin{aligned}
K &= 9\frac{\partial P}{\partial\rho}\Big|_{\rho=\rho_0} \\
&= 9[\frac{2}{3}\frac{d^2}{2m}\rho^{2/3} + a\frac{\rho}{\rho_0} + b\sigma\frac{\rho^\sigma}{\rho_0^\sigma} + 2c\frac{\rho}{\rho_0}\frac{1}{1+(\frac{p_f}{\Lambda})^2} - c\frac{\rho^2}{\rho_0}(\frac{1}{1+(\frac{p_f}{\Lambda})^2})^2(2\frac{p_f}{\Lambda^2})(\frac{1}{3}\frac{p_f}{\rho})] \\
&= 9[\frac{2}{3}\frac{p_f^2}{2m} + a\frac{\rho}{\rho_0} + b\sigma\frac{\rho^\sigma}{\rho_0^\sigma} + 2c\frac{\rho}{\rho_0}\frac{1}{1+(\frac{p_f}{\Lambda})^2} - \frac{2}{3}c(\frac{p_f}{\Lambda})^2\frac{\rho}{\rho_0}(\frac{1}{1+(\frac{p_f}{\Lambda})^2})^2]\Big|_{\rho=\rho_0, p_f=p_{f0}} \quad (1.48)
\end{aligned}$$

Using the same conditions, Eq. (1.29), we can fix the parameters entering the MNEOS. However, the number of constraints is not enough, thus Λ is a free parameter. It determines how fast the momentum dependent part becomes negligible, and should be larger than the Fermi momentum. In refs. [8, 154], $a = -144.9$

MeV, $b = 203.3$ MeV, $c = -75$ MeV, $\sigma = \frac{7}{6}$ and $\Lambda = 1.5 p_{f0} = 1.5 d \rho_0^{1/3}$ giving an incompressibility $K = 215$ MeV. Using this MNEOS, the collective flow observed in heavy-ion collisions is well reproduced, in particular a higher flow is observed as compared to a local NEOS. In order to reproduce a similar flow, local NEOS must have a much larger incompressibility $K = 380$ MeV [8, 80]. Notice that the force acting on a particle now contains a term which is the gradient of the mean field with respect to $\mathbf{p}$ [8, 76, 78, 80, 81].

The definition of the effective mass is:

$$\frac{m^*}{m} = [1 + \frac{m}{p}\frac{dU}{dp}]^{-1}_{p=p_{f0}}. \tag{1.49}$$

Using Eq. (1.43) gives:

$$\frac{dU}{dp} = -c\frac{\rho}{\rho_0}\frac{2\frac{p}{\Lambda^2}}{[1+(\frac{p}{\Lambda})^2]^2}, \tag{1.50}$$

this gives an effective mass at ground state density:

$$\begin{aligned} \frac{m^*}{m} &= [1 + \frac{m}{p}\frac{dU}{dp}]^{-1}_{p=p_{f0}} \\ &= \Big\{1 - \frac{m}{p_{f0}} c \frac{2\frac{p_{f0}}{\Lambda^2}}{[1+(\frac{p_{f0}}{\Lambda})^2]^2}\Big\}^{-1} \\ &= 0.7, \end{aligned} \tag{1.51}$$

using the values of Λ and c reported above.

1.3.3 Asymmetric Nuclear Matter EOS with Momentum Dependence

Using Eq. (1.46) we can define the MNEOS for asymmetric nuclear matter as:

$$\begin{aligned} \frac{E}{A} &= \frac{E}{A}\Big|_p \times \frac{Z}{A} + \frac{E}{A}\Big|_n \times \frac{N}{A} \\ &= \frac{3}{5}\frac{p_{fp}^2}{2m} \times \frac{Z}{A} + \frac{3}{5}\frac{p_{fn}^2}{2m} \times \frac{N}{A} \end{aligned}$$

$$+\frac{a}{2}(1+c_1 m_\chi^2)\frac{\rho}{\rho_0}+\frac{b}{\sigma+1}(1+c_2 m_\chi^2)(\frac{\rho}{\rho_0})^\sigma$$
$$+c\frac{\rho}{\rho_0}3(\frac{\Lambda}{p_{fp}})^3[\frac{p_{fp}}{\Lambda}-\tan^{-1}(\frac{p_{fp}}{\Lambda})]\times\frac{Z}{A}+c\frac{\rho}{\rho_0}3(\frac{\Lambda}{p_{fn}})^3[\frac{p_{fn}}{\Lambda}-\tan^{-1}(\frac{p_{fn}}{\Lambda})]\times\frac{N}{A}. \tag{1.52}$$

Since

$$p_{fp}=d_p\rho_p^{1/3},\quad p_{fn}=d_n\rho_n^{1/3},\quad p_f=d\rho^{1/3}, \tag{1.53}$$

and

$$d_p=d_n=2^{1/3}d, \tag{1.54}$$

$$\rho_p=\frac{1-m_\chi}{2}\rho,\quad \rho_n=\frac{1+m_\chi}{2}\rho, \tag{1.55}$$

$$p_{fp}=p_f(1-m_\chi)^{1/3},\quad p_{fn}=p_f(1+m_\chi)^{1/3}, \tag{1.56}$$

thus

$$\begin{aligned}\frac{3}{5}\frac{p_{fp}^2}{2m}\times\frac{Z}{A}+\frac{3}{5}\frac{p_{fn}^2}{2m}\times\frac{N}{A} &= \frac{3}{5}\frac{p_f^2}{2m}[(1-m_\chi)^{2/3}\times\frac{1-m_\chi}{2}+(1+m_\chi)^{2/3}\times\frac{1+m_\chi}{2}]\\ &= \frac{3}{5}\frac{p_f^2}{2m}\frac{1}{2}[(1-m_\chi)^{5/3}+(1+m_\chi)^{5/3}]\\ &\approx \frac{3}{5}\frac{p_f^2}{2m}(1+\frac{5}{9}m_\chi^2),\end{aligned} \tag{1.57}$$

$$\begin{aligned}c\frac{\rho}{\rho_0}3(\frac{\Lambda}{p_{fp}})^3[\frac{p_{fp}}{\Lambda}-\tan^{-1}(\frac{p_{fp}}{\Lambda})]\times\frac{Z}{A} &= c\frac{\rho}{\rho_0}3(\frac{\Lambda}{p_f})^3\frac{1}{1-m_\chi}\\ &\quad\times[\frac{p_f}{\Lambda}(1-m_\chi)^{1/3}-\tan^{-1}(\frac{p_f}{\Lambda}(1-m_\chi)^{1/3})]\times\frac{1-m_\chi}{2}\\ &= \frac{1}{2}c\frac{\rho}{\rho_0}3(\frac{\Lambda}{p_f})^3[\frac{p_f}{\Lambda}(1-m_\chi)^{1/3}-\tan^{-1}(\frac{p_f}{\Lambda}(1-m_\chi)^{1/3})].\end{aligned} \tag{1.58}$$

Similarly, we can obtain

$$c\frac{\rho}{\rho_0}3(\frac{\Lambda}{p_{fn}})^3[\frac{p_{fn}}{\Lambda}-\tan^{-1}(\frac{p_{fn}}{\Lambda})]\times\frac{N}{A}=\frac{1}{2}c\frac{\rho}{\rho_0}3(\frac{\Lambda}{p_f})^3[\frac{p_f}{\Lambda}(1+m_\chi)^{1/3}-\tan^{-1}(\frac{p_f}{\Lambda}(1+m_\chi)^{1/3})]. \tag{1.59}$$

Substituting Eqs. (1.57, 1.58, 1.59) into Eq. (1.52), one can obtain the energy per nucleon

$$\begin{aligned}\frac{E}{A} &= \frac{3}{5}\frac{p_f^2}{2m}(1+\frac{5}{9}m_\chi^2)+\frac{a}{2}(1+c_1m_\chi^2)\frac{\rho}{\rho_0}+\frac{b}{\sigma+1}(1+c_2m_\chi^2)(\frac{\rho}{\rho_0})^\sigma \\ &+\frac{1}{2}c\frac{\rho}{\rho_0}3(\frac{\Lambda}{p_f})^3[\frac{p_f}{\Lambda}(1-m_\chi)^{1/3}-\tan^{-1}(\frac{p_f}{\Lambda}(1-m_\chi)^{1/3})] \\ &+\frac{1}{2}c\frac{\rho}{\rho_0}3(\frac{\Lambda}{p_f})^3[\frac{p_f}{\Lambda}(1+m_\chi)^{1/3}-\tan^{-1}(\frac{p_f}{\Lambda}(1+m_\chi)^{1/3})],\end{aligned} \tag{1.60}$$

where we have followed the same philosophy of the local NEOS. The important difference is due to the momentum dependent interaction which results in another contribution to the symmetry energy because of the difference of Fermi momenta of protons and neutrons when their densities are different.

Using Eq. (1.31) the symmetry energy is:

$$\begin{aligned}S(\rho) &= \frac{1}{3}\frac{p_f^2}{2m}+\frac{a}{2}c_1\frac{\rho}{\rho_0}+\frac{b}{1+\sigma}c_2(\frac{\rho}{\rho_0})^\sigma \\ &+\frac{3}{2}c\frac{\rho}{\rho_0}(\frac{\Lambda}{p_f})^3[2^{1/3}\frac{p_f}{\Lambda}-\tan^{-1}(2^{1/3}\frac{p_f}{\Lambda})]-3c\frac{\rho}{\rho_0}(\frac{\Lambda}{p_f})^3[\frac{p_f}{\Lambda}-\tan^{-1}(\frac{p_f}{\Lambda})].\end{aligned} \tag{1.61}$$

Thus

$$\begin{aligned}L(\rho) &= 3\Big\{\frac{2}{9}\frac{p_f^2}{2m}\frac{1}{\rho/\rho_0}+c_1\frac{a}{2}+c_2\frac{b\sigma}{1+\sigma}(\frac{\rho}{\rho_0})^{\sigma-1} \\ &+\frac{c}{2^{2/3}}(\frac{\Lambda}{p_f})^2[1-\frac{1}{1+2^{2/3}(\frac{p_f}{\Lambda})^2}]-c(\frac{\Lambda}{p_f})^2[1-\frac{1}{1+(\frac{p_f}{\Lambda})^2}]\Big\},\end{aligned} \tag{1.62}$$

$$
\begin{aligned}
K_{sym}(\rho) &= 9\Big\{ -\frac{2}{27}\frac{p_f^2}{2m}\frac{1}{(\rho/\rho_0)^2} + c_2\frac{b\sigma(\sigma-1)}{1+\sigma}(\frac{\rho}{\rho_0})^{\sigma-2} \\
&\quad +\frac{2^{1/3}c}{3}\frac{1}{\rho/\rho_0}[-(\frac{\Lambda}{p_f})^2(1-\frac{1}{1+2^{2/3}(\frac{p_f}{\Lambda})^2}) + \frac{2^{2/3}}{(1+2^{2/3}(\frac{p_f}{\Lambda})^2)^2}] \\
&\quad -\frac{2c}{3}\frac{1}{\rho/\rho_0}[-(\frac{\Lambda}{p_f})^2(1-\frac{1}{1+(\frac{p_f}{\Lambda})^2}) + \frac{1}{(1+(\frac{p_f}{\Lambda})^2)^2}]\Big\}. \qquad (1.63)
\end{aligned}
$$

Similar to Eq. (1.36), we obtain

$$
\begin{aligned}
S(\rho_0) &= \frac{1}{9}\frac{p_{f0}^2}{2m} - \frac{2}{27\sigma}\frac{p_{f0}^2}{2m} + \frac{L}{3} - \frac{K_{sym}}{9\sigma} \\
&\quad +\frac{3}{2}c(\frac{\Lambda}{p_{f0}})^3[2^{1/3}\frac{p_{f0}}{\Lambda} - \tan^{-1}(2^{1/3}\frac{p_{f0}}{\Lambda})] - 3c(\frac{\Lambda}{p_{f0}})^3[\frac{p_{f0}}{\Lambda} - \tan^{-1}(\frac{p_{f0}}{\Lambda})] \\
&\quad -\frac{c}{2^{2/3}}(\frac{\Lambda}{p_{f0}})^2[1-\frac{1}{1+2^{2/3}(\frac{p_{f0}}{\Lambda})^2}] - c(\frac{\Lambda}{p_{f0}})^2[1-\frac{1}{1+(\frac{p_{f0}}{\Lambda})^2}] \\
&\quad +\frac{1}{\sigma}\{\frac{2^{1/3}c}{3}[-(\frac{\Lambda}{p_{f0}})^2(1-\frac{1}{1+2^{2/3}(\frac{p_{f0}}{\Lambda})^2}) + \frac{2^{2/3}}{(1+2^{2/3}(\frac{p_{f0}}{\Lambda})^2)^2}] \\
&\quad -\frac{2c}{3}[-(\frac{\Lambda}{p_{f0}})^2(1-\frac{1}{1+(\frac{p_{f0}}{\Lambda})^2}) + \frac{1}{(1+(\frac{p_{f0}}{\Lambda})^2)^2}]\} \\
&= \frac{5}{27}\bar{\varepsilon}_{f0} - \frac{10}{81}\frac{\bar{\varepsilon}_{f0}}{\sigma} + \frac{L}{3} - \frac{K_{sym}}{9\sigma} \\
&\quad +\frac{3}{2}c(\frac{\Lambda}{p_{f0}})^3[2^{1/3}\frac{p_{F0}}{\Lambda} - \tan^{-1}(2^{1/3}\frac{p_{f0}}{\Lambda})] - 3c(\frac{\Lambda}{p_{f0}})^3[\frac{p_{f0}}{\Lambda} - \tan^{-1}(\frac{p_{f0}}{\Lambda})] \\
&\quad -\frac{c}{2^{2/3}}(\frac{\Lambda}{p_{f0}})^2[1-\frac{1}{1+2^{2/3}(\frac{p_{f0}}{\Lambda})^2}] - c(\frac{\Lambda}{p_{f0}})^2[1-\frac{1}{1+(\frac{p_{f0}}{\Lambda})^2}] \\
&\quad +\frac{1}{\sigma}\{\frac{2^{1/3}c}{3}[-(\frac{\Lambda}{p_{f0}})^2(1-\frac{1}{1+2^{2/3}(\frac{p_{f0}}{\Lambda})^2}) + \frac{2^{2/3}}{(1+2^{2/3}(\frac{p_{f0}}{\Lambda})^2)^2}] \\
&\quad -\frac{2c}{3}[-(\frac{\Lambda}{p_{f0}})^2(1-\frac{1}{1+(\frac{p_{f0}}{\Lambda})^2}) + \frac{1}{(1+(\frac{p_{f0}}{\Lambda})^2)^2}]\}, \qquad (1.64)
\end{aligned}
$$

where the relation $\bar{\varepsilon}_{f0} = \frac{3}{5}\frac{p_{f0}^2}{2m}$ has been used. The latter equation shows the connections among the various terms of the NEOS including the momentum dependent part through the parameter Λ. The previous result, Eq. (1.36), can be easily recovered by taking the limit $\Lambda \to 0$. A simple estimate gives $K_{sym} = -19.6$ MeV quite different from the estimate from Eq. (1.36). Changing the symmetry energy

of 1 MeV, changes the value of $K_{sym} = -30.1$ MeV, thus it is very sensitive to small changes.

Note that previously we have assumed that the same effective mass for both neutrons and protons. This might be not true and different options are discussed in the literature [76, 87, 155, 160, 161, 162, 163, 164, 165]. From the definition of effective mass, we can calculate it for the asymmetric part as well and we could have different values of the Λ parameters for n and p in the MNEOS discussed above. Detailed experimental data is needed to fix this point as well [166, 167].

1.4 The Nuclear Equation of State at Finite Temperatures

At finite temperatures the NEOS can be simply obtained by modifying the kinetic part in Eq. (1.28) for momentum independent interactions. The kinetic part can be obtained by solving the integral in Eq. (A.6) and using a finite temperature Fermi-Dirac distribution instead of a Θ-function. For momentum dependent interactions, the potential energy must be obtained by folding the relevant integrals with the finite temperature distributions. Various calculations can be found in the literature and we refer to those for details [76, 83, 92, 168].

It is instructive to derive the NEOS at finite temperatures in two limits. First let us assume that the ratio $\frac{T}{\varepsilon_f}$ is much smaller than one and use the low temperature Fermi approximation. The energy per nucleon for the modified CK225 NEOS can be written as:

$$\frac{E}{A} = (1+\frac{5}{9}m_\chi^2)\bar{\varepsilon}_{f0}\tilde{\rho}^{2/3} + (1+c_1 m_\chi^2)\frac{A_1}{2}\tilde{\rho} + (1+c_2 m_\chi^2)\frac{B_1}{1+\sigma}\tilde{\rho}^\sigma + \frac{1}{1+\frac{5}{9}m_\chi^2}a_0 T^2 \frac{1}{\tilde{\rho}^{2/3}}, \tag{1.65}$$

where $a_0 = 1/13.3$ MeV^{-1}.

For each value of m_χ the critical point can be calculated by finding the roots of the following equations, see also Eq. (1.37)

$$\begin{cases} \left.\frac{\partial P}{\partial \rho}\right|_{\rho=\rho_c} = 0, \\ \left.\frac{\partial^2 P}{\partial \rho^2}\right|_{\rho=\rho_c} = 0. \end{cases} \tag{1.66}$$

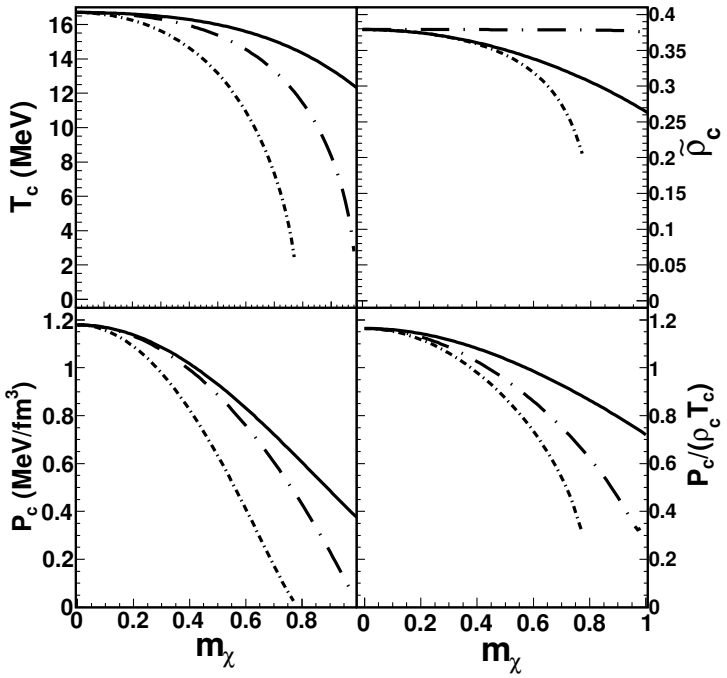

Figure 1.2: T_c, $\tilde{\rho}_c$, P_c and $\frac{P_c}{\rho_c T_c}$ versus m_χ for the modified CK225 NEOS using the low temperature Fermi gas approximation. Solid line for $(c_1 = 0, c_2 = 0)$ [case (8)], short dash-dotted line for $(c_1 = -0.730633, c_2 = 0.847651)$ [case (3)] and long dash-dotted line for $(c_1 = -0.501529, c_2 = -0.66137)$.

Those conditions, if fulfilled, give the critical temperature and the critical density,

for fixed m_χ, of the nuclear system and can be associated to a QLG phase transition. This is consistent with the description of the ground state of the nucleus as a quantum liquid drop, but we have to stress the fact that we have two liquid components: neutrons and protons. Using the low temperature approximation we get $T_c \approx 18$ MeV and $\rho_c \approx \frac{1}{3}\rho_0$ for symmetric nuclear matter. These values are consistent with those quoted in the literature which would suggest that our approximation is reasonable. However, when we look at the pressure and the ratio $\frac{P_c}{\rho_c T_c}$, we find surprising values as illustrated in Fig. 1.2. The value of the ratio for symmetric nuclear matter is larger than one and decreases for increasing asymmetries. Similar behavior for the other quantities are plotted in the figure. In particular the NEOS in table 1.1, case (3), gives a critical temperature equal to zero at $m_\chi = 0.78$. Experimental values of the critical ratio range somewhat around 0.28 for real gases [169] to 0.4 for the Van der Waals EOS [1, 7, 51]. This implies that our low temperature expansion is not yet convergent. If we include corrections to T^4 we obtain a shift to $T_c \approx 11$ MeV and values of the critical ratios less than one! This implies that the low temperature approximations converge very slowly, a feature which should be kept in mind when dealing with quantities near the critical point for a QLG phase transition.

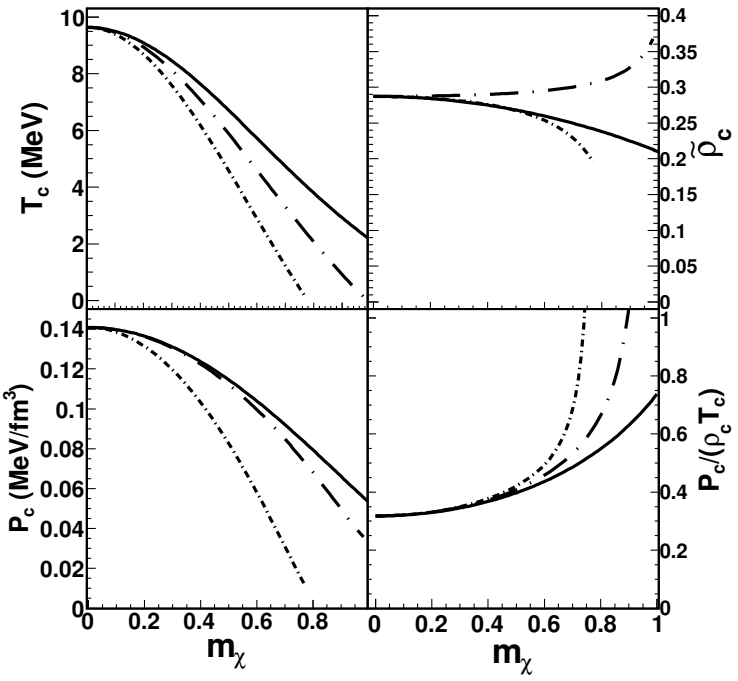

Figure 1.3: Similar to Fig. 1.2 but for the classical approximation.

We can investigate a second limit which is the classical one. Then the modified CK225 EOS becomes

$$P = \rho_0[(1+\frac{5}{9}m_\chi^2)\bar{\varepsilon}_{f0}\frac{2}{3}\tilde{\rho}^{5/3}+(1+c_1m_\chi^2)\frac{A_1}{2}\tilde{\rho}^2+(1+c_2m_\chi^2)\frac{B_1\sigma}{1+\sigma}\tilde{\rho}^{\sigma+1}+(1+\frac{5}{9}m_\chi^2)^{3/2}\tilde{\rho}T]. \tag{1.67}$$

In Eq. (1.67) we have used the relation $\tilde{\rho} \to \tilde{\rho}(1+\frac{5}{9}m_\chi^2)^{3/2}$ suggested from the Fermi gas. This is for the purpose of illustration in order to include a concentration dependence in the temperature part of the NEOS. The critical values obtained in this extreme limit are reported in Fig. 1.3, now the behavior as function of m_χ is in contrast with the low temperature approximation. The critical ratio is close to 0.3 but increases for neutron rich nuclear matter. The critical $T_c \approx 9$ MeV for symmetric

matter is about a factor of two below the previous estimate. The message is that in these ranges of temperatures and densities it is dangerous to use either purely classical or low $\frac{T}{\varepsilon_f}$ approximations: even though the behavior might seem reasonable in a given region, it is not so in another.

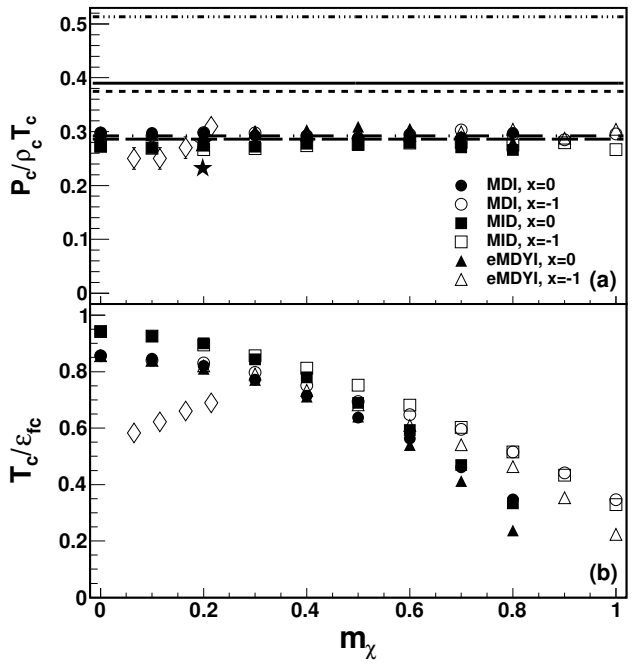

Figure 1.4: The $\frac{P_c}{\rho_c T_c}$ (top) and $\frac{T_c}{\varepsilon_{fc}}$ (bottom) versus m_χ. The results for MDI, MID and eMDYI interactions are obtained from [76, 170] which we refer for details. The dash-triple-dotted line is the result for an ideal Bose gas [1, 7, 51], the solid line is the result from the Fisher model [176], the dotted line is the result from a Van der Waals gas, the dash-dotted line is the result from Guggenheim [169], the dashed line is the result from the CMD model [175], the diamond from [171], the open star from [172, 173] and the solid star from [174]. The m_χ for [172, 173, 174] is estimated from ^{197}Au.

In Fig. 1.4 we display the results of exact calculations for different NEOS [76, 169, 170, 171, 172, 173, 174, 175, 176, 177]. Maybe not surprising, the critical ratio is constant as function of m_χ which suggests that the matter properties at the critical point are universal, i.e. independent of concentration. Furthermore, the calculated values are in agreement with real gases [169], and other values from the literature from heavy-ion collisions analysis that we will discuss later [171, 172, 173, 174]. Results from some theoretical models as well as the Van der Waals gas (which overestimates the ratio) are also displayed. The bottom part of the figure displays the behavior of $\frac{T_c}{\varepsilon_{fc}}$ as function of concentration. Such a ratio becomes very small for increasing concentrations, which explains why the low temperature approximation improves for large concentrations, see Fig. 1.2, while the opposite is true for the classical approximation reported in Fig. 1.3. The values of the critical temperature and density are consistent with those estimated in the low temperature limit and decrease for increasing concentration, similar to Fig. 1.2.

It is important to stress that the features discussed above are valid in the mean field approximation. Such an approximation is questionable in the instability region and near the critical point. The values of the critical exponents are not correct [1, 92], for instance if we expand the incompressibility $K(\rho, T)$ around the critical point:

$$\begin{aligned} K(\rho,T) &= K(\rho_c,T_c) \\ &\quad +K^{(1,0)}(\rho_c,T_c)(\rho-\rho_c)+\frac{1}{2}K^{(2,0)}(\rho-\rho_c)^2+\frac{1}{6}K^{(3,0)}(\rho-\rho_c)^3+\frac{1}{24}K^{(4,0)}(\rho-\rho_c)^4 \\ &\quad +[K^{(0,1)}+K^{(1,1)}(\rho_c,T_c)(\rho-\rho_c)+\frac{1}{2}K^{(2,1)}(\rho-\rho_c)^2+\frac{1}{6}K^{(3,1)}(\rho-\rho_c)^3 \\ &\quad +\frac{1}{24}K^{(4,1)}(\rho-\rho_c)^4]\times(T-T_c) \\ &= 0, \end{aligned} \tag{1.68}$$

where $K^{(i,j)}$ are the i, j derivatives respect to ρ and T. The terms $K^{(1,1)}(\rho_c, T_c)$, $K^{(2,1)}(\rho_c, T_c)$, $K^{(3,1)}(\rho_c, T_c)$, $K^{(4,1)}(\rho_c, T_c)$ can be neglected since they are of higher order in $(\rho - \rho_c) \times (T - T_c)$. Using Eq. (1.37) we also have:

$$K(\rho_c, T_c) = K^{(1,0)}(\rho_c, T_c) = 0. \tag{1.69}$$

Thus [92]:

$$\frac{1}{2}K^{(2,0)}(\rho - \rho_c)^2 + K^{(0,1)}(T - T_c) = 0, \tag{1.70}$$

from which we recover $\beta = 1/2$, i.e. one of the "classical" or mean field value for the critical exponents [1, 7, 51, 178]. As discussed by K. Huang [7], "when you do not know what to do, try the mean field approximation first". We learn many lessons from the mean field, but we cannot stop there, and we should try to push forward. One possible path is the use of molecular dynamics models which take into account quantum features such as the Pauli principle. It is clear that all of these are approximations and should be taken "cum grano salis".

1.4.1 Finite Sizes

We can study the properties of the NEOS at finite temperature by using heavy-ion collisions at beam energies around the Fermi energy. Two major problems arise when doing that: 1) nuclei are finite; 2) Coulomb forces must be included and those are long range forces. Furthermore, it is meaningless to speak about an NEOS in presence of a long range force. However, in some approximations and some physical conditions (low densities, high temperatures), we can correct for Coulomb effects and constrain the NEOS. Critical behavior has been observed in finite size systems, for instance in percolation models which we will use as reference, as well as in experimental data such as [179, 180]. There have been many attempts to correct for finite sizes

[172, 173, 175, 181, 182] and we will discuss here the mean field approximation of ref. [183]. The model is essentially based on the Hill-Wheeler approximation [184] modified to take into account the effect of finite temperatures.

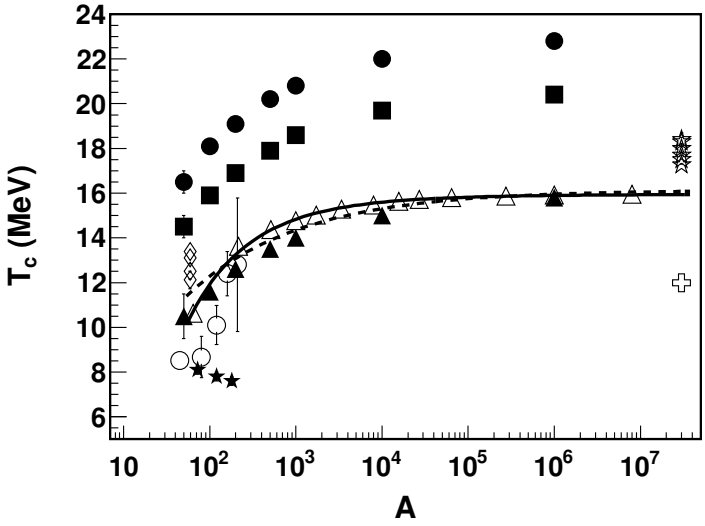

Figure 1.5: The critical temperature T_c versus the mass number A. Solid circles refer to ZR1, solid squares refer to ZR2, solid triangles refer to ZR3-NEOS [183]; open triangles refer to the percolation data [185]; open stars refer to the experimental results from Elliott [172, 173], solid stars refer to the experimental results from Elliott [174]; open diamonds refer to Mabiala's experimental results [171]; open circles refer to Natowitz's results [181, 182]; open cross refers to Ono's AMD calculations [189]. The percolation results are fitted with $T_c(A) = 15.949 - \frac{4.6149}{A^{1/3}} - \frac{65.305}{A^{2/3}}$ (solid line) and with $T_c(A) = 16.1346 - \frac{17.8664}{A^{1/3}}$ (dashed line).

For finite temperatures, the starting point is the partition function

$$Q(\beta) = \frac{V e^{-\beta\varepsilon_0}}{\lambda_T^3}(1 - \frac{\lambda_T}{4}\frac{S_{sphere}}{V} + \frac{\lambda_T^2}{8}\frac{L_{sphere}}{V}), \tag{1.71}$$

where $\lambda_T = (\frac{2\pi\hbar^2}{mkT})^{1/2}$ is the thermal wavelength of a nucleon [183], and the finite size corrections are given by terms S_{sphere} and L_{sphere} which are the surface area and circumference of the sphere respectively assuming the system is a sphere. Standard thermodynamics techniques are used to calculate the NEOS for finite nuclei in ref. [183] and the results for three different forms of the NEOS are reported in Fig. 1.5 where T_c is plotted as function of the system size A. The three different NEOS give critical temperatures ranging from 14 MeV to 22 MeV for infinite systems. For systems of mass $A = 50$ the critical temperature decreases as low as 10 MeV.

We can estimate the behavior of the critical point as function of mass in a simple bond percolation model [79, 185, 186, 187, 188]. If we assume that the critical temperature is proportional to the critical percolation bond probability [188]:

$$T_{perc} \propto \frac{1}{p_c}. \tag{1.72}$$

We can normalize Eq. (1.72) to any of the NEOS reported in Fig. 1.5. We can see that the behavior of the NEOS and the percolation model is surprisingly similar, giving a quick method to estimate the result of an infinite system, once the critical temperature for some masses are known. In the figure are also reported some experimental results obtained from heavy-ion collisions and different system sizes [171, 172, 173, 174, 181, 182]. The parametrization for the percolation model given in Fig. 1.5, inspired from the finite size Fermi gas results, could be used to derive $T_c(\infty)$. Of course, this discussion is for illustration only, since the critical temper-

ature should depend on the m_χ of the emitting source as predicted by mean-field calculations, see figures (1.2, 1.3, 1.4), and experimental results [171]. Notice, however, that the results of ref. [171] are obtained for fixed mass, with various neutron concentrations and including the Coulomb effects. Refs. [181, 182] results are obtained by changing the mass size but no information is given on the values of m_χ. Similarly for ref. [174] results, shown by solid stars, these authors have further devised a method to correct for finite sizes [172, 173]. We will discuss the different methods more in detail in chapter 3. Theoretical calculations have been performed in ref. [189] using the Antisymmetrized Molecular Dynamics model (AMD) with periodic boundary conditions. The estimated critical temperature is about 12 MeV. We stress that using a similar NEOS but in a mean field approximation gives a critical temperature of about 18 MeV as discussed in the previous section. A similar decrease in temperature has been observed in Classical Molecular Dynamics (CMD) calculations which were compared to the mean field approximation for the same interactions [175, 190, 191]. In the interesting work of ref. [183] corrections due to the Coulomb interaction and different concentrations are discussed as well. With these progresses and excellent experimental devices we should be able to pin down the NEOS at finite temperatures.

1.5 Neutron Stars

The knowledge of the NEOS is necessary to explain observed celestial objects and events. We will discuss the relevance of the NEOS in the case of neutron stars (NS). Those objects have been found so far with masses ranging from 1.4 to about 2 solar masses and a radius of the order of 10 km [33, 34, 35, 36, 37, 38, 39, 40, 41, 42, 43, 44]. These observations reveal that the density of the neutron star is larger than the ground state density of a nucleus, and of course it decreases to zero at the surface.

Thus a neutron star is a big nucleus made mostly of neutrons. Common understanding is that at the end of the evolution of a massive star, all the nuclear fuel, which are under the gravitational compression, is used up and only heavy nuclei, around iron, remain. At this stage, the gravitational force continues to compress the matter, leading to further collapse. For some conditions, which depend on the NEOS of the system, it becomes energetically more favorable to transform protons into neutrons by capturing electrons and keep the system electrically neutral. Now the NEOS, which is strongly repulsive, as we have discussed when $m_\chi \to 1$, balances the gravitational attraction. However, depending on the initial mass, dynamical equilibrium might be not reached such as in the observed Supernovae explosions [28, 29, 30, 31]. Explaining the observed masses and radii of neutron stars gives some constraints to the NEOS. We will describe briefly in this section some of these constraints and refer to more in depth review for more considerations and observations [28, 31, 44, 76, 95, 115].

Taking into account corrections due to general relativity, the structure equations, which properly describe a neutron star, are given by the Tolman-Oppenheimer-Volkoff (TOV) equations [192, 193]:

$$\frac{dm(r)}{dr} = \frac{4\pi r^2 \epsilon(r)}{c^2}, \tag{1.73}$$

$$\frac{dp(r)}{dr} = -\frac{G\epsilon(r)m(r)}{c^2 r^2}[1 + \frac{p(r)}{\epsilon(r)}][1 + \frac{4\pi r^3 p(r)}{m(r)c^2}][1 - \frac{2Gm(r)}{c^2 r}]^{-1}, \tag{1.74}$$

where G is the gravitational constant and c is the speed of light, $m(r)$ is the mass inside the sphere of radius r, $p(r)$ and $\epsilon(r)$ are the pressure and energy density of the star at radius r respectively. If the last term in Eq. (1.74) becomes zero, the pressure diverges. This defines the Schwarzschild radius and the condition for the occurrence of a black hole [28]. The NEOS enters throughout the pressure $p(r)$ and the energy

density $\epsilon(r)$. The TOV equations are easily solved numerically [194, 195, 196, 197].

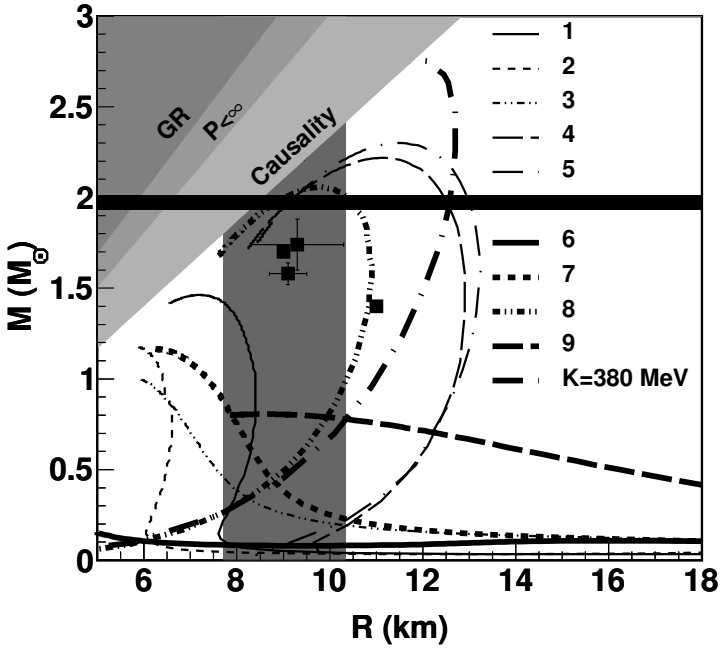

Figure 1.6: Neutron star mass-radius relations. The data points are from [38, 40, 41]. The radius band is from [43]. Different NEOS from table 1.1 are used to solve the TOV equations and are indicated in the figure.

Two particular simple but very instructive cases can be discussed first. If we assume that the neutron is replaced by massless quarks, the NEOS is that of an ideal massless Fermi gas with $\frac{p(r)}{\epsilon(r)} = \frac{1}{3}$, and $p \propto \rho^{4/3}$. This case gives an unphysical solution of the TOV equations, thus a simple non-interacting, massless QGP can be excluded. On the other hand, assuming a non-interacting nucleon gas gives $\frac{p(r)}{\epsilon(r)} = \frac{2}{3}$ in the non-relativistic case, and $p \propto \rho^{5/3}$. In the latter case the pressure increases faster with density and a solution to the TOV equations can be found. This solution is

displayed in Fig. 1.6 as a thick-dashed line and corresponds to case (9) in table 1.1. In the figure the relation between the mass (in units of solar masses) versus its radius is given. The region in the top left corner is forbidden either by causality or constraints from the TOV equations as discussed above [192, 193]. The thick horizontal line gives the maximum neutron star mass observed and, the shaded vertical region refers to the radii observed so far. The simple Fermi gas NEOS is well below the observed values and can be safely excluded. Adding the interaction but without changing the incompressibility ($c_1 = c_2 = 0$, Eq. (1.28)), gives the dash-dotted line reported in the figure and corresponds to case (8) in table 1.1. From the last two cases we understand that the actual value of the incompressibility is not the only important ingredient but the density dependence of the pressure is. For $K = 225$ MeV, $p \propto \rho^{7/3}$, clearly if we increase the density dependence of the pressure even further, we can obtain larger values of the neutron star mass. This is reported in the Fig. 1.6 for $K = 380$ MeV, and given by the long dash-dotted line, in this case $p \propto \rho^3$ at high densities. Now we could have NS of the order of 2.5 solar masses, but notice that this particular NEOS becomes acausal for radii below 12 km. Thus also this form of NEOS can be excluded, and we had already excluded such a large incompressibility from ISGMR studies [10, 11, 12, 13, 14, 15, 16, 17, 18, 19, 20, 21].

The situation becomes more complex when the interaction part of the symmetry energy is included, see Fig. 1.6, corresponding to the cases of table 1.1. Recall that all NEOS have $K = 225$ MeV unless otherwise indicated. Most cases are excluded by the NS observations and in particular the (6) and (7) NEOS which exhibit a phase transition at high densities. Notice the striking difference between case (5) and (6), derived from the same symmetry energy, but the first displaying a QLG and the second a QGP. These results together with the massless QGP result would suggest that the NS properties are mainly dependent on the EOS at a nuclear level.

But this is of course not the entire story, we could for instance change the neutron concentration [198, 199, 200, 201].

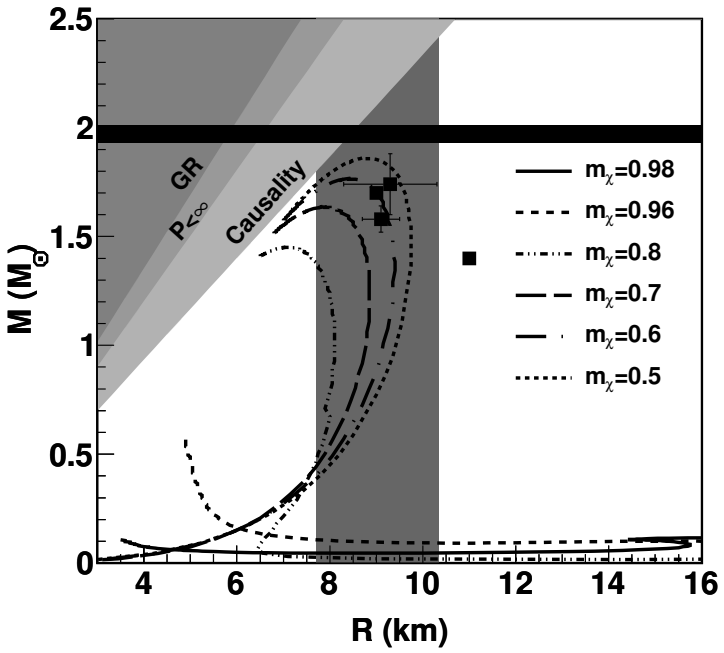

Figure 1.7: Neutron star mass-radius relations for case (6) with different $m_\chi = 0.98, 0.96, 0.8, 0.7, 0.6, 0.5$. The data points are from [38, 40, 41]. The radius band is from [43].

In Fig. 1.7 the NS mass-radius relation is now obtained for the NEOS, case (6), which undergoes a phase transition at $\rho = 4.4\rho_0$. The concentration m_χ is now varied which results in larger NS masses when including more and more protons. Eventually, the observations could be reproduced for a suitable choice of the concentration and its critical value, which, as we have seen, is also dependent on the symmetry energy. Qualitatively we could expect that the high density region of the NS might be in the

form of a QGP and, depending on the m_χ reached, the NS might become unstable. Of course other effects, such as strange matter [159], a first order (or a cross-over) rather than a second order phase transition, can complicate the subject further, thus it is extremely important that the ingredients entering the NEOS for $m_\chi \neq 0$ be strongly constrained in a similar fashion that has been done through GMR studies.

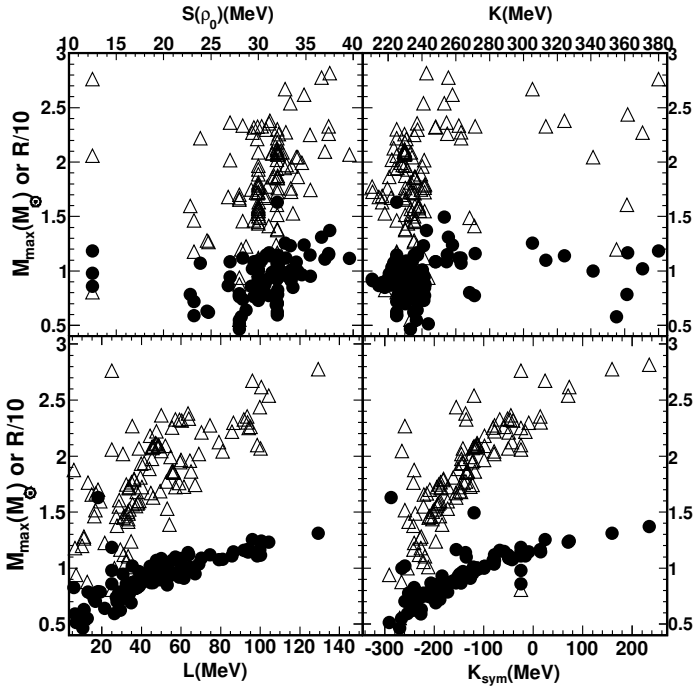

Figure 1.8: The results for 159 Skyrme NEOS in table 1.1 and refs. [10, 94, 95, 96, 97, 98, 99, 100, 101, 102, 103, 104, 105, 106, 107, 108, 109, 110, 111, 112, 113, 114, 115, 116, 117, 118, 119, 120, 121, 122, 123, 124, 125, 126, 127, 128, 129, 130, 131, 132, 133, 134, 135, 136, 137, 138, 139, 140, 141, 142]. The open triangles are the maximum masses and the solid circles are the corresponding reduced radii (divided by 10 km) of neutron stars.

In Fig. 1.8 we recap different calculations using Skyrme forces found in the literature [10, 94, 95, 96, 97, 98, 99, 100, 101, 102, 103, 104, 105, 106, 107, 108, 109, 110, 111, 112, 113, 114, 115, 116, 117, 118, 119, 120, 121, 122, 123, 124, 125, 126, 127, 128, 129, 130, 131, 132, 133, 134, 135, 136, 137, 138, 139, 140, 141, 142], together with the cases discussed in previous figures. The detail expressions of Skyrme NEOS and different quantities, i.e. P, K, $S(\rho)$, L, K_{sym} are reported in Appendix E. The NS radius is given in unit of 10 km which is in the region of the observed ones. No clear dependence on the incompressibility and the symmetry energy is observed, while some linear relation is observed as function of L and K_{sym} [31, 44, 76, 201]. In particular the NS observed values seem to favor $L > 30$ MeV and $K_{sym} > -150$ MeV. Such constraints are however not so strong, as we have seen above when changing some parameters in the NEOS (e.g. concentration), which suggests that the relevant quantities should be defined at higher densities. However, all these physical quantities can be constrained using heavy-ion collisions varying the concentration and the densities reached. These studies must be complemented with ground state studies of exotic nuclei.

1.6 Organization of Dissertation

The remainder of the dissertation is organized as follows. In chapter 2, we briefly review some of the features and differences of the microscopic simulation models used in the nuclear physics research. We give a detailed introduction to the Constrained Molecular Dynamics (CoMD) model and the modified version CoMD$_\alpha$ because our analysis is based on their simulation data. In chapter 3, we review the thermometers used to extract temperatures and study the caloric curves and the methods used to extract densities of nuclear matter in heavy-ion collisions. We also introduce a new thermometer including the genuine quantum nature of particles, i.e. fermions follow-

ing Fermi-Dirac distribution and bosons following Bose-Einstein distribution, based on the quadrupole momentum fluctuations and multiplicity fluctuations. It enables us to calculate the temperature and density of particle in the same quantum framework. Then we apply the new thermometer to fermions from CoMD simulation at low temperature approximation. In chapter 4, we outline the numerical calculation of densities and temperatures of fermions within the quantum approach with data from CoMD simulations. Then we compare the results with the ones from low temperature approximation to test the validity of the low temperature approximation in Fermi systems. In chapter 5, we explore the new thermometer even more, we consider the Coulomb correction to extract the density and temperature for fermions. In chapter 6, we turn to focus on bosons produced in the heavy-ion collisions. We show how to extract the temperature and density of bosons within the quantum approach. We apply the new thermometer to analyze the CoMD and CoMD$_\alpha$ simulation data. In chapter 7, similar to the fermion case in chapter 5, we modify our method to take into account distortions due to Coulomb field for bosons. Finally in chapter 8, we summarize the results and conclusions of this work. Appendices include the derivation details of the equations used in this dissertation.

2. REVIEW OF MICROSCOPIC SIMULATION MODELS*

We will use model results in the following chapters. In this chapter we will recall some of their features and differences. Review papers exist and we refer to those for details [8, 76, 78, 79, 80, 81, 84, 85, 86, 88, 89, 202, 203, 204, 205, 206, 207].

Ground state description of nuclei are well described within Shell model calculations [208, 209, 210] or more involved microscopic Hartree-Fock (HF) [211, 212]. Correlations can be included at some level within the Hartree-Fock-Bogoliobuv (HFB) method [210, 213, 214] and are necessary for the correct description of nuclei. For time dependent problems, i.e. heavy-ion collisions at low beam energy, Time Dependent HF (TDHF) has been widely used with a good reproduction, for instance of fusion cross sections [3, 215, 216]. At high bombarding energies, TDHF becomes inadequate since two body correlations are relevant and should be included [81]. The Wigner transform of TDHF gives the Vlasov equation in the limit $\hbar \to 0$ [217]. The Vlasov equation is easy to handle numerically and can be extended to include a two body collision term which takes into account the Pauli principle. The ground state of the nucleus in the Vlasov equation is simply obtained starting from a Fermi gas model and including a mean-field, Coulomb term and surface corrections. The latter ingredients are similar to those used in TDHF, but at variance with TDHF in that there is not a real minimization procedure for the ground state. Since we are dealing with one body dynamics, it means that the Liouville theorem is satisfied already at the one-body level. If the initial state is built in such a way to satisfy the Pauli

*Part of this chapter is reprinted with permission from "The many facets of the (non-relativistic) Nuclear Equation of State" by G. Giuliani, H. Zheng, A. Bonasera, 2014. Progress in Particle and Nuclear Physics 76, 116-164, Copyright 2014 by Elsevier B.V. and part of this chapter is reprinted with permission from "Density and temperature of bosons from quantum fluctuations" by Hua Zheng, Gianluca Giuliani, Aldo Bonasera, 2012. Nuclear Physics A 892, 43-57, Copyright 2012 by Elsevier B.V.

principle, then the Liouville theorem ensures that it is never violated [8]. This is true even after the inclusion of the collision term, since Pauli blocking is explicitly taken into account after each nucleon-nucleon collision.

The method used to solve the Vlasov equation due to Wong [218, 219, 220, 221] is called the test particles method (tp). It consists in writing the one body distribution function $f(\mathbf{r}, \mathbf{p}, t)$ as, in principle, an infinite sum of δ functions in coordinate and momentum space. The substitution of this ansatz in the Vlasov equation results in the classical Hamiltonian equations of motion of the test particles moving under the influence of the mean field and the Coulomb potential.

Different (numerical) methods of solving the Vlasov equation plus collision term have given rise to different names that can be found in the literature: Vlasov-Uheling-Uhelenbeck (VUU) [81, 222, 223, 224], Boltzmann-Uheling-Uhelenbeck (BUU) [8], Boltzmann-Nordheim-Vlasov (BNV) [225, 226, 227, 228]. A particular solution of the Vlasov equation, dubbed Landau-Vlasov (LV), was proposed by C. Gregoire and collaborators using Gaussian instead of δ functions for the test particles [204, 205].

Aichelin and Stöcker proposed to use one test particle per nucleon and described the nucleon as Gaussian distributions in phase space [80, 204, 205, 229, 230, 231], and this method was dubbed Quantum Molecular Dynamics (QMD). The name Quantum comes from the interpretation of the nucleon as a wave packet interacting through some suitable potential. Skyrme type potentials are sometimes used, which are often δ (contact) potential. When folding the δ potential with Gaussian distributions one obtains Gaussian interactions. This method is exactly equivalent to describing the nucleons as δ-functions (one per nucleon) interacting through a suitable Gaussian two body potential. This means that the system is completely classical, in fact the classical equations of motion are solved numerically. Thus quantum features are lost in this approach, but exact N-body correlations are included at the classical

level. This means that the model can, for instance in fragmentation studies, form d, α and any other kind of clusters, and all possible symmetries are broken. This is at variance with mean-field type of approaches which describe well only average trajectories and fail if instabilities are present. Some authors have tried to correct for this by including fluctuations in the Vlasov dynamics [232, 233]. Nevertheless, the problem of making light fragments remains in the (fluctuating) Vlasov equation and a possible way out is to stop the calculations at early times and use a coalescence approach in connection with an 'afterburner' which is a statistical model dealing with the decay of the hot source [202, 234, 235, 236, 237]. The possibility of correcting for this shortcoming in mean field dynamics makes molecular type approaches very appealing.

Many attempts to use Classical Molecular Dynamics (CMD) with a minimum of quantum requirements have been proposed [224, 238, 239]. In particular, including the Fermi motion results in very unstable systems. In fact, if we give a Fermi motion to the particles, the classical time evolution solving the N-body dynamics brings classical correlations. Now the Liouville theorem is satisfied at the N-body level and the classical correlations can mimic a classical Boltzmann collision term. One can prove this rigorously by averaging over many ensembles the classical N-body evolution [240]. The initial 'Fermi' momentum develops into a temperature T and the particles get high momenta and are emitted from the system. The emission will stop when the remaining particles have small momenta. The real ground state of a classical system is a solid. The situation might improve if one introduces momentum dependent potentials. The parameters of the interaction can be chosen in such a way that in the ground state the particles have zero velocity but finite momenta. A particular solution was introduced in refs. [241, 242] using the so-called Pauli potential, which is a Gaussian potential in phase space. The QMD model is very similar to

these approaches with some important differences. For momentum independent potentials the Fermi motion is partly included through the widths of the Gaussian used to describe a nucleon. In fact, folding the kinetic and potential energy terms with Gaussians gives rise to a term $A\frac{3\sigma_p^2}{2m}$ [80, 243], where σ_p is the width of the Gaussian in momentum space. If such a term is of the order of 20 MeV/A, then practically all the Fermi motion might be included in it. However, this term is a constant and it does not modify in any ways the equations of motion, which remain classical. This implies that the centroids of the Gaussians are at rest, i.e. the ground state is a solid and the real binding energy is much higher. This is one of the ambiguities that we have when we try to solve quantum problems using classical equations of motion. If we try to include a real Fermi motion in QMD, i.e. a kinetic energy is given to the centroids of the Gaussians, the classical correlations make the system unstable.

An elegant way to overcome this problem was first proposed by Feldmeier and it is dubbed Fermionic Molecular Dynamics (FMD) [88, 89, 244, 245, 246, 247, 248, 249]. He proposed to antisymmetrize the wave function to take into account the Pauli principle. This is done using Gaussian wave functions as in QMD plus antisymmetrization. The equations of motion are obtained through a minimization procedure as usual. In FMD a realistic potential which includes the hard core is used, together with the possibility that the Gaussian widths are time dependent as well. These most wished features lead to large CPU times needed for calculations, thus reducing the number of applications proposed so far [88, 89, 244, 245, 246, 247, 248, 249].

A more practical way to include the Pauli principle has been proposed in ref. [84], dubbed Antisymmetrized Molecular Dynamics (AMD), and essentially it consists in fixing the width of the Gaussians and including a collision term to mimic hard core collisions. The Pauli principle is enforced at all times. One further simplification was proposed in refs. [86, 243, 250, 251, 252, 253] where antisymmetrization is obtained

through a constraint on the phase space occupation to be less than one at all times, dubbed Constrained Molecular Dynamics (CoMD). A collision term, similar to AMD, is also included.

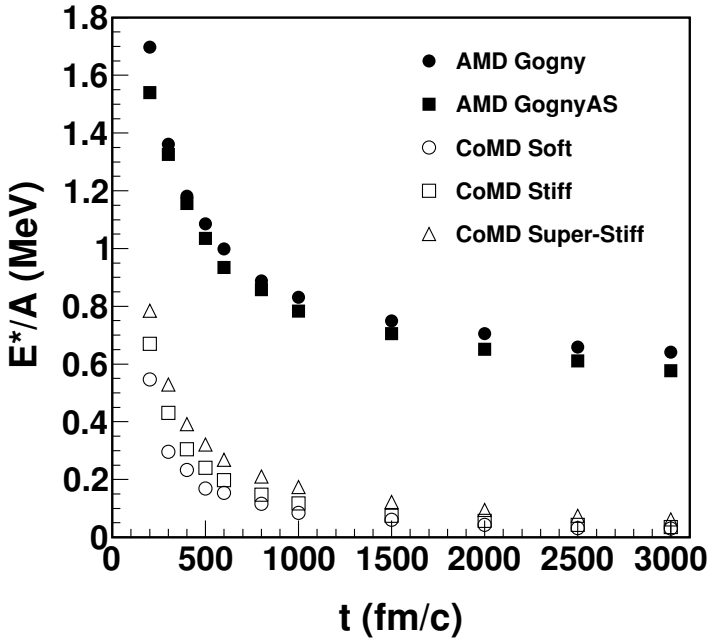

Figure 2.1: The excitation energy per nucleon from AMD and CoMD calculations versus time for different NEOS for $^{64}Zn + ^{64}Zn$ at 35 MeV/A. This figure is taken from ref. [254].

FMD, AMD and CoMD are all essentially classical in nature plus a constraint to take into account the Pauli principle. To make an analogy with the Bohr model of the atoms, one solves the classical equations of motion and chooses only the trajectories constrained by $\hbar$ [9]. Being classical, the problem of what to do with the width of the Gaussians when calculating the total energy remains. Even though this becomes

boring, we insist on this point since different choices are made by different authors on how to treat the Gaussian's width. This implies that the models could give different results even though nominally they use the same interaction and solve the same equations of motion. To be more specific let us write down equation (9) from ref. [84], the total energy of the system $\mathcal{H}(Z)$:

$$\mathcal{H}(Z) = \frac{\langle \Phi(Z)|H|\Phi(Z)\rangle}{\langle \Phi(Z)|\Phi(Z)\rangle} - \frac{3\hbar^2\nu}{2m}A + T_0(A - N_F(Z)). \tag{2.1}$$

Here, H is the hamiltonian, Z is the generalized coordinate of the wave packet $\Phi(Z)$, ν is its width in fm^{-2}, m is the nucleon mass, T_0 is a free parameter and $N_F(Z)$ is the number of fragments. In CoMD $T_0 = 0$, the contribution on the width of the Gaussian is subtracted as in Eq. (2.1) and the total energy is a constant of motion, i.e. $\mathcal{H}$ is independent of the coordinate Z and thus the time. In AMD, the width of the Gaussian is subtracted and a constant T_0 is added. The constant is fixed to reproduce the ground state binding energy of the nuclei and its value is $T_0 = 9.2$ MeV, while the contribution $\frac{3\hbar^2\nu}{2m} = 10$ MeV. The difference is not just 0.8 MeV for the two terms but more importantly the number of fragments $N_F(Z)$ that the authors parametrize as a smooth function of the coordinate Z. For nuclear ground states of course $N_F(Z) = 1$. This means that for a nucleon the correction is zero MeV, for d it amounts to $\frac{9.2}{2}$ MeV/A and converges to 9.2 MeV/A for large nuclei. With this ansatz, the authors are able to reproduce the binding energy of a large number of nuclei. However, the real binding energy of the system is the one with the T_0 term not included, since constant terms (in the ground state) do not give any contribution to the equations of motion. This choice has important consequences in time dependent problems, such as fragmentation. In such a case $N_F(Z)$ changes when fragments are formed which results in a change of the total

energy. The 'trick', as the authors define it, is to modify the kinetic energy of the particles which are emitted [84] in order to conserve the initial total energy of the system. The extra energy is randomly distributed to the nucleons in some AMD versions or to the fragments in some other versions. The use of this constant has important consequences as we have seen in the calculated nuclear ground states, we might expect that a similar effect will arise when calculating excitation energies. Results of a calculation for the system and the beam energy indicated are reported in Fig. 2.1 [254]. The excitation energy per nucleon versus time is plotted for AMD and CoMD calculations using different NEOS. The two models give drastically different results as drastically different choices are adopted in the models. In CoMD the Fermi motion is given by the kinetic energy of the Gaussians and *not* by its width and the ground state of the nuclei is obtained for a given NEOS by fixing the width parameters and a surface interaction [86, 243, 250, 251, 252, 253]. None of those ingredients are relevant for the calculation of the excitation energy which becomes negligible after a few hundred fm/c. In contrast, AMD calculations display an almost constant value for very long times and systematically higher than CoMD due to the different assumptions and the inclusion of the parameter T_0, Eq. (2.1). This feature must be taken into account also when using 'hybrid' models, i.e. when AMD, CoMD or other models, are stopped at a certain time and an afterburner for the decay from excited states is coupled to them. Usually CoMD calculations are followed for a long time (even up to 60000 fm/c for fission [255] by choice of the authors). These differences should be kept in mind when trying to derive properties of the NEOS from a comparison to experimental data. In the following we are going to rely heavily on the CoMD model which was proposed originally by my supervisor, thus the discussion above is biased, different points of view can be found from the literature [84, 88, 244].

We will show more details about CoMD. In the CoMD model [86, 243, 250, 251, 252, 253], each nucleon is described by a Gaussian wave packet

$$f_i(\mathbf{r},\mathbf{p}) = \frac{1}{(2\pi\sigma_r\sigma_p)^3} e^{-\frac{(\mathbf{r}-\langle\mathbf{r_i}\rangle)^2}{2\sigma_r^2}-\frac{(\mathbf{p}-\langle\mathbf{p_i}\rangle)^2}{2\sigma_p^2}}, \tag{2.2}$$

where $\langle\mathbf{r_i}\rangle$ and $\langle\mathbf{p_i}\rangle$ are the centroids of position and momentum of ith nucleon, respectively. σ_r and σ_p are the dispersions in the coordinate and momentum space, respectively. They satisfy the minimum uncertainty relation

$$\sigma_r\sigma_p = \frac{1}{2}\hbar. \tag{2.3}$$

The effective interaction V adopted in CoMD is

$$V = V^{vol} + V^{(3)} + V^{sym} + V^{surf} + V^{coul}. \tag{2.4}$$

By defining the superimposition integral ρ_{ij} as

$$\rho_{ij} \equiv \int d^3r_i d^3r_j \rho_i(\mathbf{r_i})\rho_j(\mathbf{r_j})\delta(\mathbf{r_i}-\mathbf{r_j}), \tag{2.5}$$

$$\rho_i \equiv \int d^3p f_i(\mathbf{r},\mathbf{p}), \tag{2.6}$$

the terms in Eq. (2.4) can be written as

$$V^{vol} = \frac{t_0}{2\rho_0}\sum_{i,j\neq i}\rho_{ij}, \tag{2.7}$$

$$V^{(3)} = \frac{t_3}{(\mu+1)\rho_0^\sigma}\sum_i(\sum_{j\neq i}\rho_{ij})^\sigma, \tag{2.8}$$

$$V^{sym} = \frac{a_{sym}}{2\rho_0}\sum_{i,j\neq i}[2\delta_{\tau_i,\tau_j}-1]\rho_{ij}, \tag{2.9}$$

$$V^{surf} = \frac{C_s}{2\rho_0} \sum_{i,j\neq i} \nabla^2_{\langle \mathbf{r_i} \rangle}(\rho_{ij}), \tag{2.10}$$

$$V^{coul} = \frac{1}{2} \sum_{i,j\neq i(i,j\in protons)} \frac{e^2}{|\langle \mathbf{r_i} \rangle - \langle \mathbf{r_j} \rangle|} erf(\frac{|\langle \mathbf{r_i} \rangle - \langle \mathbf{r_j} \rangle|}{2\sigma_r}). \tag{2.11}$$

In the above relations τ_i indicates the isospin degree of freedom and σ has been fixed to $\frac{7}{6}$. The V^{vol} and $V^{(3)}$ are the two-body potential and the so-called three-body potential, respectively. The values of t_0 and t_3 have been fixed to -356 MeV and 303 MeV. These values reproduce the saturation density ρ_0 and binding energy for symmetric nuclear matter with an incompressibility of 200 MeV. The third term represents the symmetry term with $a_{sym} = 32$ MeV. C_s in the fourth term (surface potential) is a free parameter to reproduce the nuclear radii. The fifth term is the Coulomb potential.

The equations of motion of $\langle \mathbf{r_i} \rangle$ and $\langle \mathbf{p_i} \rangle$ are derived using the time-dependent variational principle which gives

$$\langle \dot{\mathbf{r}}_\mathbf{i} \rangle = \frac{\partial H}{\partial \langle \mathbf{p_i} \rangle}, \quad \langle \dot{\mathbf{p}}_\mathbf{i} \rangle = -\frac{\partial H}{\partial \langle \mathbf{r_i} \rangle}, \tag{2.12}$$

where $H = \sum_i \frac{\langle \mathbf{p_i^2} \rangle}{2m} + V$. The cluster identification mechanism in CoMD is minimum spanning tree (MST) in coordinate space. If the distance between two particles is less or equal $2.4\sigma_r$, then the two particles belong to the same cluster, otherwise they are in different clusters. Of course such a method is exact when identifying the clusters at very large times.

The Pauli principle is taken into account in two ways in CoMD: one is the Pauli blocking of the final state of the two-body collision and the other is the constraint which brings into the system the Fermi motion in a stochastic way. The starting

point of the constraint is the requirement

$$\bar{f}_i \leq 1, \quad (\text{for all } i) \tag{2.13}$$

and

$$\bar{f}_i \equiv \sum_j \delta_{\tau_i,\tau_j}\delta_{s_i,s_j}\int_{h^3} f_j(\mathbf{r},\mathbf{p})d^3rd^3p, \tag{2.14}$$

where s_i is the spin degree of freedom of nucleon i. The integral is performed in an hypercube of volume h^3 in the phase space centered around the point $(\langle\mathbf{r_i}\rangle, \langle\mathbf{p_i}\rangle)$ with size $\sqrt{\frac{2\pi\hbar}{\sigma_r\sigma_p}}\sigma_r$ and $\sqrt{\frac{2\pi\hbar}{\sigma_r\sigma_p}}\sigma_p$ in the coordinate and momentum space, respectively. At each time step and for each particle i the phase space occupation $\bar{f}_i$ is checked. If $\bar{f}_i$ is greater than 1, an ensemble K_i of the near particles (including the particle i) is determined within the distance $3\sigma_r$ and $3\sigma_p$ in the phase space. Then we change randomly the momenta of the particles belonging to the ensemble K_i in such a way that for the newly generated sample the total momentum and the total kinetic energy is conserved ("many-body elastic scattering"). The new sample is accepted only if it reduces the phase space occupation $\bar{f}_i$. To handle the Pauli blocking in the collision term is straightforward from the constraint. For each NN collision we evaluate the occupation $\bar{f}_i$ after the elastic scattering. If such functions for both particles are less than 1, the collision is accepted, otherwise rejected. Since two protons and two neutrons with different spins are not subject to Pauli blocking, α clustering is enhanced.

The important ingredient which is missing in the model is the possibility of boson-boson collisions (α-α, d-d, etc.) and correlations. Therefore, we propose a modification of the collision term in CoMD to include the possibility of α-α collisions. We will refer to the modified version as CoMD$_\alpha$. We use a similar method as the cluster

identification to identify α particle at each time step. First one particle is chosen, then the three closest particles with the correct values of spin and isospin (i.e. two protons and two neutrons with opposite spin respectively) are selected within a radius of $2.4\sigma_r$ (the value used in cluster identification) in coordinate space. If all the conditions are fulfilled, we identify the four particles as an α. We run over all the particles and determine all the possible α particles. Each particle can only belong to one α. At each time step, we search for the α-α pair whose distance is smaller than 2.5 fm. We follow the mean free path method [78, 256, 257] and define a collision probability for the α-α pair:

$$\Xi_{ij} = 1 - e^{-\sqrt{1-\frac{V_c}{E_k}}\sigma_{cs}\Pi\rho(r_i)v_{ij}dt}, \tag{2.15}$$

where σ_{cs} is the cross section, $\Pi = (1+\bar{f}_1)(1+\bar{f}_2)$ is the Bose-Einstein factor and $\bar{f}_i$ is the average occupation probability for α, $i = 1, 2$, $\rho(r_i)$ is the local density, v_{ij} is the relative velocity of the two α particles, dt is the time step and $\sqrt{1-\frac{V_c}{E_k}}$ is the Coulomb barrier correction factor where V_c is the Coulomb energy between the two αs and E_k is their relative kinetic energy. For simplicity, we take σ_{cs} as the α-α geometric cross section. Notice that in such an approximation, the strong resonances which lead to the formation of ^8Be are not included. We expect that such resonances will increase the α yields from ^8Be decay. However, we have not been able to implement this effect in the present model. If an α-α collision occurs, we calculate the Bose-Einstein factor Π before the collision and Π' after the collision. If $\Pi' > \Pi$, the collision will be accepted, otherwise, rejected. Thus the Bose factors $(1+\bar{f}_i)$ increase the probability of collision in contrast to the Pauli blocking factors [8, 78]. Meanwhile, if the α particle does not suffer any collision in that time step, one of its nucleons can collide with another nucleon subject to Pauli blocking. This

might break the αs into nucleons.

3. THE QUANTUM THERMOMETER*

In this chapter, we will review the thermometers used to extract temperatures and study the caloric curves in heavy-ion collisions. The methods used to extract densities of nuclear matter in the collisions are reviewed as well. But the thermometer and the method to calculate density are either both with classical assumptions or one with quantum and the other with classical assumptions. Recently in [258], a new thermometer was proposed based on the quadrupole momentum fluctuation estimated from an event by event determination of fragments with classical assumption. We extend this new thermometer including the genuine quantum nature of particles, i.e. fermions following Fermi-Dirac distribution and bosons following Bose-Einstein distribution, based on the quadrupole momentum fluctuations and multiplicity fluctuations. We will dub this extended new thermometer as quantum thermometer. It enables us to calculate the temperature and density of particle in the same quantum framework. Then we will apply the quantum thermometer to fermions from CoMD simulation at low temperature approximation. We leave the bosons case in the following chapters.

3.1 The Thermometers and Methods to Extract Densities

In recent years, the availability of heavy-ion accelerators which provide colliding nuclei from a few MeV/A to GeV/A and new and performing 4π detectors, has fueled a field of research loosely referred to as Nuclear Fragmentation [8, 78, 79]. Fragmentation experiments could provide information about the nuclear matter properties

*Part of this chapter is reprinted with permission from "The many facets of the (non-relativistic) Nuclear Equation of State" by G. Giuliani, H. Zheng, A. Bonasera, 2014. Progress in Particle and Nuclear Physics 76, 116-164, Copyright 2014 by Elsevier B.V. and part of this chapter is reprinted with permission from "Density and temperature of fermions from quantum fluctuations" by Hua Zheng, Aldo Bonasera, 2011. Physics Letters B 696, 178-181, Copyright 2010 by Elsevier B.V.

and constrain NEOS [91]. Even though a large variety of experimental data and refined microscopic models exist, to date there not exist a method to determine densities and temperatures reached during the collisions, which takes into account the genuine quantum nature of the system.

There are three conventional thermometers used for nuclear studies. These are the slopes of the kinetic energy spectra, discrete state population ratios of selected isotopes and double isotopic yield ratios [79, 259]. They are used to measure the temperature in the heavy-ion collisions and extract caloric curve information. All of them assume that the particles follow the Maxwell-Boltzmann distribution, i.e. the classical limit. For the slope of the kinetic energy spectrum thermometer, the temperature is extracted by fitting the particle kinetic energy spectrum assuming a Maxwell-Boltzmann distribution and appropriate barrier. For the discrete state population ratio thermometer, the temperature is extracted from the yields of different excited states in a single isotope (bound or unbound) assuming a Maxwell-Boltzmann distribution $Y_i \sim e^{-E/T}$. For the double isotopic yield ratio thermometer, the temperature is extracted from the yield ratio of different kind of produced isotopes. The double isotopic yield ratio thermometer, which was devised by Rubbino and collaborators in 1985, is often used by experimental groups and among theorists [181, 260, 261, 262, 263, 264, 265]. Classically, the yield distribution can be calculated in the grand canonical ensemble, for a system in equilibrium [1, 7, 51]. The well known Saha equation gives the ratio of the density of two different fragments from the ratio of their yields [260]:

$$\frac{Y_1}{Y_2} = \frac{\rho(A_1, Z_1)}{\rho(A_2, Z_2)} = (\frac{A_1}{A_2})^{\frac{3}{2}} (\frac{\lambda_T^3}{2})^{A_1 - A_2} \frac{2s_1 + 1}{2s_2 + 1} \rho_p^{Z_1 - Z_2} \rho_n^{N_1 - N_2} \exp[\frac{B_1 - B_2}{T}], \qquad (3.1)$$

where $\lambda_T = \frac{h}{\sqrt{2\pi m T}}$ is the thermal wavelength, $\lambda_T^3 = 4.206 \times 10^3 T^{-\frac{3}{2}}$ fm^3, s_i are

the spins and B_i are the binding energies of the i-fragment. The detailed derivation of this equation is given in appendix F. The ratio above depends on the unknown densities of p and n, as well as the temperature. We can write a similar ratio for other fragments, for instance:

$$\frac{Y_3}{Y_4} = \frac{\rho(A_3, Z_3)}{\rho(A_4, Z_4)} = (\frac{A_3}{A_4})^{\frac{3}{2}} (\frac{\lambda^3_{T,\mathcal{N}}}{2})^{A_3 - A_4} \frac{2s_3 + 1}{2s_4 + 1} \rho_p^{Z_3 - Z_4} \rho_n^{N_3 - N_4} \exp[\frac{B_3 - B_4}{T}]. \quad (3.2)$$

Now we have two equations but still three unknowns. A particular method to obtain the temperature was devised by Rubbino and collaborators [260], and consists in taking the ratio of Eq. (3.1) and Eq. (3.2):

$$\rho_p^{DZ} \rho_n^{DN} = \frac{\frac{Y_1 Y_4}{Y_2 Y_3}}{(\frac{A_1 A_4}{A_2 A_3})^{\frac{3}{2}} (\frac{\lambda^3_{T,\mathcal{N}}}{2})^{DA} \frac{(2s_1+1)(2s_4+1)}{(2s_2+1)(2s_3+1)} \exp[\frac{DB}{T}]}, \quad (3.3)$$

where $Df = (f_1 + f_4) - (f_2 + f_3)$. By imposing $DZ = (Z_1 + Z_4) - (Z_2 + Z_3) = 0$ and $DN = (N_1 + N_4) - (N_2 + N_3) = 0$ we can eliminate the densities from Eq. (3.3). The equation can be inverted to obtain T, since the binding energies of the fragments are well known. This is a very elegant method and let us obtain the temperature once the fragments yields are known for a given excitation energy and a source size (mass and charge). However, different particles ratios might be taken and it is not guaranteed that for given source condition, they will provide the same temperature. Actually, different fragments might form during the time evolution at different densities [266, 267] or temperatures, which makes the freeze out assumption questionable. From another point of view, assuming a freeze out, the hot fragments have different excitation energy, thus the final yields are distorted by secondary evaporation which results in different temperatures for different fragment double ratios. Of course, another natural reason why different ratios result in different

temperatures, is because the system is quantal and not classical, furthermore particles with different quantum statistics, i.e. bosons or fermions, might be mixed in the double ratio.

Within the same classical approximation we can derive the density of protons and neutrons as well, and hence of all particles. For instance let us consider the double ratio formed with p, n, t and ^3He which are all fermions, but still using classical statistics.

$$\frac{\rho_p}{\rho_n} = \frac{Y(p)}{Y(n)}, \tag{3.4}$$

$$\frac{\rho_p}{\rho_n} = \exp[\frac{0.765}{T}]\frac{Y(^3He)}{Y(t)}, \tag{3.5}$$

$$\rho_p\rho_n = 4.35 \times 10^{-8}T^3 \exp[-\frac{7.716}{T}]\frac{Y(^3He)}{Y(p)}, \tag{3.6}$$

$$\rho_p\rho_n = 4.35 \times 10^{-8}T^3 \exp[-\frac{8.481}{T}]\frac{Y(t)}{Y(n)}, \tag{3.7}$$

$$T = \frac{0.765}{\ln\left[\frac{Y(p)Y(t)}{Y(n)Y(^3He)}\right]}. \tag{3.8}$$

From the set of Eqs. (3.4, 3.5, 3.6, 3.7, 3.8), one can easily obtain the p and n densities and the temperature T. Similarly, it can be done for other particle double ratios [260]. Notice that in experiments, usually the neutrons are not measured and they are inferred by assuming that the ratio of p to n is equal to the ratio ^3He to t. This is not strictly correct since the binding energies of ^3He and t are not exactly the same. But this method to calculate density is only applicable in the very low density region and high temperatures, e.g. $5 \times 10^{-4} fm^{-3}$, where the classical limit might be valid [268].

The failure of the classical thermal model [268] suggests that there might be another mechanism for cluster formation at play at higher densities. In heavy-ion

collisions the excitation energy or temperature might be high and the system expands quickly. Cluster formation might occur during the expansion in presence of a third body. For instance, the mechanism of deuterium formation might be $p + n \rightarrow d + \gamma$, but such a mechanism is too slow as compared to the expansion time of the nucleus [82, 269, 270]. More phase space is available, thus larger reaction rates, in presence of a third body, for instance $p + n + N \rightarrow d + N$, in this process the extra energy and momentum in the fusion process are taken by a third particle [78, 207]. This is the basis of the coalescence model and essentially we assume that if two particles are within a sphere of radius P_0 in momentum space, they can coalesce to form a new species. If, in the experiments, we can measure precisely the momentum or energy distributions of fragments of mass A and charge Z, plus the distributions of protons and neutrons, we can derive the value of P_0 [269, 270]. Neutrons are usually not measured, thus one uses the proton distribution and a correction for Coulomb [271]. With all those assumptions and simplifications we can write a relation from which P_0 can be derived from the energy distributions of the fragments:

$$\frac{d^2N(Z,N,E_A)}{dE_A d\Omega} = R_{np}^N \frac{1}{N!Z!A}\left(\frac{4\pi P_0^3}{3[2m^3(E-E_c)]^{0.5}}\right)^{A-1}\left(\frac{d^2N(1,0,E)}{dEd\Omega}\right)^A. \qquad (3.9)$$

R_{np}^N is the ratio of neutrons to protons of the source, E_c is the Coulomb correction. The detailed derivation of this equation is given in appendix F. Thus for each fragment type, d, t, etc., a value of P_0 can be obtained. Notice that the coalescence model takes into account the presence of other bodies when fragments are formed. Pauli blocking is one of those effects which could be taken into account indirectly through the value of P_0 [268]. Compared to the classical thermal model, coalescence occurs at relatively high densities and temperatures. It does not occur, for instance, during the big-bang expansion, since densities are too low at the time when nuclear

processes are dominant [24, 25, 26, 27, 269, 270]. It might occur in relativistic heavy-ion collisions when the quarks and gluons coalesce to form hadrons [272, 273].

A further variation of the coalescence model, was proposed by Natowitz and collaborators [266, 267, 274, 275], which consists in deriving the parameter P_0 as function of the velocity of the particles in the reference frame of the emitting source after correcting for Coulomb. This is like following the time evolution of the system, in fact to higher velocities correspond shorter times and higher temperatures. The question now is how to derive the density of the system from the knowledge of P_0. A non-equilibrium model was proposed in ref. [276] which assumes the knowledge of the fragment wave function, say the deuteron in the source, and connects P_0 to its volume in coordinate space. A less general approach, but more suitable to our goals was proposed by Mekjian [269, 270] and assumes thermal and chemical equilibrium:

$$V = \frac{3h^3}{4\pi P_0^3}[\frac{Z!N!A^3}{2^A}(2s_A+1)e^{\frac{B_A}{T}}]^{\frac{1}{A-1}}. \tag{3.10}$$

B_A and s_A are the ground state binding energy and the spin of the fragment respectively. The detailed derivation of this equation is given in appendix F. The temperature T can be determined using other methods such as the double ratio method discussed before in this section [261, 262, 266, 267, 274, 275, 277]. From the experiment we know the average multiplicities of the particles as well, thus the density can be obtained

$$\rho = \frac{\bar{N}}{V}, \tag{3.11}$$

for each source velocity together with the temperature from the double ratio method [266, 267, 274, 275].

The MSU group used the double ratio thermometer as well to extract the system

temperature but they introduced empirical corrections for different double ratios to correct for the secondary decay effects [261, 262]. They used different strategy to calculate the volume of the system rather than coalescence model. They calculated two particle correlations which took into account quantum effects [278, 279, 280] to extract the size of the systems R. If we assume the nuclear matter region is a sphere, the volume of the system is

$$V = \frac{4\pi}{3} R^3. \tag{3.12}$$

Then the density can be calculated from Eq. (3.11).

The Moretto group applied another thermometer to their experimental data. They used the level density of a modified Fermi gas but the coefficient is a function of excitation energy [264, 281]

$$E_s^* = \frac{1}{8} \frac{1}{1 + \frac{A_s E_s^*}{E_s^{bind}}} T^2, \tag{3.13}$$

where $E_s^{bind} \approx 8A_s$ MeV is the binding energy of the source. Since the excitation energy can be measured in experiment, they can calculated the temperature with Eq. (3.13). To extract the density information, they started from the modified Fisher model which was proposed in [175, 282] and corrected for finite size effects in the mass formula [172, 173, 174]. Then they fit their experimental data with the Guggenheim formula [169] which is universal for real gases from chemistry and extrapolate it to $T = 0$. In this way, they can derive the density. The details can be found in [172, 173, 174].

In [258], a new thermometer is proposed based on the quadrupole momentum fluctuations of particles in the center of mass frame of the fragmenting source. The

quadrupole momentum is defined as

$$Q_{xy} = p_x^2 - p_y^2, \tag{3.14}$$

in a direction transverse to the beam axis (z-axis) to minimize non-equilibrium effects. Then the quadrupole momentum fluctuation is calculated

$$\begin{aligned} \langle (\Delta Q_{xy})^2 \rangle &= \langle Q_{xy}^2 \rangle - \langle Q_{xy} \rangle^2 \\ &= \langle Q_{xy}^2 \rangle. \end{aligned} \tag{3.15}$$

$\langle Q_{xy} \rangle = 0$ is because of the symmetry between p_x and p_y. In [258], a Maxwell-Boltzmann distribution $f(p)$ for particles is assumed

$$\begin{aligned} \langle Q_{xy}^2 \rangle &= \frac{\int d^3p (p_x^2 - p_y^2)^2 f(p)}{\int d^3p f(p)} \\ &= (2mT)^2, \end{aligned} \tag{3.16}$$

where m is the mass of the particles. The left hand side of Eq. (3.16) can be extracted from experimental data based on event by event analysis. Therefore temperature of the particles can be obtained. For the density, they used the Fermi gas assumption $E^* = aT^2 = \frac{A}{13.3}(\frac{\rho}{\rho_0})^{-2/3}T^2$. Since the temperature is extracted from quadrupole momentum fluctuation and excitation energy is measured in experiment, the density can be calculated.

3.2 The Quantum Thermometer

The spirit of the Thomas-Fermi (TF) approximation [3] is to consider the density locally constant and derive the Fermi momentum for each density. This approximation can also be generalized at finite temperatures. Now we can try to 'invert' this

procedure, i.e. starting from some physical observables, average multiplicities, kinetic energies etc., can we derive the (local) density and temperature of the system? This is what have been done in the previous section assuming classical distributions. In the TF approximation we assume that the distribution is given by a finite temperature Fermi-Dirac. In nuclei we have fermions as well as bosons, d, α etc., thus we can generalize the approach to include bosons. In general the distribution function for elementary particles at temperature T is given by:

$$f(p) = \frac{1}{e^{[\varepsilon(p)-\mu]/T} \pm 1}, \tag{3.17}$$

where $\varepsilon(p) = \frac{p^2}{2m}$ and the chemical potential μ is connected to the density, '+' is for fermions and '-' is for bosons. The equation above refers to elementary particles and we can consider p and n as elementary particles at the excitation energies of interest in this dissertation. Other particles are composites, i.e. made of p and n, thus for instance an α particle is a boson made of fermions, thus the Pauli principle will play a role in all cases [283, 284, 285]. We will not discuss this problem further in this dissertation and we will consider them as elementary particles for illustration. For further discussion see [70, 283, 284, 285, 286].

Since we are dealing with heavy-ion collisions, where non-equilibrium effects are important, we should choose observables which can give the closest approximation to a 'temperature'. In the spirit of the fluctuation-dissipation theorem [1, 7, 51], looking at fluctuations gives the largest chaoticity, thus the closest approximation to an ergodic system. Of course chaoticity is not enough to ensure that the system is in thermal (and chemical) equilibrium, but it is probably the closest we can get. To think that we can get completely equilibrated events is a dream and we should settle for the closest we can get and, helped by models, correct for finite sizes, Coulomb and

dynamical effects. We will discuss the correction in the following chapters. In heavy-ion collisions, the produced particles do *not* follow classical statistics. Protons(p), neutrons(n), tritium etc. follow the Fermi statistics while, deuterium, alpha etc., even though they are constituted of nucleons, should follow the Bose statistics. It is easy for us to extend the quadruple momentum fluctuation thermometer taking into account quantum effects, we replace the Maxwell-Boltzmann distribution with the right distribution function for the studied particles in Eq. (3.16). Then the quadruple momentum fluctuation is

$$\langle Q_{xy}^2 \rangle = \frac{\int d^3p (p_x^2 - p_y^2)^2 f(p)}{\int d^3p f(p)}. \tag{3.18}$$

Eq. (3.17) contains two unknowns, T and μ, thus in order to fix them we need another observable in the same framework. We choose the multiplicity fluctuations of particles. A similar approach has also been applied to observe experimentally the quenching of fluctuations in a trapped Fermi gas [73, 74, 75] and the enhancement of multiplicity fluctuations in a trapped Bose gas [72]. From [1], we know that the multiplicity fluctuation is given by:

$$\langle (\Delta N)^2 \rangle = T(\frac{\partial \bar{N}}{\partial \mu})_{T,V}. \tag{3.19}$$

Eqs. (3.18, 3.19) are the foundations of the quantum thermometer.

To illustrate the strength of our approach, we apply the proposed method to the microscopic CoMD approach [86, 243, 250, 251, 252, 253] which includes fermionic statistics. We simulated $^{40}Ca + ^{40}Ca$ heavy-ion collisions at fixed impact parameter $b = 1$ fm and beam energies E_{lab}/A ranging from 4 MeV/A up to 100 MeV/A. Collisions were followed up to a maximum time $t = 1000$ fm/c in order to accumulate

enough statistics. Particles emitted at later times (evaporation) could affect somehow the results and this might be important especially at the lowest beam energies. The choice of central collisions was dictated by the desire to obtain full equilibration. This however, did not occur especially at the highest beam energies due to a partial transparency for some events.

In the following of this section, we will concentrate on fermions only and in particular p and n which are abundantly produced in the collisions thus carrying important information on the densities and temperatures reached. For bosons the results are a little bit more complicated but more interesting, since they might undergo Bose-Einstein condensate (BEC) [59, 60, 61, 62, 63, 64, 65, 66, 68, 69, 287]. If BEC could be somehow confirmed in HIC, it would open an interesting field of research since we have a system where fermions and bosons are somewhat mixed. We have some debate on the possibility of BEC started from the observation of Hoyle states [288, 289, 290, 291], α decay, large α yields, densities in HIC [266, 292, 293] and so on. We will discuss the bosons case in the following chapters. The density 'seen' by protons and neutrons refers to the gas component of the system for instance in a liquid-gas phase transition. The density of the bulk or the liquid could be inferred from a similar method but the interactions must be included [1, 7, 51]. Thus our approach is well justified for weakly interacting Fermi gases, i.e. when the gas densities are small compared to the ground state of the nucleus. As we will see this approximation is well supported by the results even at very small excitation energies where the nucleons are emitted from the surface of the nucleus which is at relatively small density. For higher excitation energies the nucleus breaks into pieces, with some large fragments which represent the liquid and very small ones, such as p and n which give the vapor part.

We substitute Fermi-Dirac distribution into Eq. (3.18) and calculate $\langle Q_{xy}^2 \rangle$ for

fermions. For the first step, we would like to derive an analytical formula for $\langle Q_{xy}^2 \rangle$. With low temperature approximation, we obtain

$$\begin{aligned} \langle Q_{xy}^2 \rangle &= (2mT)^2 \frac{4}{35} (\frac{\varepsilon_f}{T})^2 \left[1 + \frac{7\pi^2}{6} (\frac{T}{\varepsilon_f})^2 + O(\frac{T}{\varepsilon_f})^4 \right] \\ &= (2mT)^2 F_{QC}, \end{aligned} \tag{3.20}$$

where ε_f is the Fermi energy of the particles and F_{QC} is the quantum correction factor for fermions at low T approximation. The detailed derivation of this equation is given in appendix B. We have seen that the Fermi energy ε_f enters into Eq. (3.20).

Within the same low T approximation for $\langle Q_{xy}^2 \rangle$ and do the calculation for Eq. (3.19), we easily obtain

$$\frac{\langle (\Delta N)^2 \rangle}{\bar{N}} = \frac{3}{2} \frac{T}{\varepsilon_f} + O(\frac{T}{\varepsilon_f})^3. \tag{3.21}$$

The detailed derivation is also given in appendix B. Combing Eq. (3.20) with Eq. (3.21), we are able to calculate the quantum temperature for fermions and the Fermi energy ε_f. Then we can calculate the density using

$$\varepsilon_f = \frac{\hbar^2}{2m} (\frac{6\pi^2}{g})^{2/3} \rho^{2/3}, \tag{3.22}$$

where g is the degeneracy of the particle.

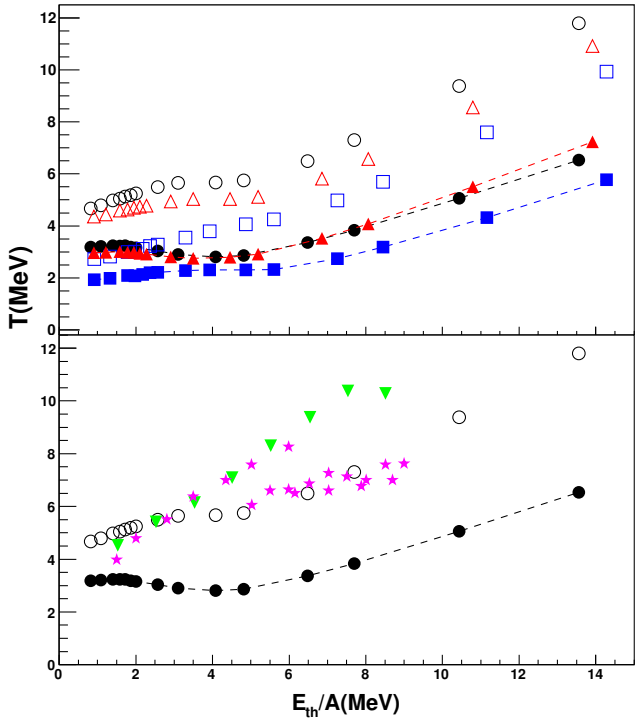

Figure 3.1: Temperature versus thermal energy per nucleon derived from quantum fluctuations (full symbols joined by dashed lines) compared to the classical case (open symbols). (Top) Circles refer to proton, squares to neutrons and triangles to protons and neutrons. (Bottom) Same as above for protons. Data: down triangles from classical quadrupole momentum fluctuations [258], star symbols from particle ratios [181].

In order to correct for collective effects as much as possible, we defined a 'thermal' energy as:

$$\langle \frac{E_{th}}{A} \rangle = \frac{E_{cm}}{A} - [\langle \frac{E_{p(n)}}{\bar{N}_{p(n)}} \rangle - \frac{3}{2} \langle \frac{E_{p(n)xy}}{\bar{N}_{p(n)}} \rangle] - Q_{value}, \tag{3.23}$$

where $\langle \frac{E_{p(n)}}{\bar{N}_{p(n)}} \rangle$ and $\langle \frac{E_{p(n)xy}}{\bar{N}_{p(n)}} \rangle$ are the average total and transverse kinetic energies (per nucleon) of protons (and/or neutrons). $Q_{value} = \frac{\bar{N}_{p(n)}}{Z(N)} 8$ MeV, similarly for protons

plus neutrons. 8 MeV is the average binding energy of a nucleon, Z (N) is the total charge (neutron) number of the system and $\bar{N}_{p(n)}$ is the average number of protons (neutrons) emitted at each beam energy. For a completely equilibrated system, the transverse kinetic energy (times 3/2) is equal to the total kinetic energy and the terms in the square brackets cancel. All the center of mass energy, $\frac{E_{cm}}{A}$, is converted into thermal energy (plus the Q_{value}). In the opposite case, say an almost complete transparency of the collision, the transverse energy would be negligible and the resulting thermal energy would be small. Our approximation will account for some corrections, and this will become more and more exact when many fragment types are included in Eq. (3.23) [258]. However, this approximation might be important in experiments where only some fragment types are detected or if, because of the time evolution of the system, different particles are sensitive to different excitation energies, for instance if some particles are produced early or late in the collision.

In Fig. 3.1 (top) we plot the estimated temperatures at various 'thermal' energies both for the quantum (full symbols) and classical approximations (open symbols). As we see the quantum case is systematically lower than the classical one. We also notice a difference if the T are estimated from the proton distributions (circles), or neutrons (squares) or the sum of the two (triangles). This is clearly a Coulomb effect which gets smaller as expected at higher energies as we will demonstrate more in detail below. The backbending observed at $T \approx 3$ MeV for all cases indicates a liquid-gas phase transition, in particular we observe that such a back-bending is more marked for the protons case as first discussed by Gross [294]. In the bottom part of Fig. 3.1 , we compare the protons results to experimental data. The down triangles are derived using the 'classical' quadrupole momentum fluctuations [258] thus should be very similar to our classical results and the agreement is reasonable at the lowest excitation energies. However, we stress that the experimental data were obtained

for different systems at a fixed 35 MeV/A beam energy. In particular projectile like fragments (PLF) were isolated and analyzed and the excitation energy was obtained from all fragments differently from Eq. (3.23). Thus there might be a mismatch in the abscissa and this could be especially important for large excitations. Also the detector acceptance might be important. Similar considerations apply to the data [181] obtained using double particle ratios (star symbols) [260]. In the latter case, classical approximations are used as well [260], the underlying assumption is that all those particles are sensitive to the same density and temperature. If T and ρ 'seen' by different particles are different, then the results give some kind of 'averaging'. Furthermore, the densities must be small and the temperatures high, i.e. $T/\varepsilon_f >> 1$, as stressed in the original proposal to measure temperatures from double ratios [260]. These classical validity conditions are not recovered in this work and most probably in the data since the measured temperatures in this beam energy regime are relatively small and different density estimates give still densities of the order of $(\frac{1}{3} - \frac{1}{6})$ of the ground state density of a nucleus [181, 258, 295]. In the top part of Fig. 3.1 we see that temperatures are different for protons and neutrons at a given excitation energy (clearly a Coulomb effect), thus we expect that other particles might give different T. This implies that different particle ratios might produce different results as well [181].

Using Eq. (3.20), we can easily show that, in the region of validity, the 'classical' T_{cl} is always larger than the 'quantum' temperature T

$$T_{cl} = \sqrt{\frac{4\varepsilon_f^2}{35} + \frac{2\pi^2}{15}T^2}. \tag{3.24}$$

A similar result has been found by Bauer [296] in 1995 in order to explain the large 'apparent' temperature observed in particles spectra. He stressed the crucial

influence of the Pauli blocking in the momentum distributions of nucleons emitted in heavy-ion collisions near the Fermi energy. In [296] a relation between the final (classical) temperature T'_{cl} and the input Fermi-Dirac T was found:

$$T'_{cl} \approx \frac{2\varepsilon_f}{5}[1 + \frac{5\pi^2}{12}(\frac{T}{\varepsilon_f})^2]. \tag{3.25}$$

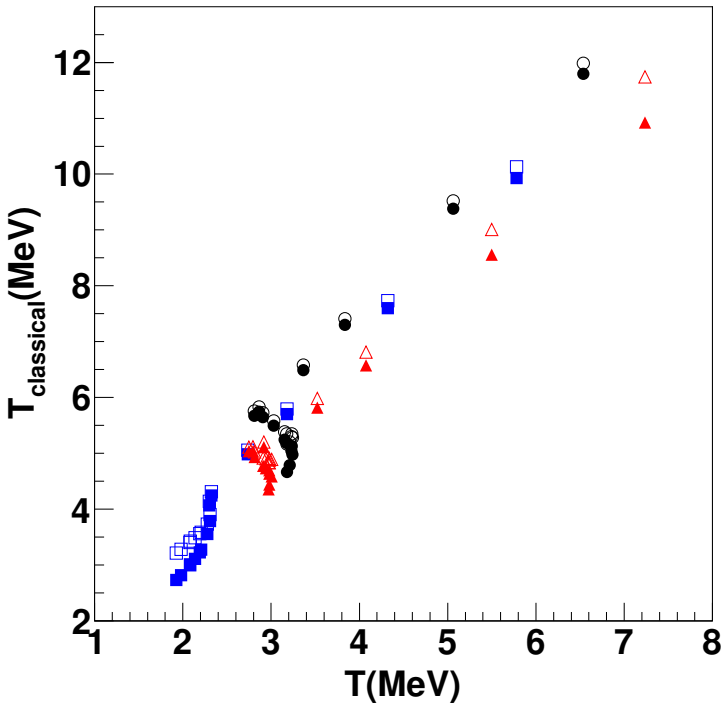

Figure 3.2: Classical temperatures versus quantum temperatures. Symbols as in Fig. 3.1, open symbols refer to Bauer's approximation, Eq. (3.25).

The ratio $\frac{T}{\varepsilon_f}$ entering the equations above can be directly obtained from Eq. (3.21). Even though Eqs. (3.24, 3.25) might look different at first sight, they give

very similar results as can be seen in Fig. 3.2 where the classical T_{cl} is plotted versus the quantum one. Bauer's approximation, Eq. (3.25), is given by the open symbols. The "difference" between the equations is minimized if one actually expands Eq. (3.24) to second order in $\frac{T}{\varepsilon_f}$. Thus the quantum temperatures are smaller than derived when fitting experimental results with a classical approximation. The reason of such small quantum temperatures is the Fermi energy entering Eq. (3.24) or Eq. (3.25).

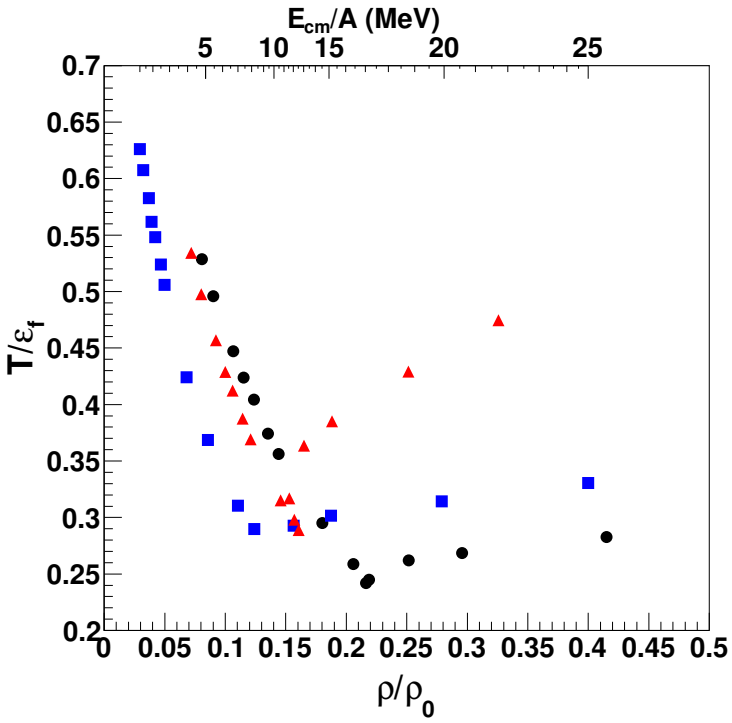

Figure 3.3: Temperature divided the Fermi energy versus density normalized to the ground state one derived from quantum fluctuations, Eqs. (3.20, 3.21). Symbols as in Fig. 3.1. The top energy scale refer to the neutron case.

In Fig. 3.3 we plot the ratio $\frac{T}{\varepsilon_f}$ directly obtained from Eq. (3.21), versus reduced density which is obtained from Eqs. (3.20, 3.21). The highest $\frac{T}{\varepsilon_f}$ corresponds to the lowest beam energy as well and gives the lowest density, especially for the neutrons case. The top energy scale in the figure is for illustration purposes only and it refers to the neutron case. In fact at the same beam energy, p and pn might measure a different $\frac{T}{\varepsilon_f}$ ratio respect to n. This result might be surprising at first, but it simply tells us that at the lowest energies nucleons from the surface of the colliding nuclei come into contact. Those nucleons are located in a low density region, especially neutrons which do not feel the Coulomb field. Thus this is the average density explored by the participant nucleons. In general it is quite different from the maximum density reached during the collisions for which other particles, such as energetic photons, are more suitable probes [8, 78]. With increasing beam energy, the overlapping region increases and more and more fermions are emitted. At about $E_{lab}/A \approx 20$ MeV/A a large number of nucleons are excited and the emission from surface becomes a volume emission. This explains the minimum in the plot, which is due to the increase of T and ε_f when deeper regions of the nuclei are affected. Fragmentation starts around the beam energy which gives the minimum in the plot, where we observe a power law in the mass distribution as well. The lowest density (as well as T) is explored by the neutrons only. Notice that at high densities the pn results are even a factor of two higher than p or n cases. Such a feature is not clear but we will see a more regular behavior of those quantities below. It is important to stress that the ratio plotted in Fig. 3.3 is always smaller than one which confirms the approximations used in Eqs. (3.20, 3.21, 3.24, 3.25).

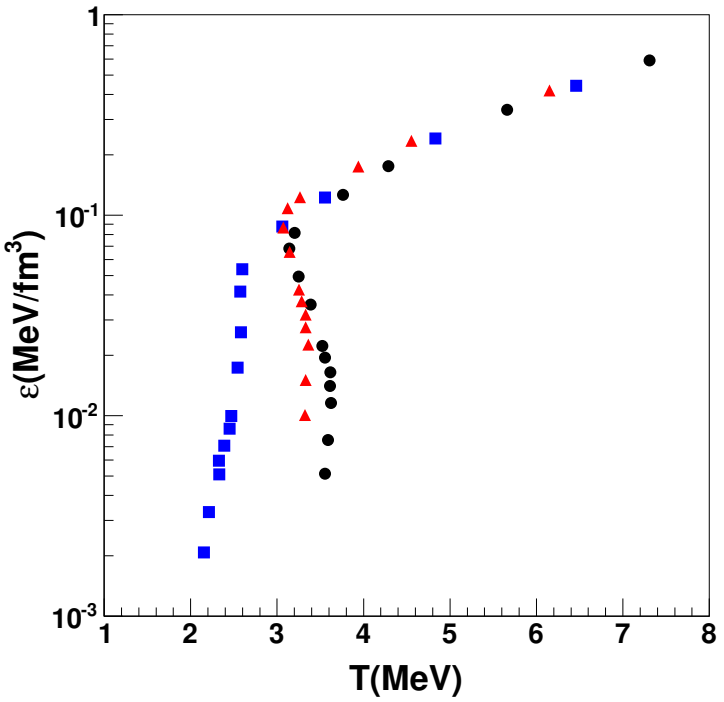

Figure 3.4: Energy density versus temperature. Symbos as in Fig. 3.1.

The best way to visualize the results is by plotting the energy density $\epsilon = \langle \frac{E_{th}}{A} \rangle \rho$ versus temperature as in Fig. 3.4. Now different particle types scale especially at high T where Coulomb effects are expected to be small. A rapid variation of the energy density is observed around $T \approx 2$ MeV for neutrons and $T \approx 3$ MeV for the other cases which indicates a first order phase transition [297]. Notice that a 'plateau' in the caloric curve, i.e. $\langle \frac{E_{th}}{A} \rangle$ versus T [181, 298] has been experimentally observed around 6 MeV. Such a value agrees with our classical approximation plotted in Fig. 3.1, but differs greatly with the quantum results, Fig. 3.4. The critical temperature derived taking into account quantum features differs of almost of a factor two from temperature data obtained using classical approximations. Thus collisions of nuclei at various bombarding energies offer the possibility to explore a

phase transition sensitive to quantum effects and to study the similarities with other quantum systems such as trapped Fermi gases [73, 74, 75]. It is important to stress that our derivation is essentially based on a free Fermi gas approximation, similar to trapped Fermi gases which are weakly interacting. If the interaction becomes important, say at high densities, then the problem of strongly fermionic systems must be addressed properly. For instance the incompressibility at the relevant temperature and density should enter Eq. (3.21). We know from Giant Monopole Resonance studies that the experimental incompressibility can be reasonably reproduced using a Fermi gas approximation [90, 92, 97], thus further validating Eq. (3.21). If this feature is just a 'coincidence' must be further explored both theoretically and experimentally especially near the phase transition. We also notice that Coulomb effects become negligible at around $T = 3$ MeV where the phase transition occurs. The smaller role of the Coulomb field in the phase transition has recently been discussed experimentally in the framework of the Landau's description of phase transitions [176, 299, 300].

4. THE NUMERICAL CALCULATION OF DENSITY AND TEMPERATURE OF FERMIONS FROM QUANTUM FLUCTUATIONS*

In the last chapter, we have discussed the quantum thermometer for fermions at low temperature approximation. The densities and temperatures for p and n from CoMD simulations at different beam energies were also shown. In this chapter, we are going to outline the numerical calculation of densities and temperatures of p and n within the quantum approach with data from CoMD simulations. We also compare the results with the ones from low temperature approximation to test the validity of the low temperature approximation in Fermi systems.

4.1 Formulas of Numerical Calculation for Quantum Fluctuations

As we have shown in the last chapter, we need to study two observables, quadrupole momentum fluctuation and multiplicity fluctuation, based on event by event analysis. In this chapter, we will concentrate on fermions only similar to the last chapter and in particular p and n which are abundantly produced in the heavy-ion collisions thus carrying important information on the densities and temperatures reached. Using the Fermi-Dirac distribution $f(p)$ instead of the Maxwell-Boltzmann distribution in Eq. (3.16), we obtain

$$\begin{aligned} \langle Q_{xy}^2 \rangle &= (2mT)^2 \frac{4}{15} \frac{\int_0^\infty dy \frac{y^{\frac{5}{2}}}{e^{y-\nu}+1}}{\int_0^\infty dy \frac{y^{\frac{1}{2}}}{e^{y-\nu}+1}} \\ &= (2mT)^2 F_{QC}(\nu), \end{aligned} \tag{4.1}$$

*Part of this chapter is reprinted with permission from "Higher order corrections to density and temperature of fermions from quantum fluctuations" by Hua Zheng, Aldo Bonasera, 2012. Physical Review C 86, 027602, Copyright 2012 by American Physical Society and part of this chapter is reprinted with permission from "The many facets of the (non-relativistic) Nuclear Equation of State" by G. Giuliani, H. Zheng, A. Bonasera, 2014. Progress in Particle and Nuclear Physics 76, 116-164, Copyright 2014 by Elsevier B.V.

where $\nu = \frac{\mu}{T}$ and μ is the chemical potential. The detailed derivation of this equation is given in appendix C. $F_{QC}(\nu) = \frac{4}{15}\frac{\int_0^\infty dy \frac{y^{\frac{5}{2}}}{e^{y-\nu}+1}}{\int_0^\infty dy \frac{y^{\frac{1}{2}}}{e^{y-\nu}+1}}$ is the quantum correction factor which should converge to one for high T (classical limit).

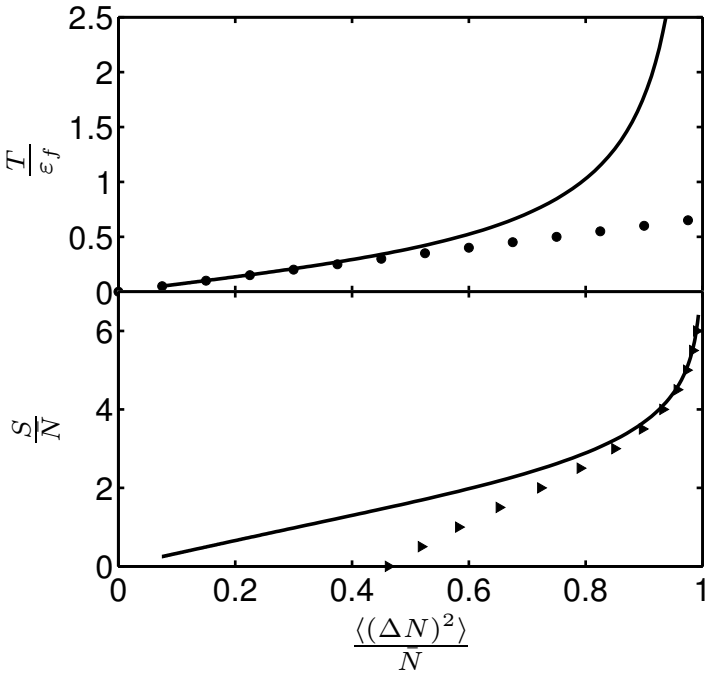

Figure 4.1: (Top) $\frac{T}{\varepsilon_f}$ versus multiplicity fluctuations using different approximations. Full line gives the numerical solution of Eqs. (4.2, 4.3), full dots are the first order approximation discussed in Eq. (3.21); (Bottom) entropy per particle $\frac{S}{N}$ (in units of $\hbar$) versus multiplicity fluctuations. Full line gives the numerical solution of Eq. (4.6), full triangles are the Sackur-Tetrod results.

Within the same framework we can calculate the fluctuations of the p, n multi-

plicity distributions. These are also given in appendix C

$$\frac{\langle(\Delta N)^2\rangle}{\bar{N}} = \frac{\int_0^\infty dy \frac{y^{\frac{1}{2}} e^{y-\nu}}{(e^{y-\nu}+1)^2}}{\int_0^\infty dy \frac{y^{\frac{1}{2}}}{e^{y-\nu}+1}}. \tag{4.2}$$

From the above Eq. (4.2) we can calculate numerically the multiplicity fluctuations for a given ν and recover the value of $\frac{T}{\varepsilon_f}$ from the following equation which is solved numerically:

$$\frac{T}{\varepsilon_f} = \frac{1}{\left[\frac{3}{2}\int_0^\infty dy \frac{y^{\frac{1}{2}}}{e^{y-\nu}+1}\right]^{\frac{2}{3}}}. \tag{4.3}$$

The detailed derivation of this equation is given in appendix C. In Fig. 4.1 we plot the quantity $\frac{T}{\varepsilon_f}$ vs the normalized multiplicity fluctuations obtained by solving numerically Eqs. (4.2, 4.3) while the lowest order approximation, Eq. (3.21), is given by the full dots.

Since in experiments or models one recovers the normalized multiplicity fluctuations, it is better to find a relation between the normalized temperatures as function of the normalized multiplicity fluctuations displayed in the Fig. 4.1. It is useful to parametrize the numerical results as:

$$\frac{T}{\varepsilon_f} = -0.442 + \frac{0.442}{(1-\frac{\langle(\Delta N)^2\rangle}{N})^{0.656}} + 0.345\frac{\langle(\Delta N)^2\rangle}{N} - 0.12(\frac{\langle(\Delta N)^2\rangle}{N})^2, \tag{4.4}$$

which is practically indistinguishable from the numerical result (full line) reported in Fig. 4.1. As expected the approximations contained in Eq. (3.21) reproduce the numerical results (full line) up to $\frac{T}{\varepsilon_f} \approx 0.5$. As we see from the figure the classical limit is recovered for high T using the numerical solution, while the approximations deviate substantially from such a limit. Since from experimental data or models it is possible to extract directly the normalized multiplicity fluctuations, one can easily

derive the value of $\frac{T}{\varepsilon_f}$ from Eq. (4.4).

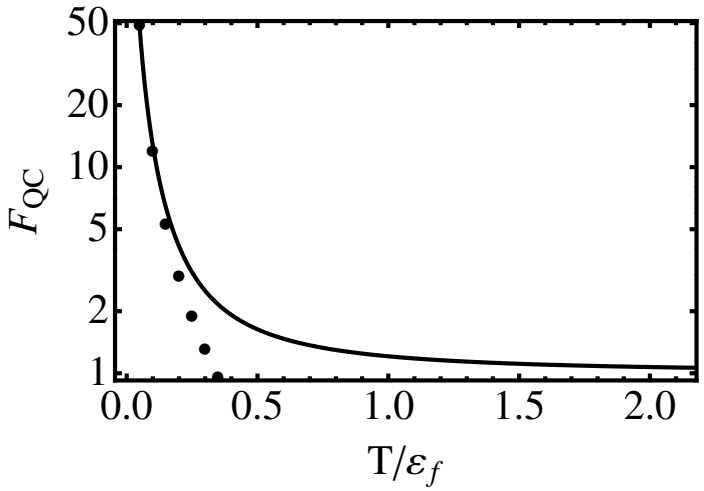

Figure 4.2: F_{QC} versus $\frac{T}{\varepsilon_f}$. Symbols as top panel in Fig. 4.1.

Before proceeding further, it is important to test the validity of the approximations for the quadrupole momentum fluctuations by comparing them to the numerical result solving Eq. (4.1). In Fig. 4.2 we plot the quantum correction term F_{QC} versus $\frac{T}{\varepsilon_f}$. The difference with the classical case is again striking (the F_{QC} in Eq. (4.1) equal to one for a classical perfect gas). For simplicity we can parametrize the numerical result with the simple approximation:

$$F_{QC}|_{fit} = 0.2(\frac{T}{\varepsilon_f})^{-1.71} + 1, \tag{4.5}$$

which is indistinguishable from the numerical result displayed in Fig. 4.2 (full line). Clearly such an equation converges to one at high T as expected. Eqs. (4.4, 4.5) might be very useful when deriving densities and temperatures from experimental

data or models, without worrying if one is in the classical or fully quantum limit, the only constraint is that we are dealing with fermions.

Once the density and the temperature of the system have been determined it is straightforward to derive other thermodynamical quantities. One of such quantities is the entropy:

$$S \equiv \frac{U-A}{T} = \bar{N}\left[\frac{5}{2}\frac{f_{5/2}(z)}{f_{3/2}(z)} - \ln z\right], \tag{4.6}$$

where $f_m(z) = \frac{1}{\Gamma(m)}\int_0^\infty \frac{x^{m-1}dx}{z^{-1}e^x+1}$ and $z = e^{\frac{\mu}{T}}$ is the fugacity. U and A are the internal and Helmotz free energy respectively [1, 7, 51]. This equation can be numerically evaluated and the results are plotted in Fig. 4.1 (bottom panel). For practical purposes it might be useful to have a parametrization of the entropy in terms of the normalized multiplicity fluctuations, which is physically transparent since entropy and fluctuations are strongly correlated [1, 7, 51]:

$$\frac{S}{\bar{N}}|_{fit} = -41.68 + \frac{41.68}{(1-\frac{\langle(\Delta N)^2\rangle}{\bar{N}})^{0.022}} + 2.37\frac{\langle(\Delta N)^2\rangle}{\bar{N}} - 0.83(\frac{\langle(\Delta N)^2\rangle}{\bar{N}})^2. \tag{4.7}$$

The latter fit is indistinguishable from the numerical result plotted in Fig. 4.1 (full line) together with the Sackur-Tetrod result valid in the classical limit [1, 7, 51] as confirmed in the figure.

4.2 Results of Numerical Calculation for Quantum Fluctuations

We apply Eqs. (4.1, 4.4, 4.5) to the CoMD simulation data and redo the analysis. We can obtain the normalized multiplicity fluctuation $\frac{\langle(\Delta N)^2\rangle}{\bar{N}}$ in an event by event analysis. Substituting $\frac{\langle(\Delta N)^2\rangle}{\bar{N}}$ into Eq. (4.4), we can calculate $\frac{T}{\varepsilon_f}$. Then we obtain the quantum correction factor F_{QC} from Eq. (4.5). Later we can derive the quantum temperature T from Eq. (4.1) and ε_f from $\frac{T}{\varepsilon_f}$. Similar to the low temperature case in the last chapter, we can calculate the density through ε_f.

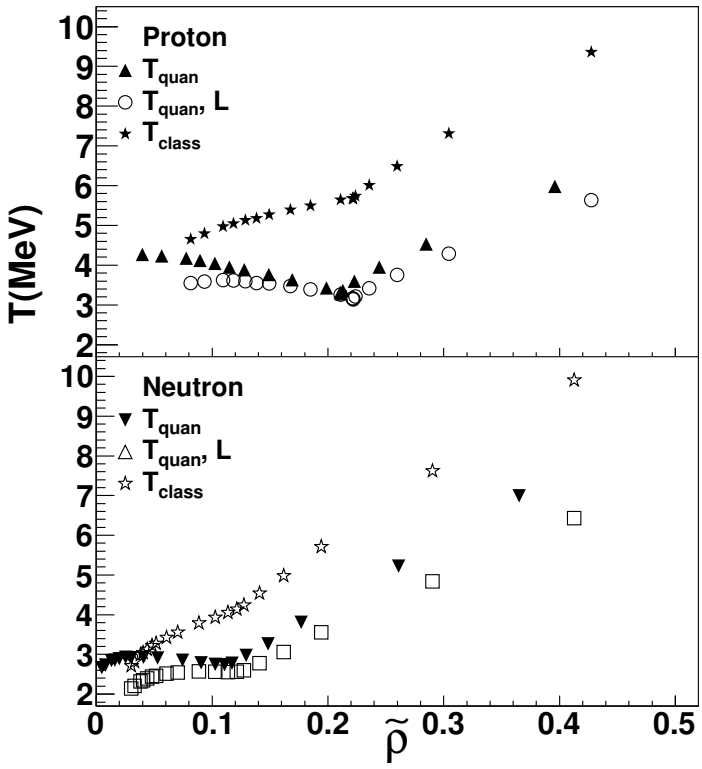

Figure 4.3: Temperature versus density normalized to the ground state density $\rho_0 = 0.165$ fm^{-3}, derived from quantum fluctuations, Eqs. (4.1, 4.4, 4.5). Open dots and open squares are the approximation at the lowest order in $\frac{T}{\varepsilon_f}$, full stars and open stars are the classical cases similar to those in [258], the full triangles are the numerical results.

In Fig. 4.3 we plot the temperature vs density as obtained from the quadrupole momentum and multiplicity fluctuations. The top panel refers to protons while the bottom to neutrons. As we can see from the figure, the results obtained using the fit functions, Eqs. (4.4, 4.5), deviate slightly from the lowest order approximations given in Eqs. (3.20, 3.21). This is a signature that we are in the fully quantum regime for the events considered. For comparison, in the same plot we display the

classical temperatures which are systematically higher than the quantum one, see Eq. (4.1) and Fig. 4.2 [296]. We have to stress that for a given excitation energy we can derive a classical or a quantum temperature, but the density can be derived for the quantum case only within our approach. Of course other methods could be devised that give both classical temperatures and densities using suitable fragment ratios [260]. Those classical temperatures do not need to coincide with the classical temperatures considered here since we are dealing with protons and neutrons only. Larger fragments could be also included and a discussion on this can be found in [181, 258, 295]. A recent experimental data analysis following our approach and compared to other methods confirms our findings [301].

To better summarize the results, we plot in Fig. 4.4 the excitation energy per nucleon $\frac{E^*}{A}$, energy density $\varepsilon = \frac{E^*}{A}\rho$ and the entropy density $\Sigma = \frac{S}{N}\rho$ versus temperature. The so-called caloric curve is well studied in the literature [181, 298] and it shows a well-defined mass dependence [181]. In Fig. 4.4 (top panel), we report the experimental data (open symbols) from ref. [181], obtained in the mass region A=60-100, which is the closest to our system. Recall that the experimental values of the temperature were obtained using classical approximations [181, 298], thus it is no surprise that they agree well with our classical results (full stars). The classical calculations clearly show a region of constant temperature (less than 6 MeV) which would indicate a phase transition. However, notice that the density is changing with changing temperature, Fig. 4.3. For this reason one might wonder on the physical meaning of the caloric curve, and it could be better to investigate the energy density (middle panel). A rapid variation of the energy density is observed around $T \approx 2$ MeV for neutrons and $T \approx 3$ MeV for protons which indicates a first order phase transition [297]. As we see from the figure, the numerical solution of the Fermi integrals gives small corrections while keeping the relevant features obtained in the

lowest approximation intact. This again suggests that in the simulations the system is fully quantal. We also notice that Coulomb effects become negligible at $T >> 3$ MeV where the phase transition occurs. The smaller role of the Coulomb field in the phase transition has recently been discussed experimentally in the framework of the Landau's description of phase transitions [176, 299, 300].

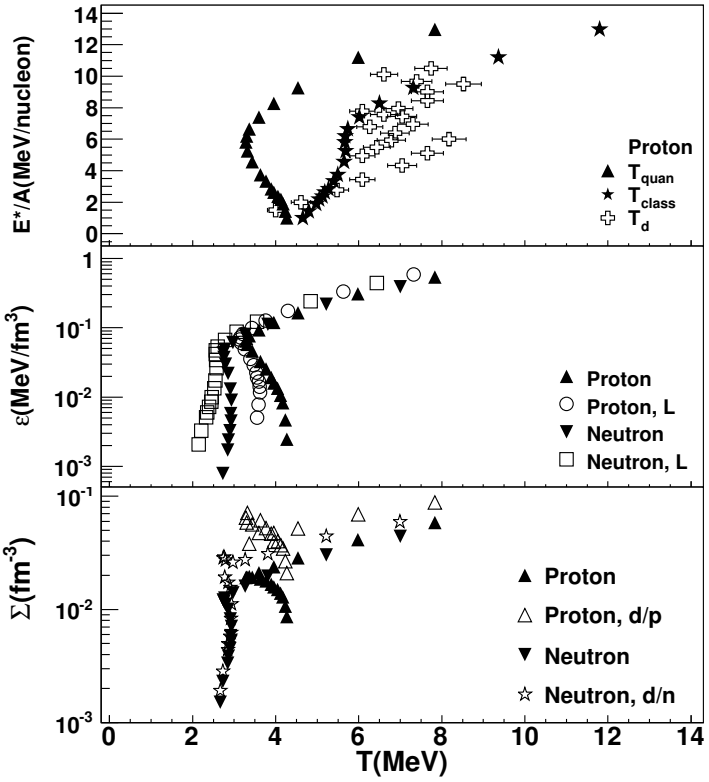

Figure 4.4: (Top) Excitation energy vs temperature, the open symbols refer to experimental data from ref. [181] obtained for mass number A=60-100. (Middle) Energy density vs temperature. (Bottom) Entropy density vs temperature. The opens symbols refer to the entropy density calculated from the ratios of the produced number of deuterons to protons (neutrons), Eq. (4.8). Other symbols as in Fig. 4.3.

In order to confirm the origin of the phase transition, it is useful to derive the entropy density $\Sigma = \frac{S}{\bar{N}}\rho$ which is plotted in the bottom panel of Fig. 4.4. The rapid increase of the entropy per unit volume is due to the sudden increase of the number of degrees of freedom (fragments) with increasing T. The entropy can be also derived from the ratio of the number of deuterons to protons (or neutrons) $R_{d,p(n)}$ [91, 304]:

$$\frac{S}{\bar{N}}|_{d/p(n)} \quad = \quad 3.95 - lnR_{d/p(n)}. \tag{4.8}$$

The CoMD results from Eq. (4.8) multiplied by the density, are plotted in Fig. 4.4 (bottom panel) with open symbols. We find an overall good agreement of the entropy density to the quantum results, Eq. (4.6), especially for neutrons. Very interesting is the good agreement at low T where the particles are emitted from the surface of the nuclei which is at low density. Such a feature is not present for the protons due to large Coulomb distortions. There is a region near the transition ($T \approx 3$ MeV), where both ratios do not reproduce well the quantum results. However, at large temperatures it seems that all methods converge as expected.

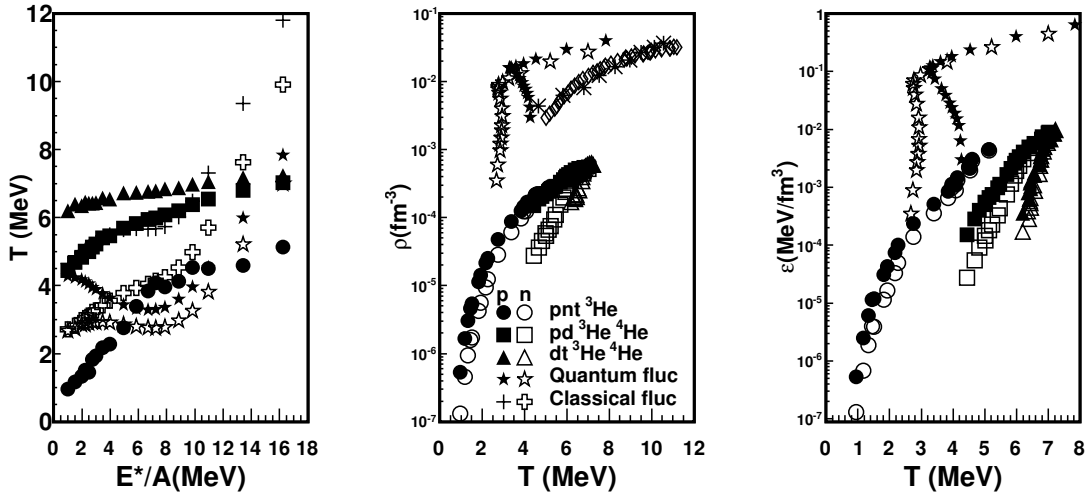

Figure 4.5: (Left panel) the temperatures from different thermometers versus excitation energy per nucleon; (Middle panel) densities versus temperatures, the asterisks [171] and the diamonds refer to experimental results [266, 267, 274]; (Right panel) energy densities versus temperatures. The calculations are performed with CoMD for $^{40}Ca +^{40} Ca$ collisions.

It is interesting to compare the temperature and density results extracted from different thermometers and methods discussed in the last chapter. In Fig. 4.5 some results are reported from CoMD calculations and experiments [171, 266, 267, 274, 283, 284]. We plot the T versus E^*/A (left panel), $\rho_{p,n}$ (middle panel) and energy density $\varepsilon_{n,p}$ (right panel) versus T for different particle double ratios: (1) pnt^3He, (2) pd^3He^4He, (3) dt^3He^4He. The three cases give quite different temperatures when plotted versus the excitation energy. However, when density and energy density are plotted versus T, it seems almost as one case is the continuation of another. The collapse onto a curve is not perfect, which could be the consequence of model calculations stopped at 1000 fm/c. However, in all cases the neutron densities are

much smaller than the proton ones at the same T, similarly for energy densities. This is clearly a Coulomb effect which results on the proton densities being larger than the neutron ones. In the figure we have plotted results from the model and experiments using different methods. The striking feature to be noticed is that the different methods gives similar ranges of T while the densities differ some order of magnitude. This is a feature similar to the one discussed for the NEOS in the classical limit. Some quantities are reasonable while others differ from the exact calculations depending how close we are to the classical limit. As we stressed before, the classical limit is never recovered in the NEOS studies and the same effect can be observed in the density results. The densities obtained from quantum thermometer are much higher than the classical thermal model, but they are very close to the coalescence approach, which can be explained from the fact that the P_0 derived from the data contains many-body effects such as Pauli blocking which is an essential ingredient of the fluctuations approach.

It is instructive to study the 'time evolution' of the temperature using the different methods discussed. In Fig. 4.6 the temperature time evolution is displayed starting from 400 fm/c, a time when fragments are reasonably recognized in coordinate space. The fluctuation method has been applied for p (without Coulomb corrections) and n. In the quantum case we notice that the temperature is saturating around 800 fm/c and the difference with earlier times is however small. It is interesting to notice a change in the time behavior of T for protons. For low excitation energies the temperature increases with time until saturation, the opposite occurs at high excitation energies. The neutron temperature is saturated already at earlier times for the smallest excitation energies. Furthermore, for the classical case, this is true for n and all excitation energies, while for p, it takes sometime until saturation is reached at small excitation energies. This is an effect of the Coulomb potential which distorts the

fluctuations slightly. A similar behavior is observed when calculating T from double ratios, even though the actual values of T are different for each cases. The model seem to indicate an early saturation of the temperature similar to ref. [79]. Probably, the time variation observed in Fig. 4.6 are comparable with the experimental error bars using the different methods [171, 181, 258, 267, 268, 274, 298, 301, 302, 303].

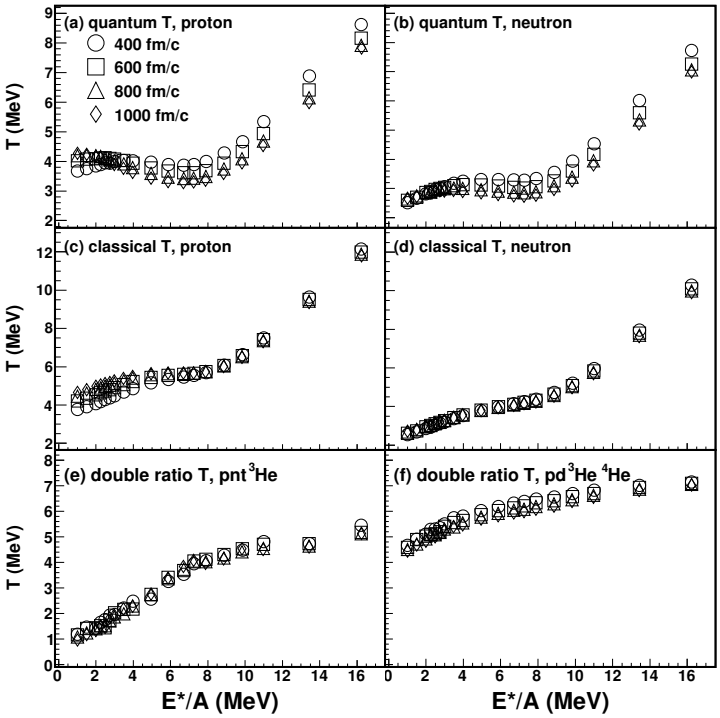

Figure 4.6: Temperature time evolution for different thermometers from CoMD calculations.

5. COULOMB CORRECTIONS TO THE EXTRACTION OF THE DENSITY AND TEMPERATURE FOR FERMIONS FROM QUANTUM FLUCTUATIONS*

In the last chapter, we have discussed the quantum thermometer for fermions using numerical calculation. For convenience, the parametrization equations for the quantum thermometer for fermions are given. The results of densities and temperatures of p and n from CoMD simulation at different beam energies are compared using the low temperature approximation and the numerical calculation which gives the exact result. We have shown the differences between p and n even within the numerical calculation. To explore this problem even more, we have to deal with some effects that might distort the results, the first one is Coulomb. In this chapter, we will consider the Coulomb correction to extract the density and temperature for fermions.

5.1 Coulomb Correction to Temperature and Density

In the microscopic system formed in heavy-ion collisions, non-equilibrium effects could be dominant. As a consequence, the derivation of quantities needed to constrain the NEOS like density, pressure and temperature is not an easy task. To determine densities and temperatures of colliding systems we have recently suggested a method based on fluctuations of quantities such as the light particles multiplicity and quadrupole momentum [147, 258, 283, 284, 286]. We expect fluctuations to give the closest possible determination of the "temperature" of the system, even though

*Reprinted with permission from "Coulomb corrections to the extraction of the density and temperature in non-relativistic heavy ion collisions" by Hua Zheng, Gianluca Giuliani and Aldo Bonasera, 2014. J. Phys. G: Nucl. Part. Phys. 41, 055109, Copyright 2014 by IOP Publishing Ltd.

it could be chaotic but non-ergodic. In the classical limit [258], Quadrupole momentum Fluctuations (QF) can be easily connected to the temperature. Of course, if the system is classical and ergodic, the temperature determined from QF and, say from the slope of the kinetic distribution of the particles should be the same. In the ergodic case, the temperature determined from isotopic double ratios [260] should also give the same result. This is, however, not always observed, which implies that the system is non-ergodic, or non-classical. In [258] the classical temperature derived from QF gave different values for different isotopes. Clearly the Coulomb repulsion of different charged particles can distort the value of the temperature obtained from QF, which depends on kinetic values. On the other hand, MF for different particles seem to be independent on Coulomb effects as we will discuss below [283]. Also the obtained values, say of the critical temperature and density, might be influenced by Coulomb as well as by finite size effects [183, 281, 305, 306, 307, 308, 309]. For these reasons, it is highly needed to correct for these effects as best as possible.

The ideal would be to measure neutron distributions and multiplicities as function of the excitation energy, mass and charge of the source, which is complicated from an experimental point of view, but maybe not impossible. A comparison of p and n will point to Coulomb corrections. The dynamics of the nucleons inside the nuclei are of course affected by Coulomb and there is nothing we can do about it. But a charged particle which leaves an excited system will experience a Coulomb acceleration. Thus we expect that the quadrupole momentum fluctuations will be distorted by Coulomb, since a quadrupole distribution which changes in time, or in different events, will result to different accelerations to the charged fragments which leave the surface of the system.

In this chapter, we proposed a method to correct for Coulomb effects in the exit channels related to the emitted charged fermions. In order to support our findings, we

will compare our results to the neutron case, which is of course independent, at least not directly, from the Coulomb force. Of course, neutron distributions and fluctuations are not easily determined experimentally, thus we will base our considerations on theoretical simulations using the CoMD model again.

Let us imagine that we have a charged particle, say a proton with charge Z_p, leaving a system of charge Z_s, mass A in a volume V. The particle momentum is $\mathbf{p_i}$, and it gets accelerated by the Coulomb field to the final momentum $\mathbf{p_f}$. Assuming a free wave function for the particle, the Coulomb field becomes:

$$\begin{aligned} V(q) &= \langle \psi_f | H_{int} | \psi_i \rangle \\ &= \frac{Z_p e}{V} \int e^{-i\mathbf{p_f}\cdot\mathbf{x}/\hbar} \phi(\mathbf{x}) e^{i\mathbf{p_i}\cdot\mathbf{x}/\hbar} d^3x \\ &= \frac{Z_p e}{V} \int \phi(\mathbf{x}) e^{i\mathbf{q}\cdot\mathbf{x}/\hbar} d^3x \\ &= \frac{4\pi\alpha\hbar^3 Z_p Z_s}{|\mathbf{q}|^2 V} \int f(\mathbf{x}) e^{i\mathbf{q}\cdot\mathbf{x}/\hbar} d^3x \\ &= \frac{1.44 \times 4\pi\hbar^2 Z_p Z_s}{q^2 V} \int f(\mathbf{x}) e^{i\mathbf{q}\cdot\mathbf{x}/\hbar} d^3x \\ &= \frac{1.44 \times 4\pi\hbar^2 Z_p Z_s}{q^2 V} F(\mathbf{q}), \end{aligned} \tag{5.1}$$

where $\mathbf{q} = \mathbf{p_i} - \mathbf{p_f}$, $\phi(\mathbf{x})$ is the Coulomb potential of the source, $f(\mathbf{x})$ is the normalized charged density distribution of the source, $F(\mathbf{q})$ is the form factor [5]. This is similar to the density determination of the source for instance in electron-nucleus scattering. To make calculations feasible, we will assume that $\mathbf{p_i}$ is negligible, which is not a bad approximation at low energies or temperatures since most of the charged particle acceleration is due to Coulomb. At high excitation energies we expect Coulomb to be negligible [175, 176] since the source is at low density. In fact we have seen in previous calculations [283, 284, 286] that charged and uncharged particles produced in the collisions at high energies give similar values of T as expected.

For simplicity we will also assume that the form factor is equal to 1. A different form factor is feasible but it needs the introduction of another parameter, which is connected to the density of the source. We have tried using a Gaussian density distribution of the source, but the extra parameter calls for other conditions to be implemented and to very high statistics. We are presently studying such cases.

The reason for essentially making a Fourier transform of the Coulomb field, is because the distribution function is modified by the factor [1]:

$$f(p) \propto \exp[-\frac{R_{min}}{T}] \propto \exp[-\frac{V(q=p)}{T}]. \tag{5.2}$$

Using this result, we can estimate modifications to physical quantities in the classical and quantum cases. The classical case is interesting because, as we will show, gives smaller temperatures for different fragments, very close to the neutron case. Furthermore, since we have an extra parameter, the volume V, entering Eq. (5.1), we need a further condition in order to determine both quantities, V and T. Multiplicity fluctuations are equal to one in the classical case and the Coulomb correction does not change such a result significantly as we will show in the following. Thus the Coulomb correction is more important for kinetic quantities, quadrupole momentum fluctuations, kinetic energy distributions, etc, and not for multiplicity fluctuations or yields. This remains true in the quantum case, where we will see that the temperatures say of protons are very close to those of neutrons after the Coulomb correction while their densities are practically independent on it. We stress that, in the quantum case, the density is mainly determined by the MF. In the next sections we will discuss the classical and quantum cases separately.

5.2 Classical Case

The quadrupole momentum fluctuations including the Coulomb corrections are given by:

$$\langle Q_{xy}^2 \rangle = \frac{\int d^3p (p_x^2 - p_y^2)^2 e^{-(\frac{p^2}{2mT} + \frac{1.44 \times 4\pi\hbar^2 Z_p Z_s}{p^2 VT})}}{\int d^3p e^{-(\frac{p^2}{2mT} + \frac{1.44 \times 4\pi\hbar^2 Z_p Z_s}{p^2 VT})}}, \tag{5.3}$$

where Z_i are the charges of the source and accelerated ion. After some algebra reported in appendix D we get

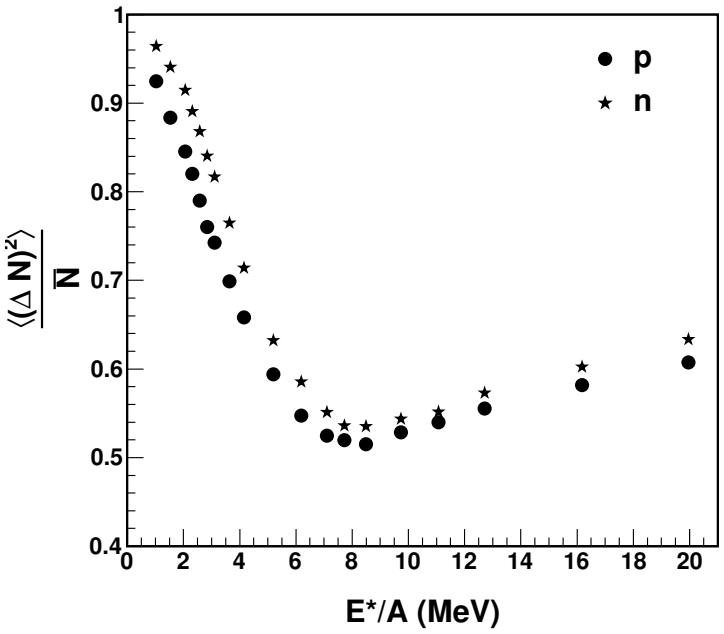

Figure 5.1: The multiplicity fluctuation for p and n, from CoMD calculations, versus excitation energy per nucleon E*/A. The minimum seen in the figure might be due to transparency effects in the model [283, 284].

$$\langle Q_{xy}^2 \rangle = \frac{1}{a^2}[1 + \frac{\frac{8}{5}ab + \frac{8}{15}(ab)^{3/2}}{1 + 2(ab)^{1/2}}], \tag{5.4}$$

where

$$a = \frac{1}{2mT}, \quad b = \frac{1.44 \times 4\pi\hbar^2 Z_p Z_s}{VT}. \tag{5.5}$$

The first term in Eq. (5.4) agrees with the classical result obtained in [258], ignoring Coulomb effects, and the correction depends on the charge, volume and mass of the emitted particle and source. Within the same spirit we can calculate the multiplicity fluctuations, which we report in appendix D. In Fig. 5.1, we plot the multiplicity fluctuations for p and n vs excitation energy per nucleon, respectively. Especially, the neutron multiplicity fluctuations are always less than 1 which cannot be explained by Eq. (D.21). Those multiplicity fluctuations might be due to fermion quenching, and we will discuss the quantum case in next section.

In Fig. 5.2 we show the differences, as function of the excitation energy per nucleon, between the multiplicity fluctuations of protons and neutrons and mirror nuclei as ^3H and ^3He:

$$\Delta\frac{\langle(\Delta N)^2\rangle}{\bar{N}} = \frac{\langle(\Delta N_a)^2\rangle}{\bar{N}_a} - \frac{\langle(\Delta N_b)^2\rangle}{\bar{N}_b}, \tag{5.6}$$

where a and b refer to p or ^3H and n or ^3He respectively. The derived multiplicity fluctuation differences from Eq. (D.21) are not able to reproduce the results obtained in CoMD for p, n, ^3H and ^3He. In particular, Fig. 5.2 shows small differences for the ^3H and ^3He nuclei, suggesting that Coulomb is not responsible for their multiplicity fluctuations quenching. In the same figure we display the difference of MF of protons and neutrons. Such a difference is quite large, which would suggest a Coulomb effect. However, the difference is especially large at low beam energy when the nucleons are

probably emitted from the touching surfaces of the colliding nuclei. If this is true then the emitted proton or neutron might be differently reabsorbed by one of the nuclei in some sort of shadowing.

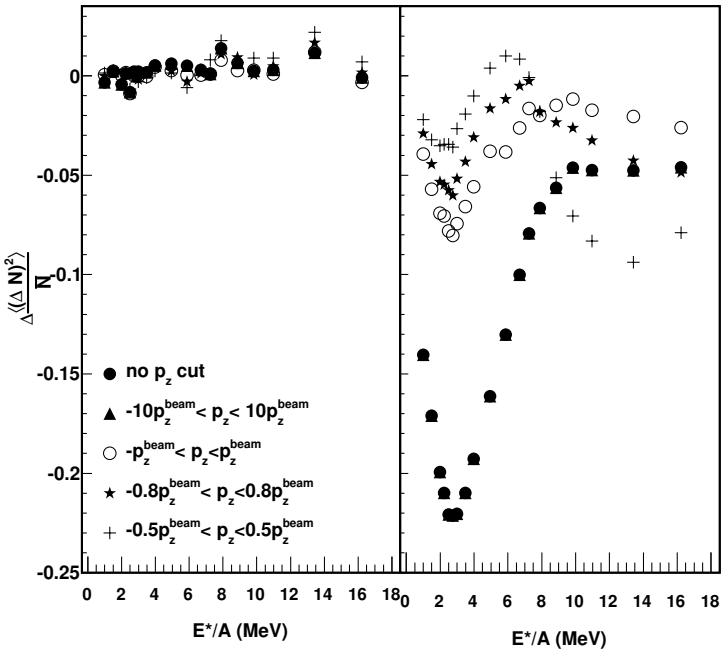

Figure 5.2: The multiplicity fluctuation differences, from CoMD calculations, versus excitation energy per nucleon E*/A for different p_z^{cut} cuts used to select particles with $-p_z^{cut} < p_z < p_z^{cut}$. $p_z^{cut} = x \times p_z^{beam}$ and p_z^{beam} is the initial p_z of the beam at energy $\underline{E/A}$ (MeV) in the center of mass frame. The left panel is for (^3H,^3He) and the right panel is for (p, n).

Thus, if we restrict the multiplicity fluctuations of particles in the direction perpendicular to the beam axis, then their difference should be small. As we see in the figure, this is indeed the case when we calculate the MF for particles emitted

with a small momentum along the beam axis, i.e. particles, which are predominantly emitted perpendicular to the beam. Notice that this strategy agrees with the choice of calculating the QF and the excitation energy [283, 284, 286] in the perpendicular direction. In the following, all results have been obtained using $1p_z^{beam}$ cut, a compromise to include particles going in the perpendicular direction and enough statistics.

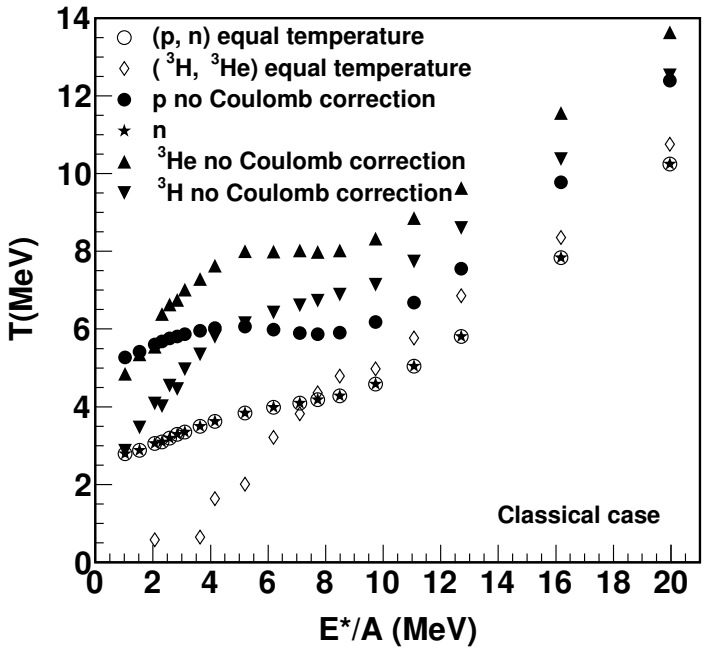

Figure 5.3: The temperatures extracted from CoMD simulated data versus excitation energy per nucleon E*/A for different particles with and without Coulomb corrections. d and α are assumed to have the same T as the neutrons and are not included in the figure for clarity.

Since MF cannot give any further constraints in the classical case, we need a

different strategy in order to solve Eq. (5.4), which depends on T and V. Let us assume that mirror nuclei, for instance ^3H and ^3He, behave similarly the only differences due to the Coulomb shift in the exit channel. If this is true, then T and V are the same for the two particles. Thus we can write down two equations for each case and from these derive the values of T and V. Of course the value of T will be smaller than their respective values obtained without Coulomb correction, when say ^3He, displays a higher temperature than ^3H. This is indeed observed in the experimental data as well [258]. In Fig. 5.3 we plot the T obtained with and without Coulomb corrections for those mirror nuclei as function of the excitation energy per nucleon. As predicted, the Coulomb corrected temperature is smaller than the uncorrected ones. Further, their common value is very close to that obtained from the neutrons. We notice that the discrepancy observed at small excitation energies is not due to the low statistics of those particles, especially ^3He, in the calculations. In fact we have repeated the calculations with half the statistics of events and found very similar results. However, the number of points for ^3H, ^3He displayed in the figure is less than the p, n points, since we could not find any solutions to Eq. (5.4) for some cases. This might suggest that the assumption of equal T for ^3H and ^3He nuclei might not be a good one at small excitation energies, where indeed, the Coulomb barrier is quite different for the two ions. An alternative explanation might be that the density seen by composite fragments is different from that of nucleons, which might result in different temperatures as well.

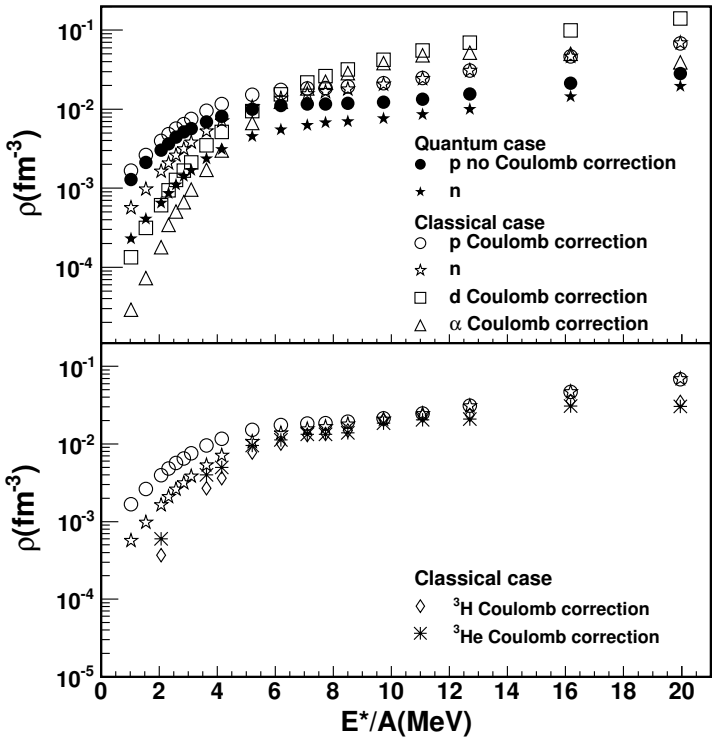

Figure 5.4: Densities extracted from CoMD simulated data versus excitation energy per nucleon E*/A. (Up panel) solid circles, solid stars refer to densities of p, n obtained from quantum fluctuations without Coulomb correction respectively; open circles, open stars, open squares and open triangles refer to densities of p, n, d and α obtained from Eqs. (3.11, 5.4) respectively. Notice that the high density obtained in the d-case is most probably due to the fact that they are overbound in the CoMD model. Experimental results display a different ordering [274] because of the different binding energies in the model. (Bottom panel) the results for the fermions in the classical limit, obtained from Eqs. (3.11, 5.4). Open circles, open stars are the same results showed in the up panel for p and n. Open diamonds and asterisks refer to ^3H and ^3He respectively.

Adopting such a strategy we can derive the T for other mirror nuclei such as p and n. Trivially the new T will coincide with the neutron one. However, in experimental data where the neutron's T is not measured, one could assume that T is given by the ^3H, ^3He mirror nuclei and from the proton QF one could derive the V which does not need to be the same as that of the other mirror nuclei [266]. The same strategy can be adopted to determine the V seen by d and α particles. All these cases are displayed in Fig. 5.3.

In cases where high statistics is available, for instance in experiments, one could determine T and V from other mirror nuclei such as ^7Li, ^7Be etc. and confirm if they agree or not with the previously determined ones. Our calculations do not allow us to do so because of the low statistics of those particles. From the volume, we can calculate the density for each particle type using Eq. (3.11). In Fig. 5.4 we plot the density vs excitation energy per nucleon in different cases and we compare to the density obtained from quantum fluctuations [283, 284]. As it has been pointed out in [310], the determination of the density of the system could be influenced by the semi-classical nature of the model approach. A dependence on the particle type is present, similar to experimental observations [274]. We have estimated the density of d and α as well, by assuming that they have the same neutron temperature. Notice that the $(^3H, ^3He)$ densities are smaller than the (p, n) densities for lower excitation energies, which could explain the corresponding lower temperatures discussed above.

We stress that the assumption of equal temperature of different particles is perfectly in the spirit of an ergodic system and it is used, for instance, when calculating T from the double isotope ratio [260]. From Fig. 5.3, the 'near ergodicity' of the system is supported from the T similarity of neutrons with ^3H, ^3He. We will find a similar result in the quantum case.

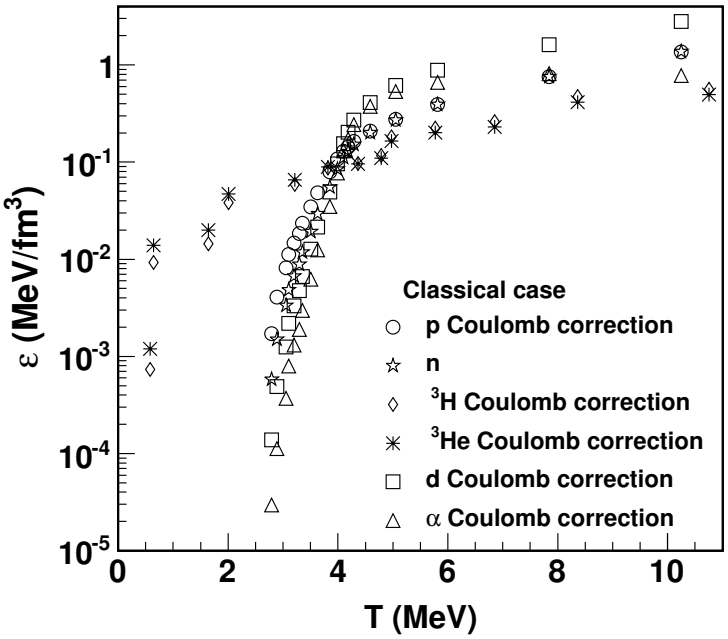

Figure 5.5: Energy densities extracted from CoMD simulated data versus temperature. The results are obtained from the classical case with Coulomb correction.

From the values of density and excitation energy, we can easily obtain the energy density, which is plotted in Fig. 5.5 as function of T. The plot displays the same features reported in [283, 284, 286]. In particular the very rapidly increase at small T is due to the opening of many evaporation channels which terminates around $T = 4$ MeV when fragmentation starts. The fragmentation region terminates around $T =$ 10 MeV for p and n, close to the critical temperature [171]. Quantum corrections, as we will discuss in the next section, gives qualitatively similar results. Notice the discrepancy at low T with the $(^3H, ^3He)$ cases which might be suggestive of the fact that the assumption of equal temperatures is not valid at low excitation energies.

5.3 Quantum Case–Fermions

The above discussion can be generalized to the quantum case. In particular, in this section we will restrict the results to the p and n cases (fermions) and avoid involved discussions on bosons (d and α) or more complex fermions [147, 283, 284]. The QF can be obtained from:

$$\langle Q_{xy}^2 \rangle = (2mT)^2 \frac{4}{15} \frac{\int_0^\infty dy y^{\frac{5}{2}} \frac{1}{e^{y+\frac{A}{yT^2}-\nu}+1}}{\int_0^\infty dy y^{\frac{1}{2}} \frac{1}{e^{y+\frac{A}{yT^2}-\nu}+1}}, \tag{5.7}$$

where $A = \frac{1.44 \times 4\pi\hbar^2 q_1 q_2}{2mV}$ and $\nu = \frac{\mu}{T}$. The terms in Eq. (5.7) are similar to their classical counterpart and a detailed derivation of this result is given in appendix D. On the same ground we can derive the MF as:

$$\frac{\langle (\Delta N)^2 \rangle}{\bar{N}} = \frac{\int_0^\infty dy y^{\frac{1}{2}} \frac{e^{y+\frac{A}{yT^2}-\nu}}{(e^{y+\frac{A}{yT^2}-\nu}+1)^2}}{\int_0^\infty dy y^{\frac{1}{2}} \frac{1}{e^{y+\frac{A}{yT^2}-\nu}+1}}. \tag{5.8}$$

Again the detailed derivation is given in the appendix D. Those equations can be solved numerically. In Fig. 5.6 we plot T and ρ vs excitation energy per nucleon respectively. The protons and neutrons cases only are included. As we see the derived T of protons are much closer to the neutrons, supporting the ansatz we used in the classical case. Notice the backbending in T vs E^*/A without Coulomb correction. This results is similar to what has been discussed by D. Gross [237] and it is purely a Coulomb effect. Also the good agreement for the obtained temperatures suggests that thermal equilibrium in the transverse direction is nearly reached.The modification to the density due to Coulomb is very small which implies that the MF are not so much affected by Coulomb.

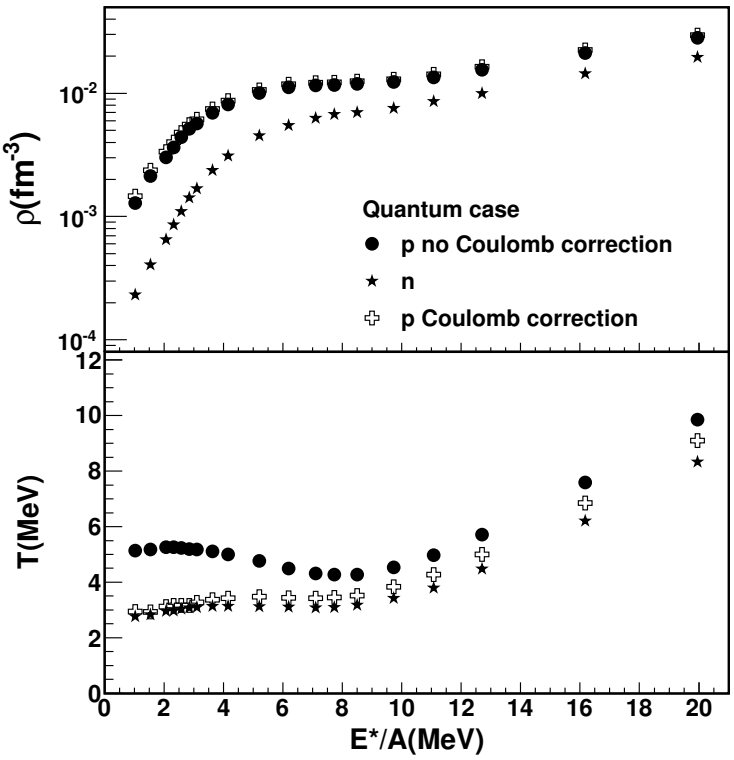

Figure 5.6: (Top panel) Densities extracted from CoMD simulated data versus excitation energy per nucleon E*/A. (Bottom panel) Temperatures versus E*/A. Solid circles and solid stars refer to p and n obtained from quantum fluctuations without Coulomb correction respectively; open crosses refer to p-case obtained from quantum fluctuations with Coulomb correction.

As we see from the results, even though the T are similar for p and n, their densities are not which suggests that p and n 'see' different densities probably already in the ground state of the nuclei. Those differences are less noticeable if we plot the energy density $\varepsilon = \frac{E}{N}\rho$ versus T. This is displayed in Fig. 5.7, which shows a very similar behavior of p and n.

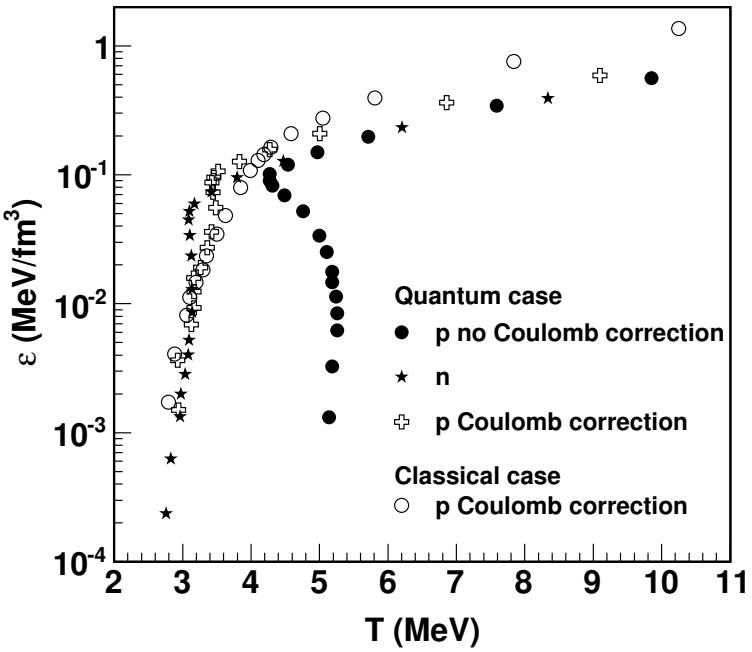

Figure 5.7: Energy density extracted from CoMD simulated data versus temperature. Open circles refer to the classical results with Coulomb correction, other symbols as in Fig. 5.6.

6. DENSITY AND TEMPERATURE OF BOSONS FROM QUANTUM FLUCTUATIONS*

In the previous chapters, we discussed the quantum thermometer for fermions in the low temperature approximation, full calculation with and without Coulomb correction. Now, we will focus on the bosons produced in the heavy-ion collisions. In this chapter, we will show how to extract the temperature and density of bosons within a quantum approach. We analyze the CoMD and CoMD$_\alpha$ which we have discussed in chapter 2 simulation data.

6.1 Quantum Thermometer for Bosons

Fragmentation of heavy ions displays a large production of α particles as compared to nucleons [8, 78, 79]. This poses the question of the role of bosons in nuclear matter and finite nuclei. We know that light nuclei display an α-cluster structure which could be exemplified by the so-called 'Hoyle' state in ^{12}C, i.e. the first excited state of such a nucleus which decays into 3α's [311]. The fact that the ground state of nuclei could be made of α clusters could justify their copious production in heavy-ion collisions near the Fermi energy. At the same time these facts raise the natural question of wheter α clustering and production could be signatures of a Bose-Einstein condensate (BEC) [62, 67, 68].

In this chapter we discuss some properties of finite temperatures assuming either a classical gas or a quantum Bose system. A Fermi system has been discussed in the previous chapters. We base our approach on fluctuations estimated from an event by event determination of fragments originating from the energetic collision.

*Reprinted with permission from "Density and temperature of bosons from quantum fluctuations" by Hua Zheng, Gianluca Giuliani, Aldo Bonasera, 2012. Nuclear Physics A 892, 43-57, Copyright 2012 by Elsevier B.V.

A similar method has recently been applied to observe suppression of fluctuations in a trapped Fermi gas [73, 74, 75] and enhancement of fluctuations in BEC [72]. Recent experimental data on low density clustering in nuclear collisions and a comparison to microscopic quantum statistical models suggested the possibility that in order to reproduce the data, a Bose condensate is needed [63, 274]. In ref. [283], we proposed a method to go beyond refs. [72, 73, 74, 75] by including quadrupole momentum fluctuations as well to have a measurement of densities and temperatures for subatomic systems for which it is difficult to obtain such information in a direct way. We apply our proposal to the results of CoMD calculation [86, 243, 250, 251, 252, 253] which includes Fermi statistics. Because of antisymmetrization, the model gives some clustering into α like structures in the ground state of some nuclei such as ^{40}Ca. Also, in fragmentation reactions, the model predicts large yields of α clusters, but the experimental yield is largely underestimated [86, 243, 250, 251, 252, 253]. However, after including boson correlations in the collision term, their yields are largely increased and closer to data. These features should be kept in mind when discussing a possible BEC in the model. More refined models are possible but experimental data are needed in order to guide the modeling. We believe that such data could be obtained from heavy-ion collisions using 4π detectors and performing a careful event by event analysis. The major serious problem we foresee is in the event selection for which the results discussed here in terms of the CoMD approach could be of guidance. In particular we suggest to select final events in such a way that all fragments have a α like (i.e. ^{12}C, ^{16}O etc.) or d-like structure (^{6}Li, ^{10}B etc.). Preliminary experimental results on $^{40}Ca + ^{40}Ca$ performed at the Cyclotron Institute at Texas A&M university show that those events are indeed found [312].

In heavy-ion collisions, the produced particles do *not* follow classical statistics thus the correct distribution function must be used when we calculate the quadrupole

momentum fluctuation. Bosons d, α etc., should follow the Bose-Einstein statistics. We will concentrate on bosons only, particularly on d and α, which are abundantly produced in the collisions.

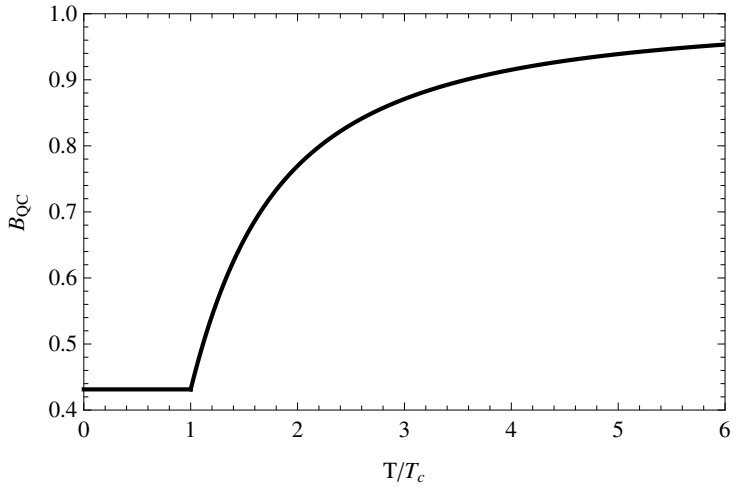

Figure 6.1: The quantum correction factor B_{QC} for bosons versus the reduced temperature $\frac{T}{T_c}$.

Using a Bose-Einstein distribution $f(p)$, Eq. (3.17), for a particle of spin s, and expanding near the critical temperature:

$$T_c = \frac{3.31}{[2s+1]^{2/3}} \frac{\hbar^2}{m} \rho^{2/3}, \tag{6.1}$$

at a given density ρ, we get:

$$\langle Q_{xy}^2 \rangle = (2mT)^2 B_{QC}(1), \quad (T < T_c) \tag{6.2}$$

$$\langle Q_{xy}^2 \rangle = (2mT)^2 B_{QC}(z), \quad (T > T_c) \tag{6.3}$$

where $B_{QC}(z) = \frac{g_{7/2}(z)}{g_{3/2}(z)}$ is the quantum correction factor for bosons, the $g_n(z) = \frac{1}{\Gamma(n)} \int \frac{x^{n-1}}{z^{-1}e^x - 1} dx$ functions are well studied in the literature and $z = e^{\mu/T}$ is the fugacity which depends on the temperature T and the chemical potential μ connecting with T_c [1, 7, 51]. Notice the similarity with the classical result which is modified by the $B_{QC}(z)$ functions only. In Fig. 6.1, we plot $B_{QC}(z)$ as function of $\frac{T}{T_c}$ obtained by solving the relevant Bose integrals numerically. Below the critical temperature $B_{QC}(1) = 0.4313$ and $B_{QC}(z)$ is always less than 1 above the critical temperature, thus the same quadrupole momentum fluctuation implies a higher temperature in a Bose gas than in a classical gas. $B_{QC}(z)$ approaches one for large T and small densities, recovering the classical result. These features are in contrast to the behavior of fermion systems. For which the temperature is always smaller than the classical limit [283, 284, 285], i.e. opposite to the boson case. The quadrupole momentum fluctuations depend on temperature and density through T_c, Eq. (6.1), thus we need more information in order to be able to determine both quantities when $T > T_c$. We stress that Eqs. (6.1, 6.2, 6.3) are derived under the assumption of a non-interacting Bose gas. Interactions will change somehow the results. However, from superfluid ^4He we know that the experimental critical temperature is not much different from the ideal gas result.

Within the same framework we can calculate the fluctuations of boson multiplicity distributions numerically when $T > T_c$. When $T < T_c$ the multiplicity fluctuations are always infinite since the isothermal compressibility diverges for ideal bosons [1, 7, 51]. This phenomenon is of course not observed in experiments [72]. Therefore, we need to include interactions between bosons (and fermions if present) near the critical point. We use the Landau's phase transition theory near the critical point.

In the Landau's theory of phase transition of second kind [1, 7], the thermodynamic potential is expanded in terms of the order parameter near the critical point:

$$\Phi(P,T,\eta) = \Phi_0(P,T) + \frac{1}{2}a\eta^2 + \frac{1}{4}b\eta^4 + \frac{1}{6}c\eta^6 - \eta hV, \tag{6.4}$$

a, b, c are the expansion coefficients and c is positive, η is the order parameter and h is the field "strength" or external field. We have stopped the expansion to sixth order since it gives a reasonable description of the critical exponents. To derive the critical exponents, let $a = a_0 t, a_0 > 0$, where $t = T - T_c$, and $b = 0$, thus

$$\Phi(P,T,\eta) = \Phi_0(P,T) + \frac{1}{2}a_0 t\eta^2 + \frac{1}{6}c\eta^6 - \eta hV, \tag{6.5}$$

To obtain the minimum of $\Phi(P,T,\eta)$, let $\frac{\partial\Phi(P,T,\eta)}{\partial\eta}|_{\eta=\overline{\eta}} = 0$:

$$a_0 t\overline{\eta} + c\overline{\eta}^5 - hV = 0. \tag{6.6}$$

For $h = 0$, the solution is

$$\overline{\eta} = \begin{cases} 0, & (t > 0) \\ \pm(\frac{a_0}{c})^{1/4}|t|^{1/4}, & (t < 0) \end{cases} \tag{6.7}$$

which gives a critical exponent $\beta = 0.25$ to compare to experimental values $\beta = 0.32 - 0.39$ and to the mean field value $\beta = 0.5$ which could be obtained from Landau's theory by stopping the expansion to fourth order [1, 7]. Differentiating Eq. (6.6) respect to h, we get

$$a_0 t\frac{\partial\overline{\eta}}{\partial h} + 5c\overline{\eta}^4\frac{\partial\overline{\eta}}{\partial h} - V = 0. \tag{6.8}$$

Solving Eq. (6.8) for $\frac{\partial\overline{\eta}}{\partial h}$ and substituting Eq. (6.7) into the solution, we obtain

$$\frac{\partial\overline{\eta}}{\partial h} = \frac{V}{a_0 t + 5c\overline{\eta}^4} = \begin{cases} \frac{V}{a_0}|t|^{-1}, & (t > 0) \\ \frac{V}{4a_0}|t|^{-1}, & (t < 0) \end{cases} \tag{6.9}$$

From [1, 7] , we know that the fluctuation of the order parameter is given by:

$$\langle(\Delta\eta)^2\rangle = T_c\chi/V, \tag{6.10}$$

where $\chi = \frac{\partial\eta}{\partial h}\Big|_{P,T;h\to 0} = \frac{\partial\overline{\eta}}{\partial h}$. Substituting Eq. (6.9) into Eq. (6.10), the fluctuation of the order parameter can be expressed as:

$$\begin{aligned} \langle(\Delta\eta)^2\rangle &= \begin{cases} \frac{VT_c}{a_0 V}|t|^{-1}, & (t > 0) \\ \frac{1}{4}\frac{VT_c}{a_0 V}|t|^{-1}, & (t < 0) \end{cases} \\ &= \begin{cases} \frac{1}{a_0}|\tilde{t}|^{-1}, & (\tilde{t} > 0) \\ \frac{1}{4a_0}|\tilde{t}|^{-1}, & (\tilde{t} < 0) \end{cases} \end{aligned} \tag{6.11}$$

where we define $\tilde{t} = \frac{T-T_c}{T_c}$. If one assumes $\langle(\Delta\eta)^2\rangle = \frac{\langle(\Delta N)^2\rangle}{\bar{N}}$, then the normalized multiplicity fluctuation of the system near the critical point is

$$\frac{\langle(\Delta N)^2\rangle}{\bar{N}} = \begin{cases} \frac{1}{a_0}|\tilde{t}|^{-1}, & (\tilde{t} > 0) \\ \frac{1}{4a_0}|\tilde{t}|^{-1}, & (\tilde{t} < 0) \end{cases} \tag{6.12}$$

The last quantity can be obtained both theoretically or experimentally from the multiplicity fluctuations say of d or α bosons. In the discussion above we are assuming that those fluctuations are critically large and use Landau's approach of critical fluctuations. In previous attempts we have used an ideal Bose-gas ansatz which gives infinite compressibility below the critical point [1, 7, 51]. Such an approach is

unphysical as it is well known and the use of Landau's theory permits the possibility of getting the critical fluctuations below the critical point as well, Eq. (6.12).

We can use Eq. (6.12) to fit the numerical result of the multiplicity fluctuations near the critical point when $T > T_c$ and determine the coefficient a_0. In the theory of phase transitions, Eq. (6.12) gives the critical behavior of the order parameter fluctuations. Away from the critical point a smooth function can be added to Eq. (6.12). Noticing that when $T = 0$ the normalized multiplicity fluctuation should be 0 and when $T = \infty$ the normalized multiplicity fluctuation should be 1, we modify Eq. (6.12), valid near the critical point, to fulfill $\frac{\langle(\Delta N)^2\rangle}{\bar{N}} = 0$ at $T = 0$ and $\frac{\langle(\Delta N)^2\rangle}{\bar{N}} = 1$ at $T = \infty$. Then the normalized multiplicity fluctuations are simply:

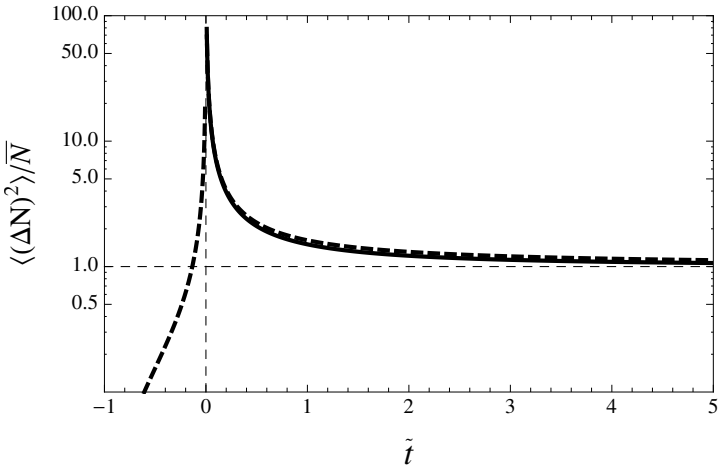

Figure 6.2: Normalized multiplicity fluctuations for bosons versus $\tilde{t}$. The black solid line is the numerical result when $T > T_c$, the thick dashed lines are the results from Landau's phase transition theory Eqs. (6.13, 6.14).

$$\frac{\langle(\Delta N)^2\rangle}{\bar{N}} = 0.155|\tilde{t}|^{-1} - 0.155, \quad (T < T_c) \tag{6.13}$$

$$\frac{\langle(\Delta N)^2\rangle}{\bar{N}} = 0.62|\tilde{t}|^{-1} + 1, \quad (T > T_c) \tag{6.14}$$

We plot the normalized multiplicity fluctuations in Fig. 6.2. It is amazing that, above the critical point, Eq. (6.14) can fit the numerical result so well. The difference with the fermionic case [283, 284, 285] is striking: for bosons, fluctuations are larger than the average value and might diverge near the critical point, Eqs. (6.13, 6.14), in the indicated approximations. Finite size effects might of course smoothen the divergence [1, 7]. These results are very important and could be used to pin down a BEC by comparing fermions and bosons produced in nuclear reactions on an event by event basis [312]. They should be valid for any boson system, for instance for trapped BEC [72].

Two solutions are possible depending whether the system is above or below the critical temperature for a BEC. Below the critical point, Eq. (6.2) can be used to calculate T and then Eq. (6.13) gives the critical temperature T_c and the corresponding density ρ, Eq. (6.1). Above the critical point it is better to estimate $\nu = \frac{\mu}{T}$. For practical purposes, we fit ν as function of normalized multiplicity fluctuation which is given by:

$$\nu = -3.018 \times \exp[-2.8018(\frac{\langle(\Delta N)^2\rangle}{\bar{N}} - 1)^{0.45}] \times (\frac{\langle(\Delta N)^2\rangle}{\bar{N}} - 1)^{0.1142}, \quad (T > T_c) \tag{6.15}$$

From this equation we can estimate the $B_{QC}(z)$ functions entering Eq. (6.3) and obtain the value of T. Also, it might be useful to have a parameterization of $B_{QC}(z)$

functions in terms of the normalized multiplicity fluctuations through ν,

$$B_{QC}(z) = -0.5764 \exp(-1.5963|\nu|^{0.6452}) + 1.0077. \tag{6.16}$$

Using such a value in Eq. (6.3) and Eq. (6.14) gives T_c and the density ρ, Eq. (6.1). In the numerical simulations discussed later we can always use the two solutions and one of them can be rejected from physical considerations. For instance assuming that we are below the critical point, it leads to densities as high as ten times the ground state density which is unphysical for heavy-ion collisions around the Fermi energy. We stress that we expect from the phenomenology of boson-fermion mixtures in a trap, that the boson density is much higher than the corresponding density of the fermions [313, 314, 315, 316, 317, 318].

6.2 The Results of Temperature and Density

In our calculation we stop the calculations at t=1000 fm/c for numerical reasons. We have tested for some cases that the results are quite stable when increasing the calculation time to 3000 fm/c. We need to stress that the binding energies of light clusters are overestimated in the model especially d. Thus the results obtained here for d should be taken as qualitative.

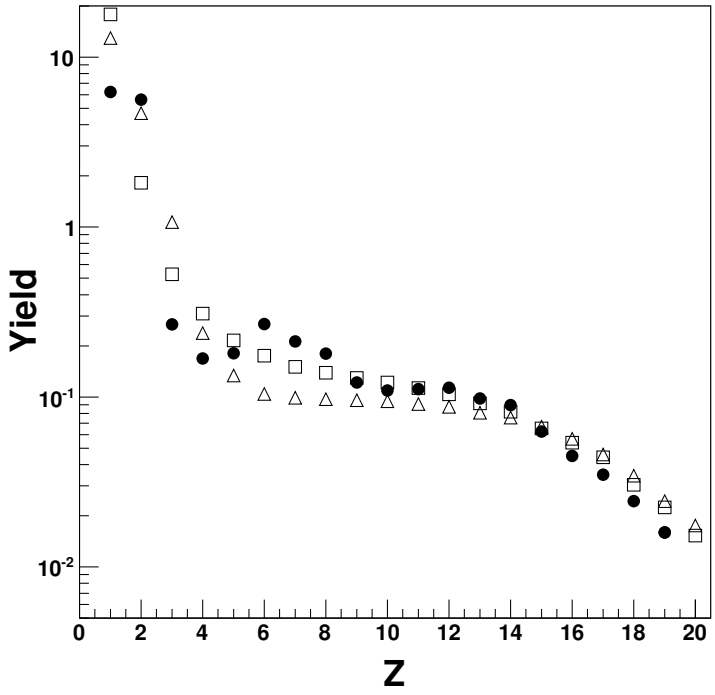

Figure 6.3: The charge distributions from experiment and simulation for $^{40}Ca+^{40}Ca$ at 35 MeV/A. Full circles refer to experimental data from [293], open squares refer to CoMD and open triangles refer to CoMD$_\alpha$.

As an example, we simulated $^{40}Ca+^{40}Ca$ heavy-ion collisions at beam energy $E_{lab}/A = 35$ MeV/A at fixed impact parameter $b = 1$ fm up to a maximum time 1000 fm/c. In Fig. 6.3, we plot the charge distribution of CoMD. The comparison to experimental data shows that we can not reproduce the experimental data completely. This is not surprising since we only have one fixed impact parameter in the model while the experimental data includes all the possible impact parameters. The experimental filter should be taken into account as well, but these features are not relevant to our goals. The important point is that the α yield is underestimated, a feature which can not be corrected by including other impact parameters or the

experimental filter.

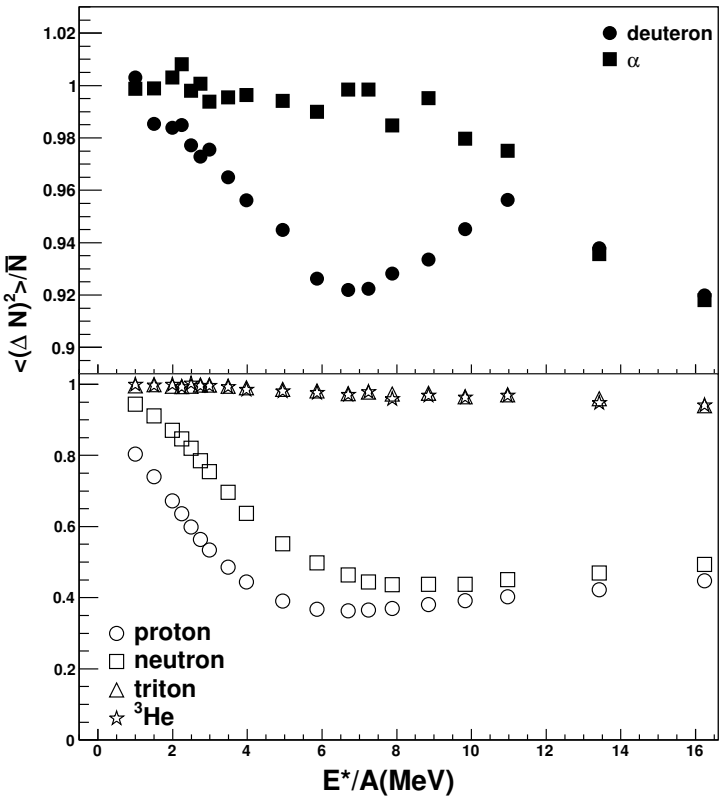

Figure 6.4: Normalized multiplicity fluctuation versus excitation energy per nucleon. (Top panel) CoMD results for d (full circles) and α particles (full squares). For comparison the normalized multiplicity fluctuations for fermions (bottom panel) [283]. (Open) Circles, squares and triangles refer to p, n and t, stars refer to ^3He. Notice the change of scales in the two panels.

We repeat the same simulations as before using CoMD$_\alpha$. The charge distribution so obtained is also plotted in Fig. 6.3. CoMD$_\alpha$ is now much closer to experimental data due to the implemented boson correlations. We have also addressed the question

if d-d collisions (or d-α) should also be implemented as well. We have tested such a possibility in collisions at 35 MeV/A by adding a d-d collision term similar to the α case. We found no difference with the case where α-α collisions only are included. This is easy to understand: d nuclei are less bound and easily destroyed in the hot matter. They form at the end of the reaction when the density is low [266]. Thus their properties are the result of decay from excited α particles or recombination of p and n in low density matter. As we will show their behavior is somewhat intermediate between that of fermions (p, n, t ...) and bosons (α particles).

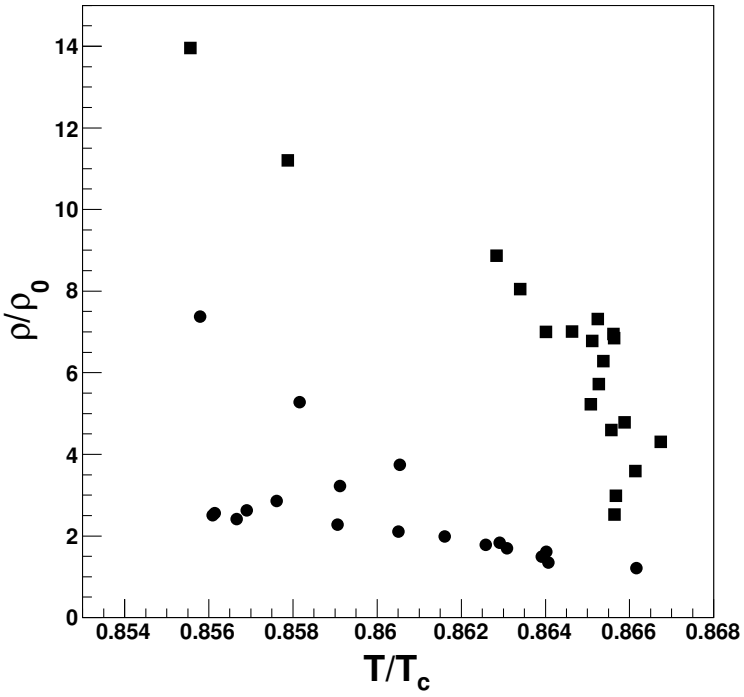

Figure 6.5: Reduced density versus reduced temperature for bosons. Symbols as in Fig. 6.4.

In Fig. 6.4, we plot the reduced variances versus excitation energy per nucleon for

CoMD. The boson results are given by the full symbols (top panel). As we see in the figure, α-normalized fluctuations are generally larger than d-normalized fluctuations [266]. As we will show below, this implies that those particles might explore different regions of densities and temperatures. In both cases, fluctuations are large and, in some cases, above Poissonian for α's. In order to understand if a BEC occurs in the model (and in the future in experiments) it is instructive to compare the boson normalized fluctuations to those of fermions discussed in ref. [283, 284, 285]. In Fig. 6.4 (bottom panel), normalized fermion fluctuations are given.

As we see the normalized fluctuations of p and n are much smaller than 1 at variance with the boson case, which would suggest a condensate. The quenching of fermion fluctuations has been recently observed in well selected data [171, 319]. However, heavier fermion clusters such as ^3He and t, display fluctuations larger than d and smaller than α. These facts are important to understand what is happening in the model and eventually search for an experimental confirmation. We offer here an intuitive explanation of the relative role of normalized fluctuations for different particles. The CoMD model is essentially classical with a constraint in the equations of motion which keeps the occupation probability $\bar{f}(r_i, p_i, t)$ smaller than 1 as dictated by the Pauli principle for fermions [8, 78, 86, 243, 250, 251, 252, 253]. A further implementation of the Pauli principle is in the collision term which avoids letting colliding nucleons occupy phase space regions which are occupied by other nucleons. Thus the Pauli principle reduces the available phase space and in turn the normalized fluctuations. For this reason p and n fluctuations are smaller than Poissonian. When composite fragments are formed, d, t, etc., the effect of Pauli blocking is reduced (also because those particles form at low densities, see below), thus fluctuations become comparable to their average value. The effect that reduces the available phase space is now the binding energy [266]. Not all nucleons can form a bound state, especially

if their relative kinetic energies are larger than the potential energy. For this reason d fluctuations are smaller than ^3He, t and smaller than α fluctuations.

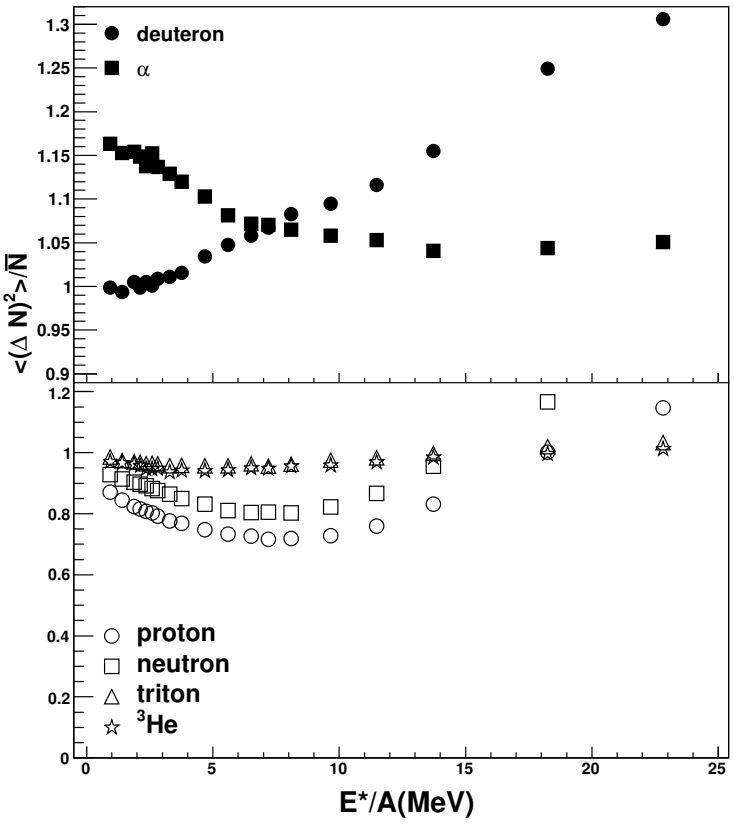

Figure 6.6: Normalized multiplicity fluctuation versus excitation energy per nucleon. (Top panel) CoMD$_\alpha$ results for d (full circles) and α particles (full squares). For comparison the normalized fluctuations for fermions (bottom panel). (Open) Circles, squares and triangles refer to p, n and t, stars refer to ^3He. Notice the change of scales in the two panels. The d-fluctuations keep increasing at high energies because they are produced from the decay of α excited clusters. Similarly for the large fluctuations observed for p and n.

It is interesting to discuss the densities 'seen' by the different bosons during the reaction in CoMD. Since most of the multiplicity fluctuations are less than 1 for d and α in Fig. 6.4, we assume there is a BEC below the critical point. Using Eqs. (6.2, 6.13), we can obtain T, T_c and ρ. A plot of reduced density (divided by the ground state density) versus $\frac{T}{T_c}$ is given in Fig. 6.5. It seems that the α's densities are too high thus unphysical. This is not surprising since there is only the Pauli blocking constraint and no Bose-Einstein factor in CoMD.

Let us turn now to CoMD$_\alpha$ which includes the Pauli blocking constraint and the Bose-Einstein factor. Similar to Fig. 6.4, we plot the reduced variances versus excitation energy per nucleon in Fig. 6.6. As we see in the figure, d and α-normalized fluctuations are generally larger than 1 (top panel). The multiplicity fluctuations of fermions (bottom panel) are less than 1 for most of the excitation energies. These results are what we expect. Since we consider the Pauli blocking for fermions and Bose-Einstein factor for bosons, the quantum effects for fermions and bosons should show up through the multiplicity fluctuations even if the system is a mixture of fermions and bosons. When the excitation energy is very high, the normalized fluctuations of fermions are larger than 1 as well, this suggests that the α particles are so excited to emit nucleons or d which carry the original large fluctuations of the parent. We also notice that the excitation energy of CoMD$_\alpha$ in Fig. 6.6 is larger than that of CoMD in Fig. 6.4 with the same beam energy. This simply tells us that we have more thermalization in CoMD$_\alpha$ than CoMD because of the large number of collisions in CoMD$_\alpha$, including the α-α collisions.

In Fig. 6.7, we plot the reduced densities for d and α versus reduced temperatures assuming the temperature is below the critical temperature (top panel) and the temperature is above the critical temperature (bottom panel). From Fig. 6.7, one can see that below the critical temperature, the α's densities are too high and unphysical.

But the densities of bosons are reasonable assuming the temperature is above critical temperature. Using the method in [283, 284], we can also estimate the densities for fermions, i.e. p and n.

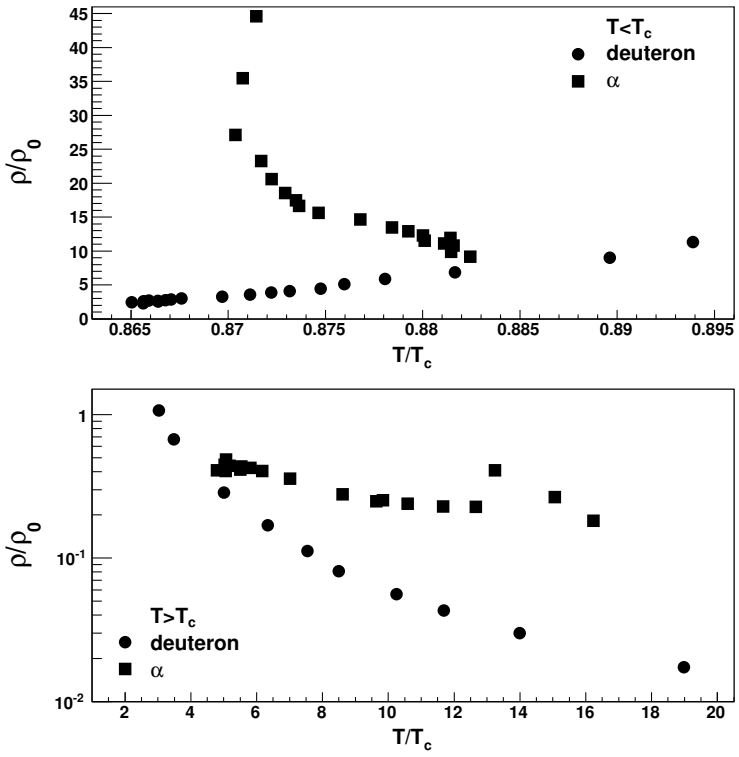

Figure 6.7: (Top panel) Reduced density versus reduced temperature for bosons assuming $T < T_c$; (Bottom panel) reduced density versus reduced temperature for bosons assuming $T > T_c$. Full circles refer to d and full squares refer to α.

To see the density difference between bosons and fermions at the same beam energy in the center of mass. We define the density ratio $\frac{\rho_B}{\rho_F} = \frac{4\rho_\alpha}{\bar{\rho}_{pn}}$ or $\frac{2\rho_d}{\bar{\rho}_{pn}}$ where $\bar{\rho}_{pn}$ is the average density of p and n. The density ratio between bosons and fermions versus the beam energies in the center of mass is plotted in Fig. 6.8. The results

of α particles at all beam energies and d at high beam energies are comparable to the results in the boson and fermion mixture gas which displays a BEC [313, 314, 315, 316, 317, 318]. The densities of d are smaller than the densities of fermions at low beam energies due to the different mechanism for their formation at different excitation energies. In particular at high excitation energy they are mainly produced from excited α-decay, thus testing a similar α-density. Comparing Figs. 6.7 and 6.8, it is evident that fermions are emitted from a low density region of the nucleus while the α particles are always at much higher density: this is the phenomenon of BEC.

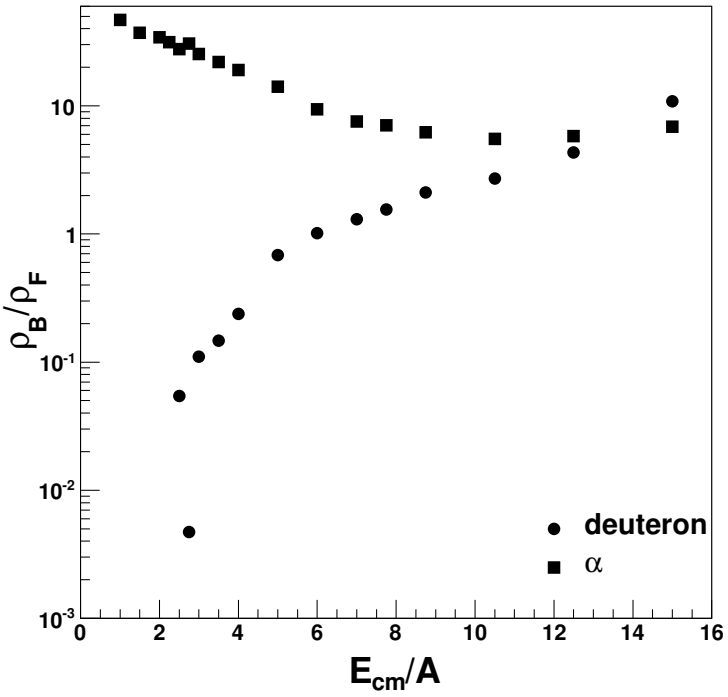

Figure 6.8: The bosons and fermions density ratio versus energy per nucleon in center of mass. Full circles refer to d and full squares refer to α.

7. COULOMB CORRECTIONS TO DENSITY AND TEMPERATURE OF BOSONS FROM QUANTUM FLUCTUATIONS*

In the last chapter, we have addressed a general approach for deriving densities and temperatures of bosons. We apply our approach to the simulation data of CoMD and CoMD$_\alpha$ and obtain densities and temperatures at each bombarding energy. We have seen that different particles like α and d explore different density and temperature regions, similar to the fermion case [283, 284, 285]. We also have seen that the density ratio between bosons and fermions is similar to the case in the boson and fermion mixture gas which displays a BEC [313, 314, 315, 316, 317, 318]. However, improvements are needed to extract the density of bosons below the critical temperature. While for fluctuations we have used the Landau's theory assuming a second order phase transition, the density has been derived assuming a non interacting Bose gas. In this chapter, we will modify our method to take into account distortions due to Coulomb field.

In chapter 5, we have discussed Coulomb corrections to fermions and in this chapter we will concentrate on bosons, i.e. α and d particles. The case was also discussed in [283, 284] but without Coulomb corrections. It is well known that ideal Bose gases give unphysical results near and below the critical point. These problems are mitigated or completely solved especially when the boson experience some repulsive potential [320]. This is surely the case for α and d where at least the Coulomb repulsion must be included. For bosons it is not possible to disentangle the 'temperature' from the critical temperature T_c, thus the density [286]. In [285]

*Reprinted with permission from "Coulomb corrections to density and temperature of bosons in heavy ion collisions" by Hua Zheng, Gianluca Giuliani and Aldo Bonasera, 2013. Physical Review C 88, 024607, Copyright 2013 by American Physical Society.

we showed that Coulomb corrections result in similar T for different nuclei having the same mass number. We also showed that the Coulomb repulsion of different charged particles can distort the value of the temperature obtained from QF, which depends on kinetic values. On the other hand, MF for different particles seem to be independent on Coulomb effects as we have discussed in [285, 286]. Also the obtained values, say of the critical temperature and density, might be influenced by Coulomb as well as by finite size effects. For these reasons, it is highly needed to correct for these effects as best as possible. It is the goal to propose a method to correct for Coulomb effects in the exit channel of produced charged particles. In order to support our findings, we will compare our results to the neutron case, which is of course independent, at least not directly, from the Coulomb force.

7.1 Quantum Case–Bosons

We will restrict the results to the d and α cases. In the quantum case considering the Coulomb correction, the QF can be obtained from:

$$\langle Q_{xy}^2 \rangle = (2mT)^2 \frac{4}{15} \frac{\int_0^\infty dy y^{\frac{5}{2}} \frac{1}{e^{y+\frac{A'}{yVT^2}-\nu}-1}}{\int_0^\infty dy y^{\frac{1}{2}} \frac{1}{e^{y+\frac{A'}{yVT^2}-\nu}-1}}, \tag{7.1}$$

where $A' = \frac{1.44 \times 4\pi\hbar^2 q_1 q_2}{2m}$ and $\nu = \frac{\mu}{T}$. On the same ground we can derive the MF as:

$$\frac{\langle (\Delta N)^2 \rangle}{\bar{N}} = \frac{\int_0^\infty dy y^{\frac{1}{2}} \frac{e^{y+\frac{A'}{yVT^2}-\nu}}{(e^{y+\frac{A'}{yVT^2}-\nu}-1)^2}}{\int_0^\infty dy y^{\frac{1}{2}} \frac{1}{e^{y+\frac{A'}{yVT^2}-\nu}-1}}. \tag{7.2}$$

The derivation of Eqs. (7.1, 7.2) is similar to the case of fermions in appendix D. We only need to change the sign in the distribution function. We introduce three variables T, V and ν into Eqs. (7.1, 7.2). This means that to solve those equations

we need one more condition. We choose the average multiplicity:

$$\bar{N} = \frac{gV}{h^3} 4\pi \frac{(2mT)^{\frac{3}{2}}}{2} \int_0^\infty dy y^{\frac{1}{2}} \frac{1}{e^{y+\frac{A'}{yVT^2}-\nu} - 1}. \tag{7.3}$$

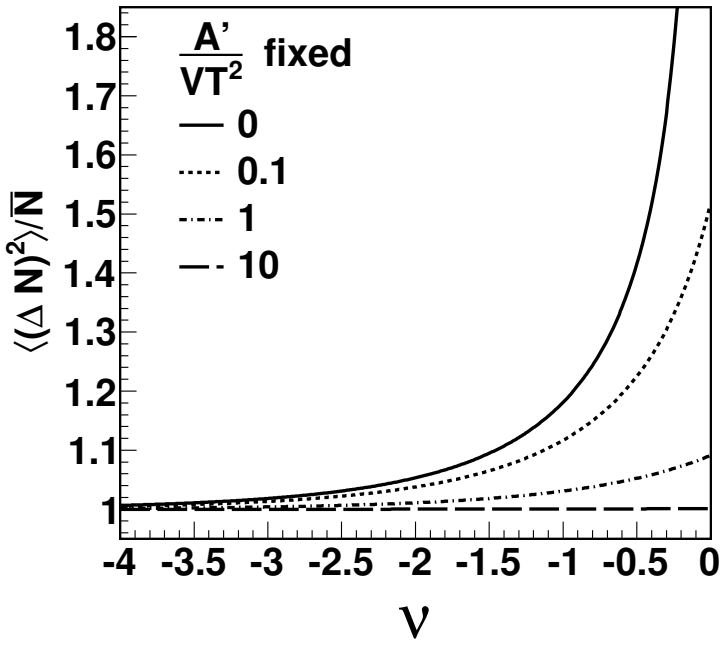

Figure 7.1: The multiplicity fluctuation versus ν with fixed $\frac{A'}{VT^2}$ in Eq. (7.2). Different lines refer to different values of $\frac{A'}{VT^2}$.

Those equations can be solved numerically. In Fig. 7.1 we plot the $\frac{\langle(\Delta N)^2\rangle}{\bar{N}}$ vs ν with fixed $\frac{A'}{VT^2}$ in Eq. (7.2). One can see that the $\frac{\langle(\Delta N)^2\rangle}{\bar{N}}$ is always larger than 1. When $\frac{A'}{VT^2} = 0$, i.e. no Coulomb correction, the $\frac{\langle(\Delta N)^2\rangle}{\bar{N}}$ recovers the ideal Bose gas result when $T > T_c$ [286] and it diverges at the critical point. For $T < T_c$, $\nu = 0$ and we get a Bose condensate. An interesting question is what the energy of the

condensate is in the case with Coulomb repulsion. Of course, we should first stress that we are dealing with finite systems. The Coulomb term gives a correction which has some similarities with the repulsive potential used in realistic Bose gases as first proposed by Bogoliubov [1, 321, 322]. For simplicity we will assume that the ground state energy of the condensate is given by an uniformly charged sphere of radius r. However, in the following we do not need any information on the ground state of the system and we have included this discussion just for completeness. We can rewrite Eq. (7.3) as

$$\rho = \frac{g}{h^3} 4\pi \frac{(2mT)^{\frac{3}{2}}}{2} \int_0^\infty dy y^{\frac{1}{2}} \frac{1}{e^{y+\frac{A'}{yVT^2}-\nu} - 1}. \tag{7.4}$$

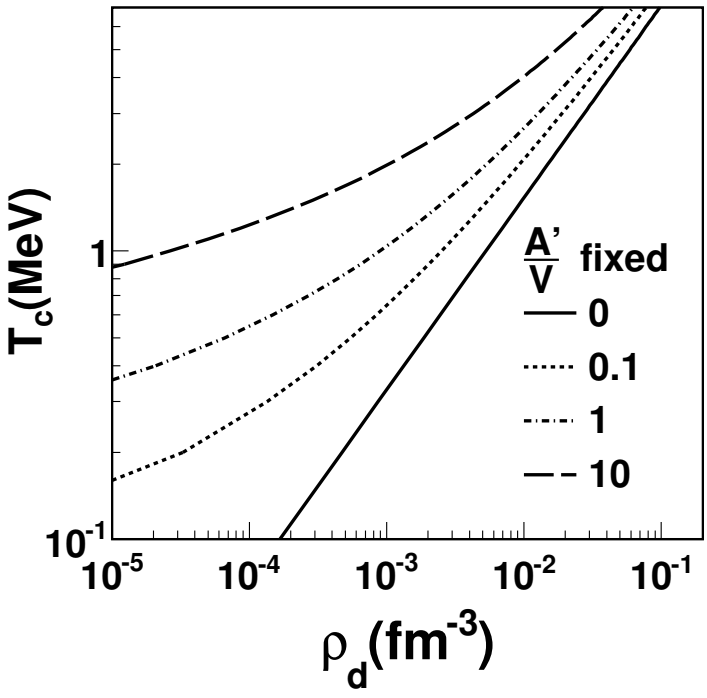

Figure 7.2: Critical temperature versus density with fixed $\frac{A'}{V}$. We take d as an example.

In Fig. 7.2, we plot the critical temperature versus density for different values of $\frac{A'}{V}$. For a fixed density and volume, the Coulomb energy is larger and the critical temperature is higher. This probably provides a larger chance for bosons to reach the lowest energy state.

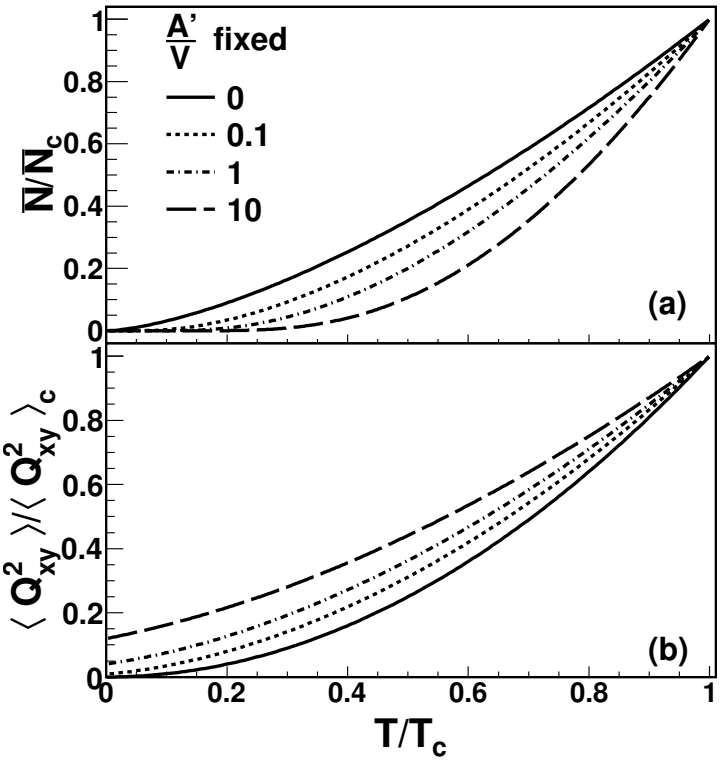

Figure 7.3: $\bar{N}$ of bosons (top panel) and quadrupole momentum fluctuations (bottom panel) divided by their respective values at the critical point vs T/T_c. This result is, to a very good approximation, independent on the particle type (i.e. α or d) at one fixed density.

It is instructive to study the behavior of the quadrupole momentum fluctuations

and the density below the critical point. In Fig. 7.3 we plot these quantities divided by their values at the critical temperature as function of T/T_c. The behavior when the Coulomb term is zero ($A' = 0$) was already discussed in [286]. For finite Coulomb potential, we observe that the number of condensate bosons increases faster with decreasing T and accordingly the quadrupole momentum fluctuations are larger. In fact the larger the Coulomb repulsion, the higher are the fluctuations already at zero T, which is intuitively clear: particles emitted from a source at zero T, because of the large Coulomb acceleration will develop substantial final momenta and consequently large fluctuations. Naturally, we have to keep in mind that at zero T, bosons might be confined by an attractive mean field.

In Fig. 7.4 we plot $\tilde{\rho} = \frac{\rho}{\rho_0}$ where ρ_0 is the nucleons ground state density and T vs excitation energy respectively obtained from CoMD simulations. The neutron case is also included [283, 284, 285]. As we see the derived density of d and α with Coulomb correction are very close to the neutrons and of course to each other. There is a large difference between the cases with Coulomb correction and without Coulomb correction which demonstrate the crucial role of adding the Coulomb repulsion among bosons. For completeness we also include the results for bosons from Landau's $O(m^6)$ approach [286] which is close to the results without Coulomb corrections. The derived T of d and α with Coulomb correction are also much closer to the neutrons. The good agreement for the obtained temperatures and densities suggests that thermal equilibrium in the transverse direction is nearly reached.

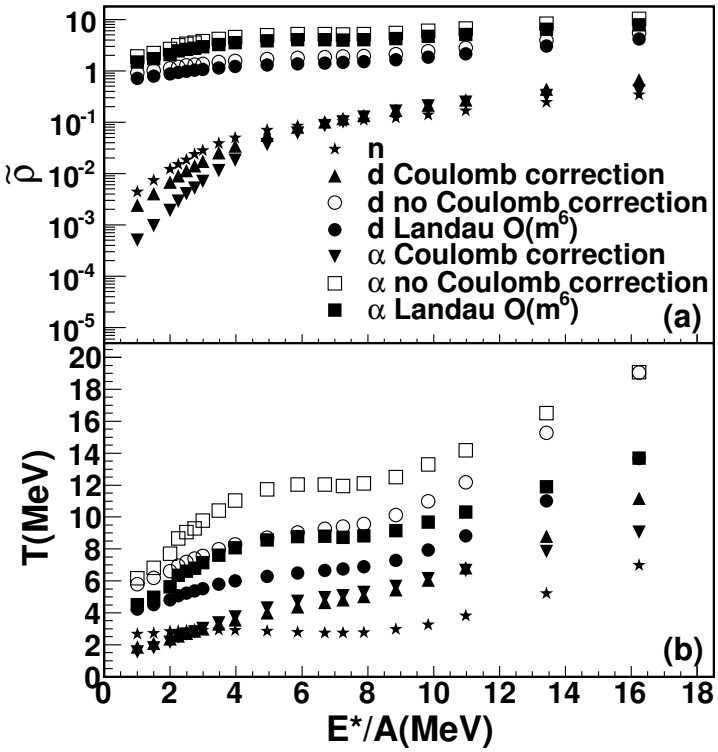

Figure 7.4: The reduced density (top panel) and temperature T (bottom panel) versus E^*/A of d and α from CoMD simulations. Three methods, with Coulomb correction, without Coulomb correction and Landau's $O(m^6)$ theory, are used to calculate the density and temperature. The neutron's corresponding results are also included as a reference.

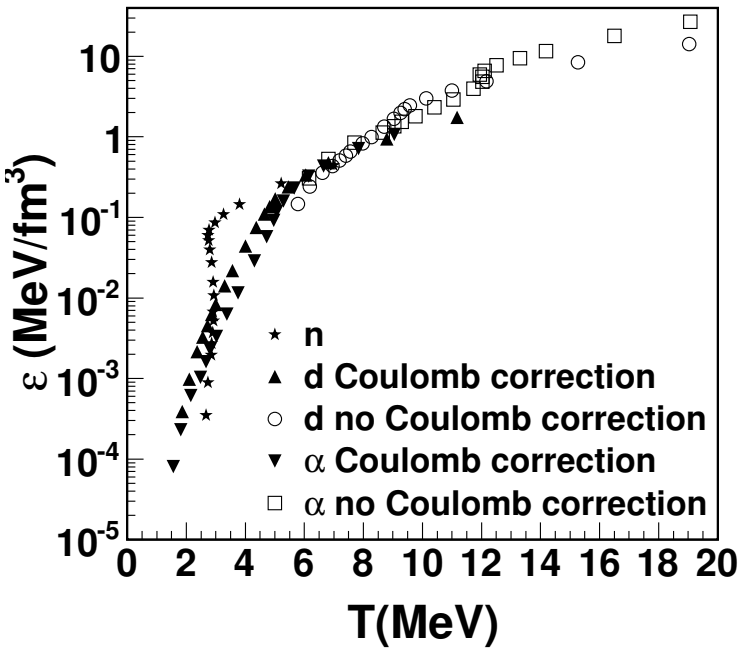

Figure 7.5: Energy density versus T for different cases, see Fig. 7.4.

In Fig. 7.5, we plot the energy density $\varepsilon = \frac{E}{N}\rho$ versus T. Without Coulomb corrections, the results are systematically located at larger T and energy density respect to n. When including the correction, we obtain a curve very close to the neutrons which of course do not feel Coulomb (at least not directly) and furthermore they are fermions. This result shows that when all the different effects are properly taken into account, we obtain a unique energy density behavior which demonstrate that different particles experience a sudden increase of the degrees of freedom (fragmentation) at the same T about 4 MeV. At higher T the energy density increases because of a liquid-gas phase transition. It is important to notice that our results but also other results in the literature [171, 172, 173, 174, 266, 298, 301] seem to give always T smaller than the temperature at the critical point for a liquid-gas phase

transition. The impossibility of reaching T_c was also predicted in microscopic dynamical calculations of the Lyapunov exponents. In those calculation, the Lyapunov exponents will not increase beyond a certain value since collective effects will set in [179]. We stress that the critical temperature for a liquid-gas phase transition has nothing to do, in principle, with the critical point of a Bose condensate. The CoMD model used has no knowledge of a Bose condensate, thus we do not expect any spectacular effect to be observable in Fig. 7.5. However, there are many signatures of a possible condensate in nuclei even though none has been so far conclusive. We mention the Hoyle state in ^{12}C, but also the anomalous large number of α particles in the universe as compared to hydrogen. In heavy-ion collision a large production of alpha is observed in the collisions. Recently, some experimental signatures of a condensate have been proposed [68, 323]. In the calculations discussed here we have always implicitly assumed that the number of bosons is constant, which is crucial to have a condensate. In reality, during the collisions, even though we might start from 'perfect' α cluster nuclei, because of the large excitation energy, α particles might be destroyed and thus we obtain in general a mixture of fermions and bosons. This is of course especially severe for d-like events. In order to avoid this problem we propose the following strategy to select 'good' events. First we define the quantity:

$$b_j = \frac{1}{M}\sum_{i=1}^{M}\frac{(-1)^{Z_i}+(-1)^{N_i}}{2}, \tag{7.5}$$

where M is the multiplicity in one event, Z_i and N_i are the proton and neutron number in the i^{th} fragment in that event respectively. The meaning of such a quantity is clear: if the final fragments for instance are all d-like, we get $b_j = -1$, while for pure α like fragments $b_j = +1$. Pure fermion cases give $b_j = 0$. In Fig. 7.6 we plot the b_j distribution from CoMD calculations. As we see in the figure the model

gives an average b_j close to zero, which means that most of the final fragments in the model are 'fermion-like'. Recall that the model takes into account mainly the Pauli principle. However, preliminary experimental results on $^{40}Ca + ^{40}Ca$ collisions [312, 324], display much larger distributions than in Fig. 7.6. In particular events are observed near $b_j = \pm 1$ which could be a signature for a Bose condensate. Therefore, we propose to select fragments from data with $b_j = 1(-1)$ and perform the analysis to obtain the density and temperature of the bosons for each excitation energy. The energy density might be constructed for different situations and compared to fermions. The experimental analysis with b_j selection is in process [324].

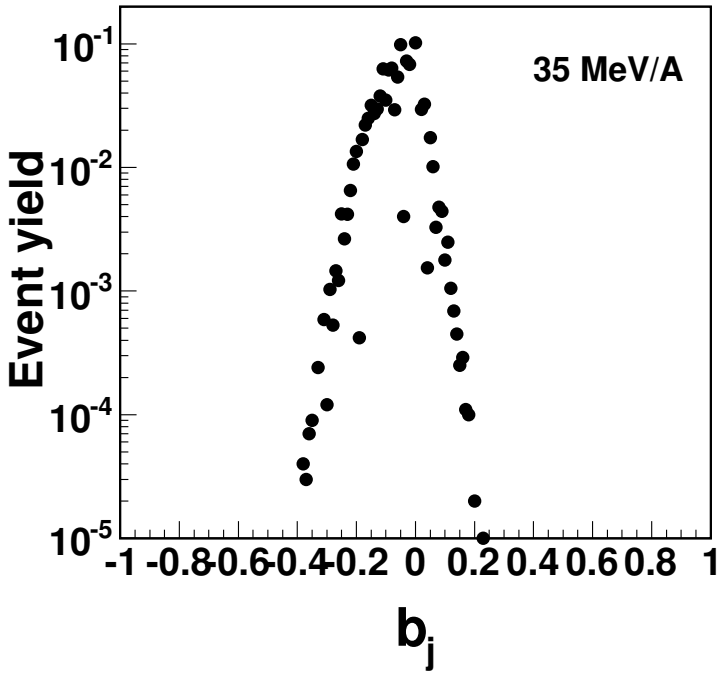

Figure 7.6: The b_j distribution for CoMD at 35 MeV/A.

8. CONCLUSIONS

A nucleus is a quantum many body system made of strongly interacting fermions, protons and neutrons (nucleons). This produces a rich Nuclear Equation of State (NEOS) which is usually a function of density and temperature and whose knowledge is crucial to our understanding of the composition and evolution of celestial objects. Several hundreds of NEOS have been proposed in the literature. The heavy-ion collisions experimental data and celestial observations (e.g. neutron star) have been used to reduce this inflation and try to pin down the NEOS. But the methods used to extract the temperature and density information of nuclear matter for NEOS from experimental data are either with full classical assumptions or hybrid with classical and quantum assumptions.

There are at least five thermometers and five methods to extract density respectively. The five thermometers are: the slopes of the kinetic energy spectra, discrete state population ratios of selected isotopes, double isotopic yield ratios, quadrupole momentum fluctuation (these four thermometers assume particles following Maxwell-Boltzmann distribution) and level density which has the form $E^* = a(E^*)T^2$ (this is similar to the formula for free Fermi gas at low temperature approximation). The five methods to extract density are: Albergo method which is in the framework of classical assumption, Guggenheim approach (the universal scaling law for real gases), two particle correlation, coalescence model and level density assuming $E^* = a(\rho)T^2$ (the last three methods implement the quantum effects of particles in some sense). In the past studies of the NEOS, the different combinations of the thermometers and the methods to extract density were used.

In this dissertation, we have addressed a general approach implementing quantum

effects for deriving densities and temperatures (both fermions and bosons) based on the quadrupole momentum fluctuations and multiplicity fluctuations. In our approach, we treat fermions and bosons separately even though both of them are produced in heavy-ion collisions. This is similar to the mixture of trapped Fermi and Bose gases where the quantum effects for both gases are observed. In order to see how our approach works, we apply it to the $^{40}Ca +^{40} Ca$ at impact parameter $b = 1$ fm up to 1000 fm/c simulation data from CoMD which includes the Fermi statistics and a modified version of the model CoMD$_\alpha$, to include the possibility of α-α collisions. The relevant Bose-Einstein factor in the collision term is properly taken into account.

For the fermion case, we have derived the analytical formulas in terms of T and $\frac{T}{\varepsilon_f}$ for quadrupole momentum fluctuation and multiplicity fluctuation in the low temperature approximation. We found that the quadrupole momentum fluctuation can be written as the product of the classical results and a quantum correction factor. This explicitly shows the quantum effects of fermions when we extract temperature information from heavy-ion collisions data. Since the quantum correction factor is larger than 1, the quantum temperature is smaller than the classical one which is similar to the result found by Bauer in 1995 in order to explain the large 'apparent' temperature in particles spectra. In our approach, we calculate the densities of fermions through their Fermi energies ε_f which can be derived from quadrupole momentum fluctuations and multiplicity fluctuations. Analyzing the data from CoMD, the results confirmed that the classical approximation is unjustified. From the results, we have been able to bridge low energy phenomenology, i.e. particles evaporation from the surface, with the fragmentation of the system. We also found that different particles like p and n explore different density and temperature regions.

To test the validity of the low temperature approximation in Fermi systems, we

derived formulas for quadrupole momentum fluctuation and multiplicity fluctuation without approximations. We have shown that for high temperatures and small densities the classical result is recovered as expected. However, we have shown in CoMD calculations that the numerical results give small differences in the physical observables considered in this dissertation but they could become large when approaching the classical limit. To overcome this problem we have produced suitable parameterizations of quadrupole and multiplicity fluctuations which are valid for fermions at all temperatures and densities. In addition to those, we determined the entropy from normalized quantum fluctuations. We have also shown that the entropy can be determined in some limit from the ratio of the number of deuterons to protons or neutrons produced in the collisions. Especially the neutrons seem to give cleaner result but of course they are more difficult to determine experimentally since the neutrons are usually not measured or measured with very low efficiency.

From the numerical results of p and n, we can see that the Coulomb effects play a role with charged particles in heavy-ion collisions. To explore our method even further, we introduce the Coulomb correction for charged particles. A method borrowed from electron scattering was adopted. We have discussed Coulomb corrections when extracting densities and temperatures of nuclear systems produced in heavy-ion collisions. The classical and quantum cases (fermions only) have been discussed. We have shown that in both cases, the temperatures obtained from different particle types are very similar to the neutron's one which implies the 'near ergodicity' of the system. On the other hand the densities are different for different particles, which suggests that the Coulomb dynamics is of course important also before the breaking of the source. The energy densities are very similar at high temperatures, which implies that Coulomb corrections are small due to the small source densities.

For bosons, the results are a little bit more complicated but more interesting, since

they might undergo Bose-Einstein condensate (BEC). Therefore, we have to assume that $T < T_c$ or $T > T_c$ when we do the data analysis for bosons. When $T < T_c$, the multiplicity fluctuations are always infinite since the isothermal compressibility diverges for ideal bosons. This phenomenon is of course not observed in experiments. Therefore, we need to include interactions between bosons (and fermions if present) near the critical point. We use Landau's $O(m^6)$ phase transition theory near the critical point to obtain the multiplicity fluctuations for bosons. Analyzing CoMD and CoMD$_\alpha$ data, we have seen that different particles like d and α explore different density and temperature regions, similar to the fermion case. We also have seen that the density ratio between bosons and fermions is similar to the case in the boson and fermion mixture gas which displays a BEC. We suggest that multiplicity fluctuations larger than one for bosons, in contrast to fermions multiplicity fluctuations which are smaller than one, is a signature of a BEC in nuclei. However, improvements are needed to extract the density of bosons below the critical temperature.

Since the Coulomb correction is necessary as we have seen for fermions, we apply the same Coulomb correction to the boson case. We have shown that the temperatures obtained from different particle types are very similar to the neutron's one which implies the 'near ergodicity' of the system. The energy densities are very similar at high temperatures, which suggests that Coulomb corrections are small due to the small source densities. Experimental investigations of the effects discussed for well determined sources and excitation energies would be very important to further constrain the Nuclear Equation of State in the liquid-gas phase transition region also for asymmetric matter. We suggest to select data according to their b_j distribution as defined in this dissertation. The T, ρ and energy density for d-like, α-like and fermion like events might be compared to pin down the possibility of a condensate in nuclei.

The application of these ideas in experiments has produced interesting results such as the sensitivity of the temperature from the symmetry energy, fermion quenching and the critical T and ρ in asymmetric matter. Very surprisingly, the method based on quantum fluctuations gives values of T and ρ very similar to those obtained using the double ratio method and coalescence and gives a good determination of the critical exponent β. This stresses the question on why sometimes different methods give different values, including different particles ratios, while in other cases the same values are obtained. To address this question, a systematic analysis to the same experimental data with different thermometers and methods to extract density and the comparison of the results are needed.

REFERENCES

[1] L. Landau and F. Lifshits, *Statistical Physics* (Pergamon, New York,1980); E.M. Lifshitz and L.P. Pitaevskii, *Statistical Physics* (Reprinted by Beijing World publishing Corporation by arrangement with Butterworth-Heinemann, 1999).

[2] A. Bohr and B.R. Mottelson, *Nuclear Structure* (World Scientific, Singapore, 1998).

[3] P. Ring and P. Schuck, *The Nuclear Many-Body Problem,* 3rd ed. (Springer, New York, 2004).

[4] M.A. Preston and R.K. Bhaduri, *Structure of the Nucleus,* (Addison-Wesley, 1975).

[5] B. Povh, K. Rith, C. Scholz and F. Zetsche, *Particles and Nuclei,* 6th ed. (Springer, Berlin, 2008).

[6] A. Bonasera, J. Natowitz and Y.El Masri, *Nuclear Science and its applications*, (Taylor & Francis eds., Baton Rouge, Fl-USA, in preparation).

[7] K. Huang, *Statistical Mechanics*, 2nd ed. (J. Wiley and Sons, New York, 1987).

[8] G.F. Bertsch and S. Das Gupta, Phys. Rep. **160**, 189 (1988).

[9] S. Kimura and A. Bonasera, Phys. Rev. A **72**, 014703 (2005).

[10] M.R. Anders *et al.*, Phys. Rev. C **87**, 024303 (2013).

[11] Y.-W. Lui *et al.*, Phys. Rev. C **83**, 044327 (2011).

[12] D.H. Youngblood, H.L. Clark and Y.-W. Lui, Phys. Rev. Lett. **82**, 691 (1999).

[13] D.H. Youngblood *et al.*, Phys. Rev. C **69**, 034315 (2004).

[14] J. Piekarewicz, J. Phys. G: Nucl. Part. Phys. **37**, 064038 (2010).

[15] W.C. Chen, J. Piekarewicz and M. Centelles, Phys. Rev. C **88**, 024319 (2013).

[16] E. Lipparini and S. Stringari, Phys. Rep. **175**, 103 (1989).

[17] L.G. Cao, H. Sagawa and G. Colò, Phys. Rev. C **86**, 054313 (2012).

[18] E. Khan, N. Paar, D. Vretenar, L.G. Cao, H. Sagawa and G. Colò, Phys. Rev. C **87**, 064311 (2013).

[19] E. Khan, N. Paar and D. Vretenar, Phys. Rev. C **84**, 051301(R) (2011).

[20] G. Colò, U. Garg and H. Sagawa, Eur. Phys. J. A **50**, 26 (2014).

[21] J.P. Blaizot, Phys. Rep. **64**, 171 (1980).

[22] L.D. Landau and E.M. Lifshitz, *Fluid Mechanics*, 2nd ed. (Pergamon Press, 1987).

[23] G.F. Bertsch, Nucl. Phys. A **249**, 253 (1975).

[24] R.V. Wagoner, W.A. Fowler and F. Hoyle, Astrophysical Journal **148**, 3 (1967).

[25] R.V. Wagoner, Astrophysical Journal **179**, 343 (1973).

[26] M.S. Smith, L.H. Kawano and R.A. Malaney, Astrophys. J. Suppl. Ser. **85**, 219 (1993).

[27] A.M. Bosegaard and G. Steigman, Ann. Rev. Astron. Astrophys. **23**, 319 (1985).

[28] B.W. Carroll and D.A. Ostlie, *An Introduction to Modern Astrophysics,* 2nd ed. (Pearson, San Francisco, 2007).

[29] N. Suzuki *et al.*, Astrophysical Journal **746**, 85 (2012).

[30] http://supernova.lbl.gov/Union/

[31] J.M. Lattimer and M. Prakash, Phys. Rep. **333**, 121 (2000).

[32] T. Klähn *et al.*, Phys. Lett. B **654**, 170 (2007).

[33] S.M. Ransom *et al.*, Science **307**, 892 (2005).

[34] D.J. Nice *et al.*, Astrophysical Journal **634**, 1242 (2005).

[35] J.M. Lattimer and M. Prakash, Science **304**, 536 (2004).

[36] A.W. Steiner, J.M. Lattimer and E.F. Brown, Astrophysical Journal **722**, 33 (2010).

[37] J.M. Lattimer, Ann. Rev. Nucl. Part. Sci. **62**, 485 (2012).

[38] F. Özel, T. Güver and D. Psaltis, Astrophysical Journal **693**, 1775 (2009).

[39] F. Özel, G. Baym and T. Güver, Phys. Rev. D **82**, 101301(R) (2010).

[40] T. Güver, F. Özel, A. Cabrera-Lavers and P. Wroblewski, Astrophysical Journal **712**, 964 (2010).

[41] T. Güver, P. Wroblewski, L. Camarota and F. Özel, Astrophysical Journal **719**, 1807 (2010).

[42] P.B. Demorest *et al.*, Nature **467**, 1081 (2010).

[43] S. Guillot, M. Servillat, N.A. Webb and R.E. Rutledge, Astrophysical Journal **772**, 7 (2013).

[44] J.M. Lattimer and M. Prakash, Phys. Rep. **442**, 109 (2007).

[45] K.H. Ackermann *et al.*, Phys. Rev. Lett. **86**, 402 (2001).

[46] J. Adams *et al.*, Nucl. Phys. A **757**, 102 (2005).

[47] S.S Adler *et al.*, Phys. Rev. Lett. **91**, 182301 (2003).

[48] K. Adcox *et al.*, Nucl. Phys. A **757**, 184 (2005).

[49] K. Aamodt *et al.*, Phys. Rev. Lett. **105**, 252302 (2010).

[50] Alice Collaboration, Phys. Lett. B **696**, 30 (2011).

[51] R.K. Pathria, *Statistical Mechanics*, 2nd ed. (Elsevier Pte Ltd, Singapore, 2003).

[52] M.B. Tsang *et al.*, Phys. Rev. Lett. **102**, 122701 (2009).

[53] M.B. Tsang *et al.*, Progress in Particle and Nuclear Physics **66**, 400 (2011).

[54] G. Chiaki, T. Nozawa and N. Yoshida, The Astrophysical Journal Letters **765**, L3 (2013).

[55] D. Page, M. Prakash, J.M. Lattimer and A.W. Steiner, Phys. Rev. Lett. **106**, 081101 (2011).

[56] R.F. Casten and B.M. Sherrill, Progress in Particle and Nuclear Physics **45**, S171 (2000).

[57] A. Stern, Nature **464**, 187 (2010).

[58] H. Zheng and A. Bonasera, Phys. Rev. C **83**, 057602 (2011).

[59] S. Ohkubo and Y. Hirabayashi, Phys. Lett. B **684**, 127 (2010).

[60] S. Ohkubo, arXiv: 1301.7485.

[61] T. Kokalova, N. Itagaki, W. Von Oertzen and C. Wheldon, Phys. Rev. Lett. **96**, 192502 (2006).

[62] A. Tohsaki, H. Horiuchi, P. Schuck and G. Röpke, Phys. Rev. Lett. **87**, 192501 (2001).

[63] G. Röpke, A. Schnell and P. Schuck, Phys. Rev. Lett. **80**, 3177 (1998).

[64] T. Sogo, G. Röpke, and P. Schuck, Phys. Rev. C **82**, 034322 (2010).

[65] Y. Funaki *et al.*, Phys. Rev. C **82**, 024312 (2010).

[66] Y. Funaki *et al.*, Int. J. Mod. Phys. E **20**, 874 (2011).

[67] Y. Funaki *et al.*, Prog. Theor. Phys. **108**, 297 (2002).

[68] Ad.R. Raduta *et al.*, Phys. Lett. B **705**, 65 (2011).

[69] P. Schuck, arXiv: 1303.2943.

[70] H. Zheng, G. Giuliani and A. Bonasera, Phys. Rev. C **88**, 024607 (2013).

[71] R.P. Smith, R.L.D. Campbell, N. Tammuz and Z. Hadzibabic, Phys. Rev. Lett. **106**, 250403 (2011).

[72] J. Esteve *et al.*, Phys. Rev. Lett. **96**, 130403 (2006).

[73] T. Müller *et al.*, Phys. Rev. Lett. **105**, 040401 (2010).

[74] C. Sanner *et al.*, Phys. Rev. Lett. **105**, 040402 (2010).

[75] C.I. Westbrook, Physics **3**, 59 (2010).

[76] B.A. Li, L.W. Chen and C.M. Ko, Phys. Rep. **464**, 113 (2008).

[77] A. Bonasera, R. Coniglione and P. Sapienza, Eur. Phys. J. A **30**, 47 (2006).

[78] A. Bonasera, F. Gulminelli and J. Molitoris, Phys. Rep. **243**, 1 (1994).

[79] A. Bonasera, M. Bruno, C.O. Dorso and P.F. Mastinu, La Rivista del Nuovo Cimento **23**, 2 (2000).

[80] J. Aichelin, Phys. Rep. **202**, 233 (1991).

[81] W. Cassing, V. Metag, U. Mosel and K. Niita, Phys. Rep. **188**, 363 (1990).

[82] L.P. Csernai and J.I. Kapusta, Phys. Rep. **131**, 223 (1986).

[83] C.B. Das, S. Das Gupta, W.G. Lynch, A.Z. Mekjian and M.B. Tsang, Phys. Rep. **406**, 1 (2005).

[84] A. Ono, H. Horiuchi, Progress in Particle and Nuclear Physics **53**, 501 (2004).

[85] H. Stöcker and W. Greiner, Phys. Rep. **137**, 277 (1986).

[86] M. Papa, G. Giuliani and A. Bonasera, Journal of Computational Physics **208**, 403 (2005).

[87] V. Baran, M. Colonna, V. Greco and M. Di Toro, Phys. Rep. **410**, 335 (2005).

[88] H. Feldmeier, Nucl. Phys. A **515**, 147 (1990).

[89] K. Vantournhout *et al.*, Progress in Particle and Nuclear Physics **66**, 271 (2011).

[90] J.P. Blaizot, D. Gogny and B. Grammaticos, Nucl. Phys. A **265**, 315 (1976).

[91] L.P. Csernai, *Introduction to Relativistic Heavy Ion Collisions,* (John Wiley & Sons Ltd, 1994).

[92] R. Magana, H. Zheng and A. Bonasera, Int. J. Mod. Phys. E **21**, 1250006 (2012).

[93] T.H.R. Skyrme, Nucl. Phys **9**, 615 (1959).

[94] J.R. Stone *et al.*, Phys. Rev. C **68**, 034324 (2003).

[95] M. Dutra *et al.*, Phys. Rev. C **85**, 035201 (2012).

[96] B.K. Agrawal, S. Shlomo and V. Kim Au, Phys. Rev. C **68**, 031304(R) (2003).

[97] B.K. Agrawal, S. Shlomo and V. Kim Au, Phys. Rev. C **72**, 014310 (2005).

[98] F. Tondeur, S. Goriely, J.M. Pearson and M. Onsi, Phys. Rev. C **62**, 024308 (2000).

[99] M. Farine, J.M. Pearson and F. Tondeur, Nucl. Phys. A **696**, 396 (2001).

[100] S. Goriely, J.M. Pearson and F. Tondeur, Nucl. Phys. A **688**, 349c (2001).

[101] M. Samyn, S. Goriely, P.H. Heenen, J.M. Pearson and F. Tondeur, Nucl. Phys. A **700**, 142 (2002).

[102] S. Goriely, M. Samyn, P.H. Heenen, J.M. Pearson and F. Tondeur, Phys. Rev. C **66**, 024326 (2002).

[103] M. Samyn, S. Goriely and J.M. Pearson, Nucl. Phys. A **725**, 69 (2003).

[104] S. Goriely, M. Samyn, M. Bender and J.M. Pearson, Phys. Rev. C **68**, 054325 (2003).

[105] M. Samyn, S. Goriely, M. Bender and J.M. Pearson, Phys. Rev. C **70**, 044309 (2004).

[106] S. Goriely, M. Samyn, J.M. Pearson and M. Onsi, Nucl. Phys. A **750**, 425 (2005).

[107] S. Goriely, M. Samyn and J.M. Pearson, Nucl. Phys. A **773**, 279 (2006).

[108] S. Goriely, M. Samyn and J.M. Pearson, Phys. Rev. C **75**, 064312 (2007).

[109] S. Goriely and J.M. Pearson, Phys. Rev. C **77**, 031301(R) (2008).

[110] N. Chamel, S. Goriely and J.M. Pearson, Nucl. Phys. A **812**, 72 (2008).

[111] S. Goriely, N. Chamel and J.M. Pearson, Phys. Rev. Lett. **102**, 152503 (2009).

[112] N. Chamel, S. Goriely and J.M. Pearson, Phys. Rev. C **80**, 065804 (2009).

[113] S. Goriely, N. Chamel and J.M. Pearson, Phys. Rev. C **82**, 035804 (2010).

[114] L.G. Cao, U. Lombardo, C.W. Shen and N.V. Giai, Phys. Rev. C **73**, 014313 (2006).

[115] A.W. Steiner, M. Prakash, J.M. Lattimer and P.J. Ellis, Phys. Rep. **411**, 325 (2005).

[116] M.M. Sharma, G. Lalazissis, J. König and P. Ring, Phys. Rev. Lett. **74**, 3744 (1995).

[117] L.W. Chen, C.M. Ko, B.A. Li and J. Xu, Phys. Rev. C **82**, 024321 (2010).

[118] P.G. Reinhard *et al.*, Phys. Rev. C **60**, 014316 (1999).

[119] N.V. Giai and H. Sagawa, Phys. Lett. B **106**, 379 (1981).

[120] Q.B. Shen, Y.L. Han and H.R. Guo, Phys. Rev. C **80**, 024604 (2009).

[121] M.J. Giannoni and P. Quentim, Phys. Rev. C **21**, 2076 (1980).

[122] C.J. Pethick, D.G. Ravenhall and C.P. Lorenz, Nucl. Phys. A **584**, 675 (1995).

[123] H.S. Köhler, Nucl. Phys. A **258**, 301 (1976).

[124] P.G. Reinhard and H. Flocard, Nucl. Phys. A **584**, 467 (1995).

[125] H. Krivine, J. Treiner and O. Bohigas, Nucl. Phys. A **336**, 155 (1980).

[126] L. Bennour *et al.*, Phys. Rev. C **40**, 2834 (1989).

[127] E. Chabanat, P. Bonche, P. Haensel, J. Meyer and R. Schaeffer, Nucl. Phys. A **635**, 231 (1998).

[128] E. Chabanat, P. Bonche, P. Haensel, J. Meyer and R. Schaeffer, Nucl. Phys. A **627**, 710 (1997).

[129] J.M.G. Gómez, C. Prieto and J. Navarro, Nucl. Phys. A **549**, 125 (1992).

[130] B. Alex Brown, Phys. Rev. C **58**, 220 (1998).

[131] B. Alex Brown *et al.*, Phys. Rev. C **76**, 034305 (2007).

[132] J. Friedrich and P.G. Reinhard, Phys. Rev. C **33**, 335 (1986).

[133] P. Klüpfel, P.G. Reinhard, T.J. Bürvenich and J.A. Maruhn, Phys. Rev. C **79**, 034310 (2009).

[134] F. Tondeur, M. Brack, M. Farine and J.M. Pearson, Nucl. Phys. A **420**, 297 (1984).

[135] J.M. Pearson *et al.*, Nucl. Phys. A **528**, 1 (1991).

[136] Y. Aboussir, J.M. Pearson, A.K. Dutta and F. Tondeur, Nucl. Phys. A **549**, 155 (1992).

[137] M. Onsi, H. Przysiezniak and J.M. Pearson, Phys. Rev. C **50**, 460 (1994).

[138] R.C. Nayak and J.M. Pearson, Phys. Rev. C **52**, 2254 (1995).

[139] J.M. Pearson and R.C. Nayak, Nucl. Phys. A **668**, 163 (2000).

[140] J.M. Pearson and S. Goriely, Phys. Rev. C **64**, 027301 (2001).

[141] S. Goriely, N. Chamel, and J.M. Pearson, Phys. Rev. C **88**, 061302(R) (2013).

[142] J. Margueron, J. Navarro and Nguyen Van Giai, Phys. Rev. C **66**, 014303 (2002).

[143] J.R. Stone, P.A.M. Guichon, H.H. Matevosyan and A.W. Thomas, Nucl. Phys. A **792**, 341 (2007).

[144] Q.N. Usmani, N. Abdullah, K. Anwar and Z. Sauli, Phys. Rev. C **84**, 064313 (2011).

[145] A. Bonasera and M. Di Toro, Lettere Al Nuovo Cimento **44**, 172 (1985).

[146] C.F.V. Weizsäcker, Z. Phys. **96**, 431 (1935).

[147] G. Giuliani, H. Zheng and A. Bonasera, Progress in Particle and Nuclear Physics **76**, 116 (2014).

[148] R. Machleidt, K. Holinde and C. Elster, Phys. Rep. **149**, 1 (1987).

[149] R. Machleidt, Phys. Rev. C **63**, 024001 (2001).

[150] W.N. Cottingham *et al.*, Phys. Rev. D **8**, 800 (1973).

[151] M. Lacombe, B. Loiseau, J.M. Richard and R.V. Mau, Phys. Rev. C **21**, 861 (1980).

[152] R.B. Wiringa, R.A. Smith and T.L. Ainsworth, Phys. Rev. C **29**, 1207 (1984).

[153] R.B. Wiringa, V.G.J. Stoks and R. Schiavilla, Phys. Rev. C **51**, 38 (1995).

[154] C. Gale, G. Bertsch and S. Das Gupta, Phys. Rev. C **35**, 1666 (1987).

[155] J. Rizzo, M. colonna, M. Di Toro and V. Greco, Nucl. Phys. A **732**, 202 (2004).

[156] J. Dechargé and D. Gogny, Phys. Rev. C **21**, 1568 (1980).

[157] C. Gale, G.M. Welke, M. Prakash, S.J. Lee and S. Das Gupta, Phys. Rev. C **41**, 1545 (1990).

[158] C.B. Das, S. Das Gupta, C. Gale and B.A. Li, Phys. Rev. C **67**, 034611 (2003).

[159] M. Prakash *et al.*, Phys. Rep. **280**, 1 (1997).

[160] W. Zuo, U. Lombardo, H.J. Schulze and Z.H. Li, Phys. Rev. C **74**, 014317 (2006).

[161] B.A. Li, C.B. Das, S. Das Gupta and C. Gale, Nucl. Phys. A **735**, 563 (2004).

[162] B. Liu, V. Greco, V. Baran, M. Colonna and M. Di Toro, Phys. Rev. C **65**, 045201 (2002).

[163] E.N.E. van Dalen, C. Fuchs and A. Faessler, Phys. Rev. Lett. **95**, 022302 (2005).

[164] E.N.E. van Dalen, C. Fuchs and A. Faessler, Phys. Rev. C **72**, 065803 (2005).

[165] W.J. Xie, J. Su, L. Zhu and F.S. Zhang, Phys. Rev. C **88**, 061601(R) (2013).

[166] M.D. Youngs, Ph.D. Dissertation, Michigan State University, 2013.

[167] D. Coupland, Ph.D. Dissertation, Michigan State University, 2013.

[168] Y.J. Zhang, R.K. Su, H.Q. Song and F.M. Lin, Phys. Rev. C **54**, 1137 (1996).

[169] E.A. Guggenheim, J. Chem. Phys. **13**, 253 (1945).

[170] J. Xu, L.W. Chen, B.A. Li and H.R. Ma, Phys. Rev. C **77**, 014302 (2008).

[171] J. Mabiala *et al.*, Int. J. Mod. Phys. E **22**, No.12, 1 (2013).

[172] L.G. Moretto, J.B. Elliott, L. Phair and P.T. Lake, J. Phys. G: Nucl. Part. Phys. **38**, 113101 (2011).

[173] J.B. Elliott, P.T. Lake, L.G. Moretto and L. Phair, Phys. Rev. C **87**, 054622 (2013).

[174] J.B. Elliott *et al.*, Phys. Rev. C **67**, 024609 (2003).

[175] P. Finocchiaro *et al.*, Nucl. Phys. A **600**, 236 (1996).

[176] M. Huang *et al.*, Phys. Rev. C **81**, 044618 (2010).

[177] A.Z. Mekjian, S.J. Lee and L. Zamick, Phys. Rev. C **72**, 044305 (2005).

[178] J. Tõke, J. Lu and W. Udo Schröder, Phys. Rev. C **67**, 044307 (2003).

[179] A. Bonasera, V. Latora and A. Rapisarda, Phys. Rev. Lett. **75**, 3434 (1995).

[180] A. Bonasera, *Physics World Archive*, page 20, 1999.

[181] J.B. Natowitz *et al.*, Phys. Rev. C **65**, 034618 (2002).

[182] J.B. Natowitz *et al.*, Int. J. Mod. Phys. E **13**, 269 (2004).

[183] H.R. Jaqaman, A.Z. Mekjian and L. Zamick, Phys. Rev. C **29**, 2067 (1984).

[184] D.L. Hill and J.A. Wheeler, Phys. Rev. **89**, 1102 (1953).

[185] S. Wilke, Phys. Lett. A **96**, 344 (1983).

[186] D. Stauffer, Phys. Rep. **54**, 1 (1979).

[187] J.B. Elliot *et al.*, Phys. Rev. C **49**, 3185 (1994).

[188] L. Phair *et al.*, Phys. Lett. B **285**, 10 (1992).

[189] T. Furuta and A. Ono, Phys. Rev. C **74**, 014612 (2006).

[190] T.J. Schlagel and V.R. Pandharipande, Phys. Rev. C **36**, 162 (1987).

[191] M. Belkacem, V. Latora and A. Bonasera, Phys. Lett. B **326**, 21 (1994).

[192] R.C. Tolman, Phys. Rev. **55**, 364 (1939).

[193] J.R. Oppenheimer and G.M. Volkoff, Phys. Rev. **55**, 374 (1939).

[194] I. Sagert, M. Hempel, C. Greiner and J. Schaffner Bielich, Eur. J. Phys. **27**, 577 (2006).

[195] J.P.W Diener, Master thesis, Stellenbosch University, 2008.

[196] E. Egeland, Master thesis, Norwegian University, 2007.

[197] O.M. Zubairi, Master thesis, San Diego State University, 2010.

[198] T. Endo, T. Maruyama, S. Chiba and T. Tatsumi, Progress of Theoretical Physics **115**, 2 (2006).

[199] N. Yasutake, T. Maruyama and T. Tatsumi, Phys. Rev. D **86**, 101302(R) (2012).

[200] G. Pagliara, M. Hempel and J. Schaffner-Bielich, Phys. Rev. Lett. **103**, 171102 (2009).

[201] R. Cavagnoli, D.P. Menezes and C. Providência, Phys. Rev. C **83**, 065810 (2011).

[202] J.P. Bondorf *et al.*, Phys. Rep. **257**, 133 (1995).

[203] W. Bauer, G.F. Bertsch and S. Das Gupta, Phys. Rev. Lett. **58**, 863 (1987).

[204] C. Grégoire, B. Rémaud, F. Sébille, L. Vinet and Y. Raffray, Nucl. Phys. A **465**, 317 (1987).

[205] L. Vinet, C. Grégoire, P. Schuck, B. Rémaud, and F. Sébille, Nucl. Phys. A **468**, 321 (1987).

[206] B. Friedman and V.R. Pandharipande, Nucl. Phys. A **361**, 502 (1981).

[207] P. Danielewicz, Ann. Phys **197**, 154 (1990).

[208] C.W. Johnson, S.E. Koonin, G.H. Lang and W.E. Ormand, Phys. Rev. Lett. **69**, 3157 (1992).

[209] B.A. Brown, B.H. Wildenthal, Ann. Rev. Nucl. Part. Sci. **38**, 29 (1988).

[210] B.A. Brown, Progress in Particle and Nuclear Physics **47**, 517 (2001).

[211] J. Dukelsky, G. Röpke and P. Schuck, Nucl. Phys. A **628**, 17 (1998).

[212] J.P. Jeukenne, A. Lejeune and C. Mahaux, Phys. Rep. **25**, 83 (1976).

[213] I. Bombaci and U. Lombardo, Phys. Rev. C **44**, 1892 (1991).

[214] W. Zuo, I. Bombaci and U. Lombardo, Phys. Rev. C **60**, 024605 (1999).

[215] A.S. Umar and V.E. Oberacker, Phys. Rev. C **73**, 054607 (2006).

[216] A.S. Umar and V.E. Oberacker, Phys. Rev. C **74**, 024606 (2006).

[217] A. Bonasera, V.N. Kondratyev, A. Smerzi and E.A. Remler, Phys. Rev. Lett. **71**, 505 (1993).

[218] C.Y. Wong and H.H.K. Tang, Phys. Rev. Lett. **40**, 1070 (1978).

[219] C.Y. Wong and H.H.K. Tang, Phys. Rev. C **20**, 1419 (1979).

[220] C.Y. Wong, Phys. Rev. C **25**, 1460 (1982).

[221] C.Y. Wong and K.T.R. Davies, Phys. Rev. C **28**, 240 (1983).

[222] H. Kruse, B.V. Jacak and H. Stöcker, Phys. Rev. Lett. **54**, 289 (1985).

[223] H. Kruse, B.V. Jacak, J.J. Molitoris, G.D. Westfall and H. Stöcker, Phys. Rev. C **31**, 1770 (1985).

[224] J.J. Molitoris, H. Stöcker and B.L. Winer, Phys. Rev. C **36**, 220 (1987).

[225] A. Bonasera, G.F. Burgio and M. Di Toro, Phys. Lett. B **221**, 223 (1989).

[226] A. Bonasera, M. Di Toro and F. Gulminelli, Phys. Rev. C **42**, 966 (1990).

[227] A. Bonasera and F. Gulminelli, Phys. Lett. B **259**, 399 (1991).

[228] A. Bonasera and F. Gulminelli, Phys. Lett. B **275**, 24 (1992).

[229] J. Aichelin and H. Stöcker, Phys. Lett. B **176**, 14 (1986).

[230] S.W. Huang *et al.*, Progress in Particle and Nuclear Physics **30**, 105 (1993).

[231] E. Lehmann *et al.*, Progress in Particle and Nuclear Physics **30**, 219 (1993).

[232] Ph. Chomaz, G.F. Burgio and J. Randrup, Phys. Lett. B **254**, 340 (1991).

[233] M. Colonna, G.F. Burgio, Ph. Chomaz, M. Di Toro and J. Randrup, Phys. Rev. C **47**, 1395 (1993).

[234] J.P. Bondorf *et al.*, Nucl. Phys. A **443**, 321 (1985).

[235] J.P. Bondorf, R. Donangelo, I.N. Mishustin and H. Schulz, Nucl. Phys. A **444**, 460 (1985).

[236] http://www.chemistry.wustl.edu/∼rc/gemini++/gemini.pdf

[237] D.H.E. Gross, Rep. Prog. Phys. **53**, 605 (1990).

[238] A.R. Bodmer, C.N. Panos and A.D. Mackellar, Phys. Rev. C **22**, 1025 (1980).

[239] R.J. Lenk and V.R. Pandharipande, Phys. Rev. C **39**, 2242 (1989).

[240] L.D. Landau and E.M. Lifshitz, *Physical Kinetics,* 1st ed. (Pergamon Press Ltd, 1981).

[241] C. Dorso and J. Randrup, Phys. Lett. B **301**, 328 (1993).

[242] C. Dorso, S. Duarte and J. Randrup, Phys. Lett. B **188**, 287 (1987).

[243] M. Papa, T. Maruyama and A. Bonasera, Phys. Rev. C **64**, 024612 (2001).

[244] H. Feldmeier, K. Bieler and J. Schnack, Nucl. Phys. A **586**, 493 (1995).

[245] J. Schnack and H. Feldmeier, Phys. Lett. B **409**, 6 (1997).

[246] H. Feldmeier and J. Schnack, Progress in Particle and Nuclear Physics **39**, 393 (1997).

[247] H. Feldmeier and J. Schnack, Rev. Mod. Phys. **72**, 655 (2000).

[248] T. Neff and H. Feldmeier, Nucl. Phys. A **738**, 357 (2004).

[249] H. Feldmeier and T. Neff, arXiv: 1307.6449v1.

[250] A. Bonasera, Phys. Rev. C **62**, 052202(R) (2000).

[251] A. Bonasera, Nucl. Phys. A **681**, 64c (2001).

[252] S. Terranova and A. Bonasera, Phys. Rev. C **70**, 024906 (2004).

[253] S. Terranova, D.M. Zhou and A. Bonasera, Eur. Phys. J. A **26**, 333 (2005).

[254] A. Raphelt, Master thesis, Texas A&M University, 2014.

[255] G.A. Souliotis, National and Kapodistrian University of Athens, private communication.

[256] A. Bonasera, T. Maruyama, Progress of Theoretical Physics **90**, 12 (1993).

[257] Z.G. Tan *et al.*, Int. J. Mod. Phys. E **16**, 2269 (2007).

[258] S. Wuenschel *et al.*, Nucl. Phys. A **843**, 1 (2010).

[259] A. Kelić, J.B. Natowitz and K.H. Schmidt, Eur. Phys. J. A **30**, 203 (2006).

[260] S. Albergo, S. Costa, E. Costanzo and A. Rubbino, Nuovo Cimento A **89**, 1 (1985).

[261] H. Xi *et al.*, Phys. Lett. B **431**, 8 (1998).

[262] H. Xi, W.G. Lynch, M.B. Tsang, W.A. Friedman and D. Durand, Phys. Rev. C **59**, 1567 (1999).

[263] Z. Majka, P. Staszel, J. Cibor, J.B. Natowitz, K. Hagel, J. Li, N. Mdeiwayeh, R. Wada and Y. Zhao, Phys. Rev. C **55**, 2991 (1997).

[264] S. Kowalski *et al.*, Phys. Rev. C **75**, 014601 (2007).

[265] J. Sun, L. Zhu, W.J. Xie and F.S. Zhang, Phys. Rev. C **85**, 017604 (2012).

[266] K. Hagel *et al.*, Phys. Rev. Lett. **108**, 062702 (2012).

[267] R. Wada *et al.*, Phys. Rev. C **85**, 064618 (2012).

[268] G. Röpke *et al.*, Phys. Rev. C **88**, 024609 (2013).

[269] A. Mekjian, Phys. Rev. Lett. **38**, 640 (1977).

[270] A. Mekjian, Phys. Rev. C **17**, 1051 (1978).

[271] T.C. Awes *et al.*, Phys. Rev. C **24**, 89 (1981).

[272] V. Greco, C.M. Ko and R. Rapp, Phys. Lett. B **595**, 202 (2004).

[273] The STAR Collaboration, Nature **473**, 353 (2011).

[274] L. Qin *et al.*, Phys. Rev. Lett. **108**, 172701 (2012).

[275] K. Hagel *et al.*, Phys. Rev. C **62**, 034607 (2000).

[276] H. Sato and K. Yazaki, Phys. Lett. B **98**, 153 (1981).

[277] M.B. Tsang, W.G. Lynch, H. Xi and W.A. Friedman, Phys. Rev. Lett. **78**, 3836 (1997).

[278] S. Pratt and M.B. Tsang, Phys. Rev. C **36**, 2390 (1987).

[279] W.G. Gong, W. Bauer, C.K. Gelbke and S. Pratt, Phys. Rev. C **43**, 781 (1991).

[280] D.O. Handzy *et al.*, Phys. Rev. C **51**, 2237 (1995).

[281] S. Shlomo and J.B. Natowitz, Phys. Rev. C **44**, 2878 (1991).

[282] T. Kubo, M. Belkacem, V. Latora and A. Bonasera, Z. Phys. A **352**, 145 (1995).

[283] H. Zheng and A. Bonasera, Phys. Lett. B **696**, 178 (2011).

[284] H. Zheng and A. Bonasera, Phys. Rev. C **86**, 027602 (2012).

[285] H. Zheng, G. Giuliani and A. Bonasera, J. Phys. G: Nucl. Part. Phys. **41**, 055109 (2014).

[286] H. Zheng, G. Giuliani and A. Bonasera, Nucl. Phys. A **892**, 43 (2012).

[287] W.H. Dickhoff, A. Faessler, J. Meyer-ter-Vehn and H. Müther, Phys. Rev. C **23**, 1154 (1981).

[288] F. Hoyle, Astrophys. J. Suppl. Ser. **1**, 121 (1954).

[289] M. Chernykh *et al.*, Phys. Rev. Lett. **98**, 032501 (2007).

[290] M. Hjorth-Jensen, Physics **4**, 38 (2011).

[291] E. Epelbaum, H. Krebs, D. Lee and U. Meiβner, Phys. Rev. Lett. **106**, 192501 (2011).

[292] K. Hagel *et al.*, Phys. Rev. Lett. **68**, 2141 (1992).

[293] K. Hagel *et al.*, Phys. Rev. C **50**, 2017 (1994).

[294] D.H.E. Gross, Phys. Rep. **279**, 119 (1997).

[295] J.B. Natowitz *et al.,* Phys. Rev. Lett. **104**, 202501 (2010).

[296] W. Bauer, Phys. Rev. C **51**, 803 (1995).

[297] M. D'Agostino *et al.*, Nucl. Phys. A **650**, 329 (1999).

[298] J. Pochodzalla *et al.*, Phys. Rev. Lett. **75**, 1040 (1995).

[299] A. Bonasera *et al.*, Phys. Rev. Lett. **101**, 122702 (2008).

[300] M. Huang *et al.*, Nucl. Phys. A **847**, 233 (2010).

[301] B. Borderie *et al.*, Phys. Lett. B **723**, 140 (2013).

[302] S. Piantelli *et al.*, Nucl. Phys. A **809**, 111 (2008).

[303] B. Borderie and M.F. Rivet, Progress in Particle and Nuclear Physics **61**, 551 (2008).

[304] P.J. Siemens and J.I. Kapusta, Phys. Rev. Lett. **43**, 1486 (1979).

[305] P. Bonche, S. Levit and D. Vautherin, Nucl. Phys. A **436**, 265 (1985).

[306] K. Binder, Rep. Prog. Phys. **50**, 783 (1987).

[307] F. Gulminelli, Ph. Chomaz, Al.H. Raduta and Ad.R. Raduta, Phys. Rev. Lett. **91**, 202701 (2003).

[308] Ad.R. Raduta and F. Gulminelli, Phys. Rev. C **75**, 044605 (2007).

[309] L.G. Moretto, J.B. Elliott and L. Phair, Phys. Rev. C **68**, 061602 (2003).

[310] D. Lacroix and Ph. Chomaz, Nucl. Phys. A **636**, 85 (1998).

[311] D. Arnett, Supernovae and Nucleosynthesis, Princeton University Press, 1996.

[312] K. Schmidt *et al.*, Journal of Physics: Conference Series **420**, 012088 (2013).

[313] A.G. Truscott *et al.*, Science **291**, 2570 (2001).

[314] F. Schreck *et al.*, Phys. Rev. Lett. **87**, 080403 (2001).

[315] G. Modugno *et al.*, Science **297**, 2240 (2002).

[316] Z. Hadzibabic *et al.*, Phys. Rev. Lett. **88**, 160401 (2002).

[317] G. Roati *et al.*, Phys. Rev. Lett. **89**, 150403 (2002).

[318] C. Ospelkaus *et al.*, Phys. Rev. Lett. **96**, 020104 (2006).

[319] B.C. Stein *et al.*, J. Phys. G: Nucl. Part. Phys. **41**, 025108 (2014).

[320] P. Grüter, D. Ceperley and F. Laloë, Phys. Rev. Lett. **79**, 3549 (1997).

[321] T.D. Lee and C.N. Yang, Phys. Rev. **105**, 1119 (1957).

[322] T.D. Lee, K. Huang and C.N. Yang, Phys. Rev. **106**, 1135 (1957).

[323] J. Manfredi *et al.*, Phys. Rev. C **85**, 037603 (2012).

[324] P. Marini *et al.*, in preparation.

APPENDIX A

FREE FERMI GAS AT $T = 0$

From [1, 7, 51], we know the distribution function of free Fermi gas at $T = 0$ is

$$f(p) = \begin{cases} 1, & p \leq p_f, \\ 0, & p > p_f, \end{cases} \tag{A.1}$$

where p_f is Fermi momentum. Then the average multiplicity is

$$\begin{aligned} N &= \frac{g}{h^3} \int f(p) d^3x d^3p \\ &= \frac{g}{8\pi^3\hbar^3} 4\pi V \int_0^{p_f} p^2 dp \\ &= \frac{gV}{6\pi^2\hbar^3} p_f^3, \end{aligned} \tag{A.2}$$

where g is the degeneracy of the free Fermi gas and $\hbar = \frac{h}{2\pi}$ is the reduced Planck constant. Thus density of the free Fermi gas is

$$\rho = \frac{N}{V} = \frac{g}{6\pi^2\hbar^3} p_f^3. \tag{A.3}$$

From Eq. (A.3), one can obtain the Fermi momentum p_f as a function of density

$$p_f = \left(\frac{6\pi^2\hbar^3}{g} \rho \right)^{1/3}. \tag{A.4}$$

A.1 Energy per Particle, Pressure, Incompressibility and Speed of Sound of Free Fermi Gas at $T = 0$

Using Eqs. (1.7, 1.10, 1.16, 1.17), we can calculate the pressure, the incompressibility and the speed of sound of free Fermi gas if we know the equation of energy per particle. The energy per particle can be a function of density ρ or Fermi momentum p_f. In the following, we will calculate the energy per particle first, then we calculate the pressure, the incompressibility and the speed of sound.

A.1.1 Non-relativistic Free Fermi Gas

For the non-relativistic free Fermi gas, the energy of particle with momentum p is

$$\varepsilon(p) = \frac{p^2}{2m}. \tag{A.5}$$

The total energy of the non-relativistic free Fermi gas is

$$\begin{aligned} E &= \frac{g}{h^3}\int \varepsilon(p) f(p) d^3x d^3p \\ &= \frac{g}{h^3}\int \frac{p^2}{2m} f(p) d^3x d^3p \\ &= \frac{g}{8\pi^3\hbar^3} 4\pi V \int_0^{p_f} \frac{p^4}{2m} dp \\ &= \frac{gV}{10\pi^2\hbar^3}\frac{p_f^5}{2m}. \end{aligned} \tag{A.6}$$

The energy per particle of the non-relativistic free Fermi gas is

$$\begin{aligned} (E/A)_{nonrel} &= \frac{E}{N} \\ &= \frac{\frac{gV}{10\pi^2\hbar^3}\frac{p_f^5}{2m}}{\frac{gV}{6\pi^2\hbar^3}p_f^3} \\ &= \frac{3}{5}\frac{p_f^2}{2m}. \end{aligned} \tag{A.7}$$

We have used Eq. (A.3). Notice that the energy per particle doesn't depend on the particle degeneracy.

Considering the non-relativistic free Fermi gas is the mixture of protons and neutrons and $N = Z$, therefore $g = 4, m = 938.6$ MeV. The energy per particle at density ρ is

$$\begin{aligned}
(E/A)_{nonrel} &= \frac{3}{5}\frac{p_f^2}{2m} \\
&= \frac{3}{5}\frac{1}{2m}(\frac{6\pi^2\hbar^3\rho}{g})^{2/3} \\
&= \frac{3}{5}\frac{\hbar^2}{2m}(\frac{6\pi^2\rho_0}{g})^{2/3}\tilde{\rho}^{\frac{2}{3}} \\
&= \bar{\varepsilon}_{f0}\tilde{\rho}^{\frac{2}{3}}, \qquad \text{(A.8)}
\end{aligned}$$

where the average Fermi energy $\bar{\varepsilon}_{f0} = \frac{3}{5}\frac{\hbar^2}{2m}(\frac{6\pi^2\rho_0}{g})^{2/3} = 22.5$ MeV, $\rho_0 = 0.165$ fm^{-3} and the reduced density $\tilde{\rho} = \frac{\rho}{\rho_0}$.

The pressure is

$$\begin{aligned}
P &= \rho^2\frac{\partial(E/A)_{nonrel}}{\partial\rho} \\
&= \frac{2}{3}\rho_0\bar{\varepsilon}_{f0}\tilde{\rho}^{\frac{5}{3}}. \qquad \text{(A.9)}
\end{aligned}$$

The incompressibility is

$$\begin{aligned}
K &= 9\frac{\partial P}{\partial\rho}\Big|_{\rho=\rho_0} \\
&= 9\times\frac{2}{3}\times\frac{5}{3}\bar{\varepsilon}_{f0}\tilde{\rho}^{\frac{2}{3}}\Big|_{\rho=\rho_0} \\
&= 10\bar{\varepsilon}_{f0}\tilde{\rho}^{\frac{2}{3}}\Big|_{\rho=\rho_0}. \qquad \text{(A.10)}
\end{aligned}$$

The speed of sound is

$$\begin{aligned}\frac{v}{c} &= \sqrt{\frac{1}{\frac{\partial[\rho(E/A)_{nonrel}]}{\partial\rho}+m}\frac{\partial P}{\partial\rho}} \\ &= \sqrt{\frac{\frac{10}{9}\bar{\varepsilon}_{f0}\tilde{\rho}^{\frac{2}{3}}}{\frac{5}{3}\bar{\varepsilon}_{f0}\tilde{\rho}^{\frac{2}{3}}+m}}. \end{aligned} \tag{A.11}$$

We can see that the speed of sound will be larger than 1 when ρ is large enough for the non-relativistic free Fermi gas.

A.1.2 Relativistic Free Fermi Gas

For the relativistic free Fermi gas, the energy of particle with momentum p is

$$\varepsilon(p) = \sqrt{p^2+m^2}. \tag{A.12}$$

The total energy of the relativistic Fermi gas is

$$\begin{aligned} E &= \frac{g}{h^3}\int \varepsilon(p) f(p) d^3x d^3p \\ &= \frac{g}{h^3}\int \sqrt{p^2+m^2} f(p) d^3x d^3p \\ &= \frac{g}{8\pi^3\hbar^3} 4\pi V \int_0^{p_f} \sqrt{p^2+m^2} p^2 dp \\ &= \frac{gV}{16\pi^2\hbar^3}[p_f\sqrt{p_f^2+m^2}(m^2+2p_f^2) - m^4 \ln\frac{p_f+\sqrt{p_f^2+m^2}}{m}]. \end{aligned} \tag{A.13}$$

The energy per particle of the relativistic free Fermi gas is

$$\begin{aligned}(E/A)_{rel} &= \frac{E}{N} \\ &= \frac{\frac{gV}{16\pi^2\hbar^3}[p_f\sqrt{p_f^2+m^2}(m^2+2p_f^2) - m^4\ln\frac{p_f+\sqrt{p_f^2+m^2}}{m}]}{\frac{gV}{6\pi^2\hbar^3}p_f^3}\end{aligned}$$

$$= \frac{3}{8}\frac{1}{p_f^3}[p_f\sqrt{p_f^2+m^2}(m^2+2p_f^2) - m^4\ln\frac{p_f+\sqrt{p_f^2+m^2}}{m}]. \quad \text{(A.14)}$$

The pressure is

$$\begin{aligned}
P &= -N\left[\frac{\partial(E/A)_{rel}}{\partial\rho}\frac{\partial\rho}{\partial V}\right]_{S,N} \\
&= -N\left[\frac{\partial(E/A)_{rel}}{\partial p_f}\frac{\partial p_f}{\partial V}\right]_{S,N} \\
&= -N\frac{\frac{3}{8}\frac{-3m^4p_f - m^2p_f^3 + 2p_f^5 + 3m^4\sqrt{m^2+p_f^2}\ln\frac{p_f+\sqrt{m^2+p_f^2}}{m}}{p_f^4\sqrt{m^2+p_f^2}}}{-\frac{3V}{p_f}} \\
&= \frac{1}{8}\rho\frac{-3m^4p_f - m^2p_f^3 + 2p_f^5 + 3m^4\sqrt{m^2+p_f^2}\ln\frac{p_f+\sqrt{m^2+p_f^2}}{m}}{p_f^3\sqrt{m^2+p_f^2}} \\
&= \frac{1}{8}\frac{g}{6\pi^2\hbar^3}\frac{-3m^4p_f - m^2p_f^3 + 2p_f^5 + 3m^4\sqrt{m^2+p_f^2}\ln\frac{p_f+\sqrt{m^2+p_f^2}}{m}}{\sqrt{m^2+p_f^2}} \\
&= \frac{g}{16\pi^2\hbar^3}\frac{p_f(\frac{2}{3}p_f^2 - m^2)(p_f^2+m^2) + m^4\sqrt{m^2+p_f^2}\ln\frac{p_f+\sqrt{m^2+p_f^2}}{m}}{\sqrt{m^2+p_f^2}} \\
&= \frac{g}{16\pi^2\hbar^3}\left[p_f(\frac{2}{3}p_f^2 - m^2)\sqrt{p_f^2+m^2} + m^4\ln\frac{p_f+\sqrt{m^2+p_f^2}}{m}\right]. \quad \text{(A.15)}
\end{aligned}$$

We have used Eq. (A.3). The incompressibility is

$$\begin{aligned}
K &= 9\frac{\partial P}{\partial\rho}\bigg|_{\rho=\rho_0} \\
&= 9\frac{\partial P}{\partial p_f}\Big/\frac{\partial\rho}{\partial p_f}\bigg|_{p_f=p_{f0}} \\
&= 9\frac{\frac{g}{6\pi^2\hbar^3}\frac{p_f^4}{\sqrt{p_f^2+m^2}}}{\frac{g}{6\pi^2\hbar^3}3p_f^2}\bigg|_{p_f=p_{f0}}
\end{aligned}$$

$$= \quad 3\frac{p_f^2}{\sqrt{p_f^2+m^2}}\Bigg|_{p_f=p_{f0}} . \tag{A.16}$$

The energy density is

$$\begin{aligned}
\epsilon &= \rho(E/A)_{rel} \\
&= \frac{3}{8}\rho\frac{1}{p_f^3}\left[p_f\sqrt{p_f^2+m^2}(m^2+2p_f^2) - m^4\ln\frac{p_f+\sqrt{p_f^2+m^2}}{m}\right] \\
&= \frac{3}{8}\frac{g}{6\pi^2\hbar^3}p_f^3\frac{1}{p_f^3}\left[p_f\sqrt{p_f^2+m^2}(m^2+2p_f^2) - m^4\ln\frac{p_f+\sqrt{p_f^2+m^2}}{m}\right] \\
&= \frac{g}{16\pi^2\hbar^3}\left[p_f\sqrt{p_f^2+m^2}(m^2+2p_f^2) - m^4\ln\frac{p_f+\sqrt{p_f^2+m^2}}{m}\right] .
\end{aligned} \tag{A.17}$$

Then we can calculate the speed of sound

$$\begin{aligned}
\frac{v}{c} &= \sqrt{\frac{\partial P}{\partial\epsilon}} \\
&= \sqrt{(\frac{\partial P}{\partial p_f})/(\frac{\partial\epsilon}{\partial p_f})} \\
&= \sqrt{\frac{\frac{g}{6\pi^2\hbar^3}\frac{p_f^4}{\sqrt{p_f^2+m^2}}}{\frac{g}{2\pi^2\hbar^3}p_f^2\sqrt{p_f^2+m^2}}} \\
&= \sqrt{\frac{p_f^2}{3(p_f^2+m^2)}}.
\end{aligned} \tag{A.18}$$

From Eq. (A.18), we can see that the speed of sound of relativistic free Fermi gas is always less than 1.

A.1.3 Ultra-relativistic Free Fermi Gas

For the ultra-relativistic free Fermi gas, the energy of particle with momentum p is

$$\varepsilon(p) = p. \tag{A.19}$$

The total energy of the ultra-relativistic Fermi gas is

$$\begin{aligned} E &= \frac{g}{h^3}\int \varepsilon(p) f(p) d^3x d^3p \\ &= \frac{g}{h^3}\int p f(p) d^3x d^3p \\ &= \frac{g}{8\pi^3\hbar^3} 4\pi V \int_0^{p_f} p^3 dp \\ &= \frac{gV}{8\pi^2\hbar^3} p_f^4. \end{aligned} \tag{A.20}$$

The energy per particle of the ultra-relativistic free Fermi gas is

$$\begin{aligned} (E/A)_{rel} &= \frac{E}{N} \\ &= \frac{\frac{gV}{8\pi^2\hbar^3}p_f^4}{\frac{gV}{6\pi^2\hbar^3}p_f^3} \\ &= \frac{3}{4}p_f. \end{aligned} \tag{A.21}$$

The pressure is

$$\begin{aligned} P &= -N\left[\frac{\partial (E/A)_{rel}}{\partial \rho}\frac{\partial \rho}{\partial V}\right]_{S,N} \\ &= -N\left[\frac{\partial (E/A)_{rel}}{\partial p_f}\frac{\partial p_f}{\partial V}\right]_{S,N} \\ &= -N\frac{\frac{3}{4}}{-\frac{3V}{p_f}} \\ &= \frac{1}{4}\rho p_f \end{aligned}$$

$$= \frac{g}{24\pi^2\hbar^3}p_f^4. \tag{A.22}$$

The incompressibility is

$$\begin{aligned} K &= 9\frac{\partial P}{\partial \rho}\Big|_{\rho=\rho_0} \\ &= 9\frac{\partial P}{\partial p_f}\Big/\frac{\partial \rho}{\partial p_f}\Big|_{p_f=p_{f0}} \\ &= 9\frac{\frac{g}{6\pi^2\hbar^3}p_f^3}{\frac{g}{6\pi^2\hbar^3}3p_f^2}\Big|_{p_f=p_{f0}} \\ &= 3p_f|_{p_f=p_{f0}}. \end{aligned} \tag{A.23}$$

The energy density is

$$\begin{aligned} \epsilon &= \rho(E/A)_{rel} \\ &= \rho\frac{3}{4}p_f \\ &= \frac{g}{6\pi^2\hbar^3}p_f^3 \times \frac{3}{4}p_f \\ &= 3 \times \frac{g}{24\pi^2\hbar^3}p_f^4 \\ &= 3P. \end{aligned} \tag{A.24}$$

Thus we obtain

$$P = \frac{1}{3}\epsilon. \tag{A.25}$$

Therefore, the speed of sound is

$$\frac{v}{c} = \sqrt{\frac{\partial P}{\partial \epsilon}} = \sqrt{\frac{1}{3}}. \tag{A.26}$$

For the ultra-relativistic free Fermi gas, the speed of sound is a constant. Eq. (A.26) is the limit of relativistic free Fermi gas Eq. (A.18) when $p_f >> m$.

APPENDIX B

FREE FERMI GAS AT LOW T

When $T \neq 0$, free Fermi gas satisfies the Fermi-Dirac distribution

$$f(p) = \frac{1}{e^{(\frac{p^2}{2m}-\mu)/T}+1} = \frac{1}{e^{[\varepsilon(p)-\mu]/T}+1}, \tag{B.1}$$

where $\varepsilon(p) = \frac{p^2}{2m}$ is the energy , μ is the chemical potential and T is the temperature of the free Fermi gas. In the following, we use ε instead of $\varepsilon(p)$. We define

$$y \equiv \frac{\varepsilon}{T}, \quad \nu \equiv \frac{\mu}{T}, \quad z \equiv e^{\nu}. \tag{B.2}$$

Then Fermi-Dirac distribution becomes

$$f(p) = \frac{1}{e^{y-\nu}+1} = \frac{1}{z^{-1}e^{y}+1}. \tag{B.3}$$

B.1 The Fermi Integral at Low T

For convenience, we define the Fermi integral

$$f_n(z) \equiv \frac{1}{\Gamma(n)} \int_0^\infty dy \frac{y^{n-1}}{z^{-1}e^{y}+1}, \tag{B.4}$$

or

$$f_n(\nu) \equiv \frac{1}{\Gamma(n)} \int_0^\infty dy \frac{y^{n-1}}{e^{y-\nu}+1}. \tag{B.5}$$

Eqs. (B.4, B.5) have different arguments but they are equivalent. At low T, $\nu = \frac{\mu}{T} >> 1$, from [51] the appendix (E. 15), we know

$$\begin{aligned}
f_n(\nu) &\equiv \frac{1}{\Gamma(n)}\int_0^\infty dy \frac{y^{n-1}}{e^{y-\nu}+1} \\
&= \frac{\nu^n}{\Gamma(n+1)}[1+2n\sum_{j=1,3,5,\cdots}(n-1)(n-2)\cdots(n-j)(1-\frac{1}{2^j})\frac{\zeta(j+1)}{\nu^{j+1}}] \\
&= \frac{\nu^n}{\Gamma(n+1)}[1+2n\sum_{j=1,3,5,\cdots}(n-1)(n-2)\cdots(n-j)(1-\frac{1}{2^j})\frac{\zeta(j+1)}{\nu^{j+1}}] \\
&= \frac{\nu^n}{\Gamma(n+1)}[1+2n(n-1)(1-\frac{1}{2})\frac{\zeta(2)}{\nu^2}+2n(n-1)(n-2)(n-3)(1-\frac{1}{2^3})\frac{\zeta(4)}{\nu^4} \\
&\quad +2n(n-1)(n-2)(n-3)(n-4)(n-5)(1-\frac{1}{2^5})\frac{\zeta(6)}{\nu^6} \\
&\quad +2n(n-1)(n-2)(n-3)(n-4)(n-5)(n-6)(n-7)(1-\frac{1}{2^7})\frac{\zeta(8)}{\nu^8} \\
&\quad +\cdots], \qquad \text{(B.6)}
\end{aligned}$$

where $\zeta(j)$ is zeta function. Once we know n, we can obtain the low temperature expansion of Fermi integral $f_n(\nu)$.

B.2 Chemical Potential of Free Fermi Gas at Low T

B.2.1 The General Integral Transformation

One of the frequently used integrals is

$$FUI(n) = \int_0^\infty dp p^n f(p), \qquad \text{(B.7)}$$

where $f(p)$ is a function of p. Let's make the integral variable transformation,

$$\varepsilon = \frac{p^2}{2m}, \quad p = (2m\varepsilon)^{\frac{1}{2}}, \quad dp = \frac{m}{\sqrt{2m\varepsilon}}d\varepsilon. \qquad \text{(B.8)}$$

Then we obtain

$$\begin{aligned} FUI(n) &= \int_0^\infty d\varepsilon \frac{m}{\sqrt{2m\varepsilon}} (2m\varepsilon)^{\frac{n}{2}} f(p) \\ &= \frac{(2m)^{\frac{n+1}{2}}}{2} \int_0^\infty d\varepsilon \varepsilon^{\frac{n-1}{2}} f(p). \end{aligned} \tag{B.9}$$

Let's make the integral variable transformation again

$$y = \frac{\varepsilon}{T}, \quad d\varepsilon = Tdy, \tag{B.10}$$

which has the same notation in Eq. (B.2). Therefore

$$FUI(n) = \frac{(2mT)^{\frac{n+1}{2}}}{2} \int_0^\infty dy y^{\frac{n-1}{2}} f(p). \tag{B.11}$$

B.2.2 Chemical Potential of Free Fermi Gas at Low T

The average multiplicity of free Fermi gas is

$$\begin{aligned} \bar{N} &= \frac{g}{h^3} \int f(p) d^3x d^3p \\ &= \frac{g}{h^3} \int f(p) d^3x d^3p \\ &= \frac{g}{h^3} 4\pi V \int_0^\infty p^2 f(p) dp \\ &= \frac{g}{h^3} 4\pi V \times FUI(2) \\ &= \frac{g}{h^3} 4\pi V \frac{(2mT)^{\frac{3}{2}}}{2} \int_0^\infty dy y^{\frac{2-1}{2}} \frac{1}{e^{y-\nu}+1} \\ &= \frac{g}{h^3} 4\pi V \frac{(2mT)^{\frac{3}{2}}}{2} \int_0^\infty dy \frac{y^{\frac{3}{2}-1}}{e^{y-\nu}+1} \\ &= V \frac{g}{h^3} (2\pi mT)^{\frac{3}{2}} f_{3/2}(\nu). \end{aligned} \tag{B.12}$$

We have used Eqs. (B.5, B.11) in above calculation. The density of free Fermi gas is

$$\rho = \frac{\bar{N}}{V} = \frac{g}{h^3}(2\pi mT)^{3/2} f_{3/2}(\nu). \tag{B.13}$$

On the other hand, the Fermi energy is

$$\varepsilon_f = \frac{p_f^2}{2m}. \tag{B.14}$$

Substituting Eq. (A.4) into Eq. (B.14), we obtain

$$\varepsilon_f^{3/2} = \frac{h^3}{(2m)^{3/2}} \frac{\rho}{g} \frac{3}{4\pi}. \tag{B.15}$$

Substituting Eq. (B.13) into Eq. (B.15), we obtain

$$\varepsilon_f^{3/2} = \frac{3\sqrt{\pi}}{4} T^{3/2} f_{3/2}(\nu). \tag{B.16}$$

We need to calculate the low temperature expansion of $f_{3/2}(\nu)$. From Eq. (B.2), we have

$$\nu = \frac{\mu}{T} = \ln z, \quad \mu = T \ln z. \tag{B.17}$$

Substituting Eq. (B.17) into Eq. (B.6) when $n = \frac{3}{2}$, we obtain

$$f_{3/2}(\nu) = \frac{4}{3\pi^{1/2}} (\ln z)^{3/2} [1 + \frac{\pi^2}{8} (\ln z)^{-2} + \frac{7\pi^4}{640} (\ln z)^{-4} + \frac{31\pi^6}{3072} (\ln z)^{-6} + \frac{4191\pi^8}{163840} (\ln z)^{-8} + \cdots]. \tag{B.18}$$

Substituting Eq. (B.18) into Eq. (B.16), we obtain

$$\begin{aligned} \varepsilon_f^{3/2} &= (T \ln z)^{3/2} [1 + \frac{\pi^2}{8} (\ln z)^{-2} + \frac{7\pi^4}{640} (\ln z)^{-4} + \frac{31\pi^6}{3072} (\ln z)^{-6} + \frac{4191\pi^8}{163840} (\ln z)^{-8} + \cdots] \\ &= \mu^{3/2} [1 + \frac{\pi^2}{8} (\ln z)^{-2} + \frac{7\pi^4}{640} (\ln z)^{-4} + \frac{31\pi^6}{3072} (\ln z)^{-6} + \frac{4191\pi^8}{163840} (\ln z)^{-8} + \cdots] \end{aligned} \tag{B.19}$$

Therefore the iteration equation for chemical potential at low T is

$$\begin{aligned}\mu &= \varepsilon_f \frac{1}{[1+\frac{\pi^2}{8}(\ln z)^{-2}+\frac{7\pi^4}{640}(\ln z)^{-4}+\frac{31\pi^6}{3072}(\ln z)^{-6}+\frac{4191\pi^8}{163840}(\ln z)^{-8}+\cdots]^{2/3}} \\ &= \varepsilon_f \frac{1}{[1+\frac{\pi^2}{8}(\frac{T}{\mu})^2+\frac{7\pi^4}{640}(\frac{T}{\mu})^4+\frac{31\pi^6}{3072}(\frac{T}{\mu})^6+\frac{4191\pi^8}{163840}(\frac{T}{\mu})^8+\cdots]^{2/3}}. \end{aligned} \tag{B.20}$$

We process the iteration and obtain

$$\mu_{(0)} = \varepsilon_f, \quad \frac{T}{\mu_{(0)}} = \frac{T}{\varepsilon_f}, \tag{B.21}$$

$$\mu_{(1)} = \varepsilon_f[1-\frac{\pi^2}{12}(\frac{T}{\varepsilon_f})^2], \quad \frac{T}{\mu_{(1)}} = \frac{\frac{T}{\varepsilon_f}}{1-\frac{\pi^2}{12}(\frac{T}{\varepsilon_f})^2}, \tag{B.22}$$

$$\mu_{(2)} = \varepsilon_f[1-\frac{\pi^2}{12}(\frac{T}{\varepsilon_f})^2-\frac{\pi^4}{80}(\frac{T}{\varepsilon_f})^4], \quad \frac{T}{\mu_{(2)}} = \frac{\frac{T}{\varepsilon_f}}{1-\frac{\pi^2}{12}(\frac{T}{\varepsilon_f})^2-\frac{\pi^4}{80}(\frac{T}{\varepsilon_f})^4}, \tag{B.23}$$

$$\mu_{(3)} = \varepsilon_f[1-\frac{\pi^2}{12}(\frac{T}{\varepsilon_f})^2-\frac{\pi^4}{80}(\frac{T}{\varepsilon_f})^4-\frac{247\pi^6}{25920}(\frac{T}{\varepsilon_f})^6], \quad \frac{T}{\mu_{(3)}} = \frac{\frac{T}{\varepsilon_f}}{1-\frac{\pi^2}{12}(\frac{T}{\varepsilon_f})^2-\frac{\pi^4}{80}(\frac{T}{\varepsilon_f})^4-\frac{247\pi^6}{25920}(\frac{T}{\varepsilon_f})^6}. \tag{B.24}$$

B.3 Multiplicity and Quadrupole Momentum Fluctuations of Free Fermi Gas at Low T

In this section, we will derive the low temperature expansion formulas for multiplicity and quadrupole momentum fluctuations of free Fermi gas.

B.3.1 Expansion of ν^n at Low T

From section B.2.2, we know the chemical potential of free Fermi gas at low temperature is

$$\mu = \varepsilon_f[1-\frac{1}{12}\pi^2(\frac{T}{\varepsilon_f})^2-\frac{1}{80}\pi^4(\frac{T}{\varepsilon_f})^4+O(\frac{T}{\varepsilon_f})^6], \tag{B.25}$$

where T is the temperature and ε_f is the Fermi energy. We stop the expansion at $O(\frac{T}{\varepsilon_f})^6$. Therefore,

$$\nu = \frac{\mu}{T} = \frac{\varepsilon_f}{T}[1 - \frac{1}{12}\pi^2(\frac{T}{\varepsilon_f})^2 - \frac{1}{80}\pi^4(\frac{T}{\varepsilon_f})^4 + O(\frac{T}{\varepsilon_f})^6]. \tag{B.26}$$

We do several expansions for ν^n with different power n which we will use later,

$$\nu^{\frac{7}{2}} = (\frac{\varepsilon_f}{T})^{\frac{7}{2}}[1 - \frac{7}{24}\pi^2(\frac{T}{\varepsilon_f})^2 - \frac{77}{5760}\pi^4(\frac{T}{\varepsilon_f})^4 + O(\frac{T}{\varepsilon_f})^6], \tag{B.27}$$

$$\nu^{\frac{5}{2}} = (\frac{\varepsilon_f}{T})^{\frac{5}{2}}[1 - \frac{5}{24}\pi^2(\frac{T}{\varepsilon_f})^2 - \frac{7}{384}\pi^4(\frac{T}{\varepsilon_f})^4 + O(\frac{T}{\varepsilon_f})^6], \tag{B.28}$$

$$\nu^{\frac{3}{2}} = (\frac{\varepsilon_f}{T})^{\frac{3}{2}}[1 - \frac{1}{8}\pi^2(\frac{T}{\varepsilon_f})^2 - \frac{31}{1920}\pi^4(\frac{T}{\varepsilon_f})^4 + O(\frac{T}{\varepsilon_f})^6], \tag{B.29}$$

$$\nu^{\frac{1}{2}} = (\frac{\varepsilon_f}{T})^{\frac{1}{2}}[1 - \frac{1}{24}\pi^2(\frac{T}{\varepsilon_f})^2 - \frac{41}{5760}\pi^4(\frac{T}{\varepsilon_f})^4 + O(\frac{T}{\varepsilon_f})^6], \tag{B.30}$$

$$\nu^{-\frac{1}{2}} = (\frac{\varepsilon_f}{T})^{-\frac{1}{2}}[1 + \frac{1}{24}\pi^2(\frac{T}{\varepsilon_f})^2 + \frac{17}{1920}\pi^4(\frac{T}{\varepsilon_f})^4 + O(\frac{T}{\varepsilon_f})^6], \tag{B.31}$$

$$\nu^{-\frac{3}{2}} = (\frac{\varepsilon_f}{T})^{-\frac{3}{2}}[1 + \frac{1}{8}\pi^2(\frac{T}{\varepsilon_f})^2 + \frac{61}{1920}\pi^4(\frac{T}{\varepsilon_f})^4 + O(\frac{T}{\varepsilon_f})^6], \tag{B.32}$$

$$\nu^{-\frac{5}{2}} = (\frac{\varepsilon_f}{T})^{-\frac{5}{2}}[1 + \frac{5}{24}\pi^2(\frac{T}{\varepsilon_f})^2 + \frac{71}{1152}\pi^4(\frac{T}{\varepsilon_f})^4 + O(\frac{T}{\varepsilon_f})^6], \tag{B.33}$$

$$\nu^{-\frac{7}{2}} = (\frac{\varepsilon_f}{T})^{-\frac{7}{2}}[1 + \frac{7}{24}\pi^2(\frac{T}{\varepsilon_f})^2 + \frac{63}{640}\pi^4(\frac{T}{\varepsilon_f})^4 + O(\frac{T}{\varepsilon_f})^6]. \tag{B.34}$$

B.3.2 Multiplicity Fluctuation

From Eq. (B.12), we know the average multiplicity of free Fermi gas is

$$\bar{N} = V\frac{g}{h^3}(2\pi mT)^{\frac{3}{2}}f_{3/2}(\nu). \tag{B.35}$$

Using Eqs. (B.17, B.18), we obtain

$$\begin{aligned}\bar{N} &= V\frac{g}{h^3}(2\pi mT)^{\frac{3}{2}}\frac{4}{3\pi^{1/2}}(\ln z)^{3/2}[1+\frac{\pi^2}{8}(\ln z)^{-2}+\frac{7\pi^4}{640}(\ln z)^{-4}+\cdots] \\ &= V\frac{g}{h^3}(2mT)^{\frac{3}{2}}\frac{4\pi}{3}\left[\nu^{\frac{3}{2}}+\frac{\pi^2}{8}\nu^{-\frac{1}{2}}+\frac{7\pi^4}{640}\nu^{-\frac{5}{2}}+O(\nu^{-\frac{9}{2}})\right]. \qquad \text{(B.36)}\end{aligned}$$

Substituting Eqs. (B.29, B.31, B.33) into Eq. (B.36), we obtain the average multiplicity of free Fermi gas is

$$\begin{aligned}\bar{N} &= V\frac{g}{h^3}(2mT)^{\frac{3}{2}}\frac{4\pi}{3}(\frac{\varepsilon_f}{T})^{\frac{3}{2}} \\ &= \frac{gV}{6\pi^2\hbar^3}p_f^3, \qquad \text{(B.37)}\end{aligned}$$

which is Eq. (A.2).

From [1], we know the multiplicity fluctuation is given by

$$\langle(\Delta N)^2\rangle = T\left(\frac{\partial\bar{N}}{\partial\mu}\right)_{T,V}. \qquad \text{(B.38)}$$

The Eq. (B.38) can be rewritten as

$$\langle(\Delta N)^2\rangle = \left[\frac{\partial\bar{N}}{\partial(\frac{\mu}{T})}\right]_{T,V} = \left(\frac{\partial\bar{N}}{\partial\nu}\right)_{T,V}. \qquad \text{(B.39)}$$

Substituting Eq. (B.36) into Eq. (B.39), we obtain

$$\langle(\Delta N)^2\rangle = V\frac{g}{h^3}(2mT)^{\frac{3}{2}}\frac{4\pi}{3}\left[\frac{3}{2}\nu^{\frac{1}{2}}-\frac{\pi^2}{16}\nu^{-\frac{3}{2}}-\frac{7\pi^4}{256}\nu^{-\frac{7}{2}}+O(\nu^{-\frac{11}{2}})\right]. \qquad \text{(B.40)}$$

Substituting Eqs. (B.30, B.32, B.34) into Eq. (B.40), we obtain the multiplicity

fluctuation of free Fermi gas as function of $\frac{T}{\varepsilon_f}$

$$\langle(\Delta N)^2\rangle = V\frac{g}{h^3}(2mT)^{\frac{3}{2}}\frac{4\pi}{3}(\frac{\varepsilon_f}{T})^{\frac{1}{2}}\left[\frac{3}{2}-\frac{\pi^2}{8}(\frac{T}{\varepsilon_f})^2-\frac{11\pi^4}{240}(\frac{T}{\varepsilon_f})^4+O(\frac{T}{\varepsilon_f})^6\right]. \quad \text{(B.41)}$$

Dividing Eq. (B.41) by Eq. (B.37), we obtain the normalized multiplicity fluctuation of free Fermi gas at low T

$$\begin{aligned}\frac{\langle(\Delta N)^2\rangle}{\bar{N}} &= \frac{V\frac{g}{h^3}(2mT)^{\frac{3}{2}}\frac{4\pi}{3}(\frac{\varepsilon_f}{T})^{\frac{1}{2}}\left[\frac{3}{2}-\frac{\pi^2}{8}(\frac{T}{\varepsilon_f})^2-\frac{11\pi^4}{240}(\frac{T}{\varepsilon_f})^4+O(\frac{T}{\varepsilon_f})^6\right]}{V\frac{g}{h^3}(2mT)^{\frac{3}{2}}\frac{4\pi}{3}(\frac{\varepsilon_f}{T})^{\frac{3}{2}}} \\ &= \frac{T}{\varepsilon_f}\left[\frac{3}{2}-\frac{\pi^2}{8}(\frac{T}{\varepsilon_f})^2-\frac{11\pi^4}{240}(\frac{T}{\varepsilon_f})^4+O(\frac{T}{\varepsilon_f})^6\right] \\ &= \frac{3}{2}\frac{T}{\varepsilon_f}\left[1-\frac{\pi^2}{12}(\frac{T}{\varepsilon_f})^2-\frac{11\pi^4}{360}(\frac{T}{\varepsilon_f})^4+O(\frac{T}{\varepsilon_f})^6\right]. \quad \text{(B.42)}\end{aligned}$$

B.3.3 Quadrupole Momentum Fluctuation

The quadrupole momentum is defined

$$Q_{xy} = p_x^2 - p_y^2, \quad \text{(B.43)}$$

where p_x and p_y are the x and y components of particle momentum respectively.

The quadrupole momentum fluctuation is

$$\begin{aligned}\langle(\Delta Q_{xy})^2\rangle &= \langle Q_{xy}^2\rangle - \langle Q_{xy}\rangle^2 \\ &= \langle Q_{xy}^2\rangle. \quad \text{(B.44)}\end{aligned}$$

$\langle Q_{xy}\rangle = 0$ is because of the symmetry between p_x and p_y.

$$\begin{aligned}
\langle Q_{xy}^2 \rangle &= \frac{\int d^3p(p_x^2 - p_y^2)^2 f(p)}{\int d^3p f(p)} \\
&= \frac{\frac{gV}{h^3}\int d^3p(p_x^2 - p_y^2)^2 f(p)}{\frac{gV}{h^3}\int d^3p f(p)} \\
&= \frac{\frac{gV}{h^3}\int d^3p(p_x^2 - p_y^2)^2 f(p)}{\frac{g}{h^3}\int d^3x d^3p f(p)} \\
&= \frac{1}{\bar{N}}\frac{gV}{h^3}\int d^3p(p_x^2 - p_y^2)^2 f(p). \qquad \text{(B.45)}
\end{aligned}$$

Using the relations

$$p_x = p\sin\theta\cos\phi, \quad p_y = p\sin\theta\sin\phi, \quad p_z = p\cos\theta, \qquad \text{(B.46)}$$

we obtain

$$\begin{aligned}
\langle Q_{xy}^2 \rangle &= \frac{1}{\bar{N}}\frac{gV}{h^3}\int d^3p(p_x^2 - p_y^2)^2 f(p) \\
&= \frac{1}{\bar{N}}\frac{gV}{h^3}\int_0^\infty\int_0^\pi\int_0^{2\pi} p^2\sin\theta dp d\theta d\phi p^4(\cos^2\phi - \sin^2\phi)^2\sin^4\theta f(p) \\
&= \frac{1}{\bar{N}}\frac{gV}{h^3}\int_0^\infty dp p^6 f(p)\int_0^\pi d\theta\sin^5\theta\int_0^{2\pi} d\phi(\cos^2\phi - \sin^2\phi)^2 \\
&= \frac{16}{15}\pi\frac{1}{\bar{N}}\frac{gV}{h^3}\int_0^\infty dp p^6 f(p) \\
&= \frac{16}{15}\pi\frac{1}{\bar{N}}\frac{gV}{h^3}\times FUI(6) \\
&= \frac{16}{15}\pi\frac{1}{\bar{N}}\frac{gV}{h^3}\frac{(2mT)^{7/2}}{2}\int_0^\infty dy y^{\frac{6-1}{2}}\frac{1}{e^{y-\nu}+1} \\
&= \frac{16}{15}\pi\frac{1}{\bar{N}}\frac{gV}{h^3}\frac{(2mT)^{7/2}}{2}\int_0^\infty dy\frac{y^{\frac{7}{2}-1}}{e^{y-\nu}+1} \\
&= \frac{1}{\bar{N}}\frac{gV}{h^3}(2\pi mT)^{3/2}(2mT)^2 f_{7/2}(\nu). \qquad \text{(B.47)}
\end{aligned}$$

From Eq. (B.6), we know the low T expansion of $f_{7/2}(\nu)$

$$f_{7/2}(\nu) = \frac{16}{105\pi^{1/2}}\nu^{7/2}[1 + \frac{35\pi^2}{24}\nu^{-2} + \frac{49\pi^4}{384}\nu^{-4} + O(\nu^{-6})]. \tag{B.48}$$

Substituting Eqs. (B.37, B.48) into Eq. (B.47), we obtain

$$\begin{aligned}\langle Q_{xy}^2\rangle &= \frac{1}{V\frac{g}{h^3}(2mT)^{\frac{3}{2}}\frac{4\pi}{3}(\frac{\varepsilon_f}{T})^{\frac{3}{2}}}\frac{gV}{h^3}(2\pi mT)^{3/2}(2mT)^2\frac{16}{105\pi^{1/2}} \\ &\quad \times\nu^{7/2}[1 + \frac{35\pi^2}{24}\nu^{-2} + \frac{49\pi^4}{384}\nu^{-4} + O(\nu^{-6})] \\ &= (2mT)^2\frac{4}{35}(\frac{T}{\varepsilon_f})^{\frac{3}{2}}[\nu^{7/2} + \frac{35\pi^2}{24}\nu^{3/2} + \frac{49\pi^4}{384}\nu^{-1/2} + O(\nu^{-5/2})]. \end{aligned} \tag{B.49}$$

Using Eq. (B.27, B.29, B.31), we obtain the quadrupole momentum fluctuation at low T

$$\langle Q_{xy}^2\rangle = (2mT)^2\frac{4}{35}(\frac{\varepsilon_f}{T})^2\left[1 + \frac{7\pi^2}{6}(\frac{T}{\varepsilon_f})^2 - \frac{49\pi^4}{720}(\frac{T}{\varepsilon_f})^4 + O(\frac{T}{\varepsilon_f})^6\right]. \tag{B.50}$$

APPENDIX C

FREE FERMI GAS AT T

C.1 Multiplicity and Quadrupole Momentum Fluctuations of Free Fermi Gas at T

C.1.1 Multiplicity Fluctuation

From Eq. (B.12), we know the average multiplicity of free Fermi gas is

$$\bar{N} = V\frac{g}{h^3}(2\pi mT)^{\frac{3}{2}} f_{3/2}(\nu). \tag{C.1}$$

The multiplicity fluctuation is given in Eq. (B.39)

$$\langle(\Delta N)^2\rangle = \left(\frac{\partial \bar{N}}{\partial \nu}\right)_{T,V}. \tag{C.2}$$

Substituting Eq. (C.1) into Eq. (C.2), we obtain

$$\begin{aligned}\langle(\Delta N)^2\rangle &= \left.\frac{\partial[V\frac{g}{h^3}(2\pi mT)^{\frac{3}{2}} f_{3/2}(\nu)]}{\partial\nu}\right|_{T,V} \\ &= V\frac{g}{h^3}(2\pi mT)^{\frac{3}{2}}\frac{1}{\Gamma(\frac{3}{2})}\int_0^\infty dy \frac{y^{\frac{1}{2}}e^{y-\nu}}{(e^{y-\nu}+1)^2}.\end{aligned} \tag{C.3}$$

Therefore, the normalized multiplicity fluctuation is

$$\begin{aligned}\frac{\langle(\Delta N)^2\rangle}{\bar{N}} &= \frac{V\frac{g}{h^3}(2\pi mT)^{\frac{3}{2}}\frac{1}{\Gamma(\frac{3}{2})}\int_0^\infty dy\frac{y^{\frac{1}{2}}e^{y-\nu}}{(e^{y-\nu}+1)^2}}{V\frac{g}{h^3}(2\pi mT)^{\frac{3}{2}}\frac{1}{\Gamma(\frac{3}{2})}\int_0^\infty dy\frac{y^{\frac{1}{2}}}{e^{y-\nu}+1}} \\ &= \frac{\int_0^\infty dy\frac{y^{\frac{1}{2}}e^{y-\nu}}{(e^{y-\nu}+1)^2}}{\int_0^\infty dy\frac{y^{\frac{1}{2}}}{e^{y-\nu}+1}}.\end{aligned} \tag{C.4}$$

C.1.2 Quadrupole Momentum Fluctuation

From Eq. (B.47), we know the quadrupole momentum fluctuation is

$$\langle Q_{xy}^2 \rangle = \frac{1}{\bar{N}} \frac{gV}{h^3} (2\pi mT)^{3/2} (2mT)^2 f_{7/2}(\nu). \tag{C.5}$$

Substituting Eq. (C.1) into Eq. (C.5), we obtain

$$\begin{aligned} \langle Q_{xy}^2 \rangle &= \frac{\frac{gV}{h^3}(2\pi mT)^{3/2}(2mT)^2 f_{7/2}(\nu)}{V\frac{g}{h^3}(2\pi mT)^{\frac{3}{2}} f_{3/2}(\nu)} \\ &= (2mT)^2 \frac{4}{15} \frac{\int_0^\infty dy \frac{y^{\frac{5}{2}}}{e^{y-\nu}+1}}{\int_0^\infty dy \frac{y^{\frac{1}{2}}}{e^{y-\nu}+1}} \\ &= (2mT)^2 F_{QC}(\nu), \end{aligned} \tag{C.6}$$

where $F_{QC}(\nu) = \frac{4}{15} \frac{\int_0^\infty dy \frac{y^{\frac{5}{2}}}{e^{y-\nu}+1}}{\int_0^\infty dy \frac{y^{\frac{1}{2}}}{e^{y-\nu}+1}}$ is quantum correction factor for fermions.

C.2 The Relation Between Fermi Energy ε_f and ν

From Eq. (B.16), we know the relation between Fermi energy ε_f and ν

$$\varepsilon_f^{3/2} = \frac{3\sqrt{\pi}}{4} T^{3/2} f_{3/2}(\nu). \tag{C.7}$$

We would like to derive the relation between $\frac{T}{\varepsilon_f}$ and ν. Thus

$$\begin{aligned} \frac{T}{\varepsilon_f} &= \frac{1}{[\frac{3\sqrt{\pi}}{4} f_{3/2}(\nu)]^{\frac{2}{3}}} \\ &= \frac{1}{[\frac{3}{2}\int_0^\infty dy \frac{y^{\frac{1}{2}}}{e^{y-\nu}+1}]^{\frac{2}{3}}}. \end{aligned} \tag{C.8}$$

APPENDIX D

COULOMB CORRECTION

D.1 Quadrupole Momentum Fluctuation with Coulomb Correction in Classical Case

For the classical case, assuming particles follow the Maxwell-Boltzmann distribution, then the quadrupole momentum fluctuation including the Coulomb effect is:

$$\begin{aligned}\langle Q_{xy}^2\rangle &= \frac{\int d^3p(p_x^2-p_y^2)^2 e^{-(\frac{p^2}{2mT}+\frac{1.44\times 4\pi\hbar^2 Z_p Z_s}{p^2 VT})}}{\int d^3p e^{-(\frac{p^2}{2mT}+\frac{1.44\times 4\pi\hbar^2 Z_p Z_s}{p^2 VT})}} \\ &= \frac{\int d^3p(p_x^2-p_y^2)^2 e^{-(ap^2+\frac{b}{p^2})}}{\int d^3p e^{-(ap^2+\frac{b}{p^2})}}. \end{aligned} \tag{D.1}$$

For simplicity, we write

$$a=\frac{1}{2mT}, \quad b=\frac{1.44\times 4\pi\hbar^2 Z_p Z_s}{VT}. \tag{D.2}$$

Using

$$p_x = p\sin\theta\cos\phi, \quad p_y = p\sin\theta\sin\phi, \quad p_z = p\cos\theta, \tag{D.3}$$

one obtains

$$\begin{aligned}\langle Q_{xy}^2\rangle &= \frac{\int d^3p(p_x^2-p_y^2)^2 e^{-(ap^2+\frac{b}{p^2})}}{\int d^3p e^{-(ap^2+\frac{b}{p^2})}} \\ &= \frac{\int_0^\infty dp p^6 e^{-(ap^2+\frac{b}{p^2})}\int_0^\pi d\theta\sin^5\theta\int_0^{2\pi}d\phi(\cos^2\phi-\sin^2\phi)^2}{\int_0^\infty dp p^2 e^{-(ap^2+\frac{b}{p^2})}\int_0^\pi d\theta\sin\theta\int_0^{2\pi}d\phi}\end{aligned}$$

$$= \frac{4}{15}\frac{\int_0^\infty dpp^6 e^{-(ap^2+\frac{b}{p^2})}}{\int_0^\infty dpp^2 e^{-(ap^2+\frac{b}{p^2})}}. \tag{D.4}$$

Define the integral

$$I_n = \int_0^\infty dx x^n e^{-(ax^2+\frac{b}{x^2})}, \tag{D.5}$$

where $a > 0, b > 0$. Then

$$\langle Q_{xy}^2 \rangle = \frac{4}{15}\frac{I_6}{I_2}. \tag{D.6}$$

Now we are going to calculate the integral I_n,

$$\begin{aligned}
I_n &= \int_0^\infty dx x^n e^{-(ax^2+\frac{b}{x^2})} \\
&= \frac{1}{n+1}\int_0^\infty dx^{n+1} e^{-(ax^2+\frac{b}{x^2})} \\
&= -\frac{1}{n+1}\int_0^\infty dx x^{n+1}[-(2ax - \frac{2b}{x^3})]e^{-(ax^2+\frac{b}{x^2})} \\
&= \frac{2}{n+1}\int_0^\infty dx x^{n+1}(ax - \frac{b}{x^3})e^{-(ax^2+\frac{b}{x^2})} \\
&= \frac{2}{n+1}[a\int_0^\infty dx x^{n+2} e^{-(ax^2+\frac{b}{x^2})} - b\int_0^\infty dx x^{n-2} e^{-(ax^2+\frac{b}{x^2})}] \\
&= \frac{2}{n+1}[aI_{n+2} - bI_{n-2}].
\end{aligned} \tag{D.7}$$

Then

$$I_{n+2} = \frac{n+1}{2a}I_n + \frac{b}{a}I_{n-2}. \tag{D.8}$$

We derived the recurrence relation for the integral I_n. If we know two of them, we can calculate all the integrals. On the other hand,

$$\begin{aligned}
I_n &= \int_0^\infty dx x^n e^{-(ax^2+\frac{b}{x^2})} \\
&= \int_0^\infty dx x^n e^{-(ab)^{1/2}[(\frac{a}{b})^{1/2}x^2 + \frac{1}{(\frac{a}{b})^{1/2}x^2}]} \\
&= (\frac{b}{a})^{(n+1)/4}\int_0^\infty dy y^n e^{-(ab)^{1/2}[y^2+\frac{1}{y^2}]}
\end{aligned}$$

$$= (\frac{b}{a})^{(n+1)/4} e^{-2(ab)^{1/2}} \int_0^\infty dy y^n e^{-(ab)^{1/2}(y-\frac{1}{y})^2}. \quad \text{(D.9)}$$

First we calculate I_0. Let $n = 0$ in Eq. (D.9) and use the variable substitution $x = \frac{1}{y}$,

$$\begin{aligned}
I_0 &= (\frac{b}{a})^{1/4} e^{-2(ab)^{1/2}} \int_0^\infty dy e^{-(ab)^{1/2}(y-\frac{1}{y})^2} \\
&= \frac{1}{2}(\frac{b}{a})^{1/4} e^{-2(ab)^{1/2}} [\int_0^\infty dy e^{-(ab)^{1/2}(y-\frac{1}{y})^2} + \int_0^\infty dx \frac{1}{x^2} e^{-(ab)^{1/2}(x-\frac{1}{x})^2}] \\
&= \frac{1}{2}(\frac{b}{a})^{1/4} e^{-2(ab)^{1/2}} \int_0^\infty dy (1 + \frac{1}{y^2}) e^{-(ab)^{1/2}(y-\frac{1}{y})^2} \\
&= \frac{1}{2}(\frac{b}{a})^{1/4} e^{-2(ab)^{1/2}} \int_0^\infty d(y - \frac{1}{y}) e^{-(ab)^{1/2}(y-\frac{1}{y})^2} \\
&= \frac{1}{2}(\frac{b}{a})^{1/4} e^{-2(ab)^{1/2}} \int_{-\infty}^\infty dx e^{-(ab)^{1/2}x^2} \\
&= \frac{\pi^{1/2}}{2a^{1/2}} e^{-2(ab)^{1/2}}. \quad \text{(D.10)}
\end{aligned}$$

Second we calculate I_{-2}. Let $n = -2$ in Eq. (D.9)

$$\begin{aligned}
I_{-2} &= (\frac{b}{a})^{(-2+1)/4} e^{-2(ab)^{1/2}} \int_0^\infty dy y^{-2} e^{-(ab)^{1/2}(y-\frac{1}{y})^2} \\
&= (\frac{b}{a})^{-1/2} (\frac{b}{a})^{1/4} e^{-2(ab)^{1/2}} \int_0^\infty dy \frac{1}{y^2} e^{-(ab)^{1/2}(y-\frac{1}{y})^2} \\
&= (\frac{b}{a})^{-1/2} (\frac{b}{a})^{1/4} e^{-2(ab)^{1/2}} \int_0^\infty dx e^{-(ab)^{1/2}(x-\frac{1}{x})^2} \\
&= (\frac{b}{a})^{-1/2} I_0 \\
&= (\frac{b}{a})^{-1/2} \frac{\pi^{1/2}}{2a^{1/2}} e^{-2(ab)^{1/2}} \\
&= \frac{\pi^{1/2}}{2b^{1/2}} e^{-2(ab)^{1/2}}. \quad \text{(D.11)}
\end{aligned}$$

Using Eqs. (D.8, D.10, D.11), we can calculate

$$\begin{aligned}
I_2 &= \frac{1}{2a} I_0 + \frac{b}{a} I_{-2} \\
&= \frac{1}{2a} I_0 + \frac{b}{a} (\frac{b}{a})^{-1/2} I_0
\end{aligned}$$

$$
\begin{aligned}
&= [\frac{1}{2a} + (\frac{b}{a})^{1/2}] I_0 \\
&= [\frac{1}{2a} + (\frac{b}{a})^{1/2}] \frac{\pi^{1/2}}{2a^{1/2}} e^{-2(ab)^{1/2}} \\
&= \frac{1 + 2(ab)^{1/2}}{4a^{3/2}} \pi^{1/2} e^{-2(ab)^{1/2}}. \qquad \text{(D.12)}
\end{aligned}
$$

$$
\begin{aligned}
I_4 &= \frac{3}{2a} I_2 + \frac{b}{a} I_0 \\
&= \frac{3}{2a} [\frac{1}{2a} + (\frac{b}{a})^{1/2}] I_0 + \frac{b}{a} I_0 \\
&= [\frac{3}{(2a)^2} + \frac{3}{2a} (\frac{b}{a})^{1/2} + \frac{b}{a}] I_0 \\
&= [\frac{3}{(2a)^2} + \frac{3}{2a} (\frac{b}{a})^{1/2} + \frac{b}{a}] \frac{\pi^{1/2}}{2a^{1/2}} e^{-2(ab)^{1/2}} \\
&= \frac{3 + 6(ab)^{1/2} + 4ab}{8a^{5/2}} \pi^{1/2} e^{-2(ab)^{1/2}}. \qquad \text{(D.13)}
\end{aligned}
$$

$$
\begin{aligned}
I_6 &= \frac{5}{2a} I_4 + \frac{b}{a} I_2 \\
&= \frac{5}{2a} [\frac{3}{(2a)^2} + \frac{3}{2a} (\frac{b}{a})^{1/2} + \frac{b}{a}] I_0 + \frac{b}{a} [\frac{1}{2a} + (\frac{b}{a})^{1/2}] I_0 \\
&= [\frac{15}{(2a)^3} + \frac{15}{(2a)^2} (\frac{b}{a})^{1/2} + \frac{3b}{a^2} + (\frac{b}{a})^{3/2}] I_0 \\
&= [\frac{15}{(2a)^3} + \frac{15}{(2a)^2} (\frac{b}{a})^{1/2} + \frac{3b}{a^2} + (\frac{b}{a})^{3/2}] \frac{\pi^{1/2}}{2a^{1/2}} e^{-2(ab)^{1/2}} \\
&= \frac{15 + 30(ab)^{1/2} + 24ab + 8(ab)^{3/2}}{16a^{7/2}} \pi^{1/2} e^{-2(ab)^{1/2}}. \qquad \text{(D.14)}
\end{aligned}
$$

Substituting Eqs. (D.12, D.14) into Eq. (D.6), we obtain

$$
\begin{aligned}
\langle Q_{xy}^2 \rangle &= \frac{4}{15} \frac{I_6}{I_2} \\
&= \frac{4}{15} \frac{\frac{15 + 30(ab)^{1/2} + 24ab + 8(ab)^{3/2}}{16a^{7/2}} \pi^{1/2} e^{-2(ab)^{1/2}}}{\frac{1 + 2(ab)^{1/2}}{4a^{3/2}} \pi^{1/2} e^{-2(ab)^{1/2}}}
\end{aligned}
$$

$$
\begin{aligned}
&= \frac{4}{15}\frac{1}{4a^2}\frac{15+30(ab)^{1/2}+24ab+8(ab)^{3/2}}{1+2(ab)^{1/2}} \\
&= \frac{1}{a^2}\frac{1+2(ab)^{1/2}+\frac{8}{5}ab+\frac{8}{15}(ab)^{3/2}}{1+2(ab)^{1/2}} \\
&= \frac{1}{a^2}[1+\frac{\frac{8}{5}ab+\frac{8}{15}(ab)^{3/2}}{1+2(ab)^{1/2}}]. \qquad \text{(D.15)}
\end{aligned}
$$

D.2 Multiplicity Fluctuation with Coulomb Correction in Classical Case

For the classical case, the single particle partition function considering the Coulomb effect is

$$
\begin{aligned}
Z_1 &= \frac{1}{h^3}\int e^{-\beta\varepsilon}d^3xd^3p \\
&= \frac{4\pi V}{h^3}\int_0^\infty e^{-(\frac{p^2}{2mT}+\frac{1.44\times 4\pi Z_p Z_s}{VTp^2})}p^2dp \\
&= \frac{4\pi V}{h^3}\int_0^\infty e^{-(ap^2+\frac{b}{p^2})}p^2dp \\
&= \frac{4\pi V}{h^3}\times[\frac{1+2(ab)^{1/2}}{4a^{3/2}}\pi^{1/2}e^{-2(ab)^{1/2}}]. \qquad \text{(D.16)}
\end{aligned}
$$

Then the pressure is

$$
\begin{aligned}
P &= \frac{N}{\beta}\frac{\partial}{\partial V}\ln Z_1 \\
&= NT\frac{\partial}{\partial V}\ln\{\frac{4\pi V}{h^3}\times[\frac{1+2(ab)^{1/2}}{4a^{3/2}}\pi^{1/2}e^{-2(ab)^{1/2}}]\} \\
&= NT\frac{\partial}{\partial V}\ln\{V\times[1+2(ab)^{1/2}]e^{-2(ab)^{1/2}}\} \\
&= NT\frac{\partial}{\partial V}\ln\{V\times[1+2(ab')^{1/2}V^{-1/2}]e^{-2(ab')^{1/2}V^{-1/2}}\} \\
&= NT[\frac{1}{V}-\frac{(ab')^{1/2}V^{-3/2}}{1+2(ab')^{1/2}V^{-1/2}}+(ab')^{1/2}V^{-3/2}] \\
&= NT[\frac{1}{V}+\frac{2ab'V^{-2}}{1+2(ab')^{1/2}V^{-1/2}}], \qquad \text{(D.17)}
\end{aligned}
$$

where $b' = bV = \frac{1.44\times 4\pi\hbar^2 Z_p Z_s}{T}$. Thus

$$\begin{aligned}
\left.\frac{\partial P}{\partial V}\right|_{N,T} &= NT\{-\frac{1}{V^2} + \frac{-4ab'V^{-3}[1+2(ab')^{1/2}V^{-1/2}] - 2ab'V^{-2}[-(ab')^{1/2}V^{-3/2}]}{[1+2(ab')^{1/2}V^{-1/2}]^2}\} \\
&= NT\{-\frac{1}{V^2} - \frac{4ab'}{[1+2(ab')^{1/2}V^{-1/2}]V^3} + \frac{2(ab')^{3/2}}{[1+2(ab')^{1/2}V^{-1/2}]^2V^{7/2}}\} \\
&= -\frac{NT}{V^2}\{1 + \frac{4ab'}{[1+2(ab')^{1/2}V^{-1/2}]V} - \frac{2(ab')^{3/2}}{[1+2(ab')^{1/2}V^{-1/2}]^2V^{3/2}}\}. \quad \text{(D.18)}
\end{aligned}$$

The normalized multiplicity fluctuation is

$$\begin{aligned}
\frac{\langle(\Delta N)^2\rangle}{\bar{N}} &= -\frac{TN}{V^2}\left.\frac{\partial V}{\partial P}\right|_{T,N} \\
&= -\frac{TN}{V^2} \times \frac{1}{-\frac{NT}{V^2}\{1 + \frac{4ab'}{[1+2(ab')^{1/2}V^{-1/2}]V} - \frac{2(ab')^{3/2}}{[1+2(ab')^{1/2}V^{-1/2}]^2V^{3/2}}\}} \\
&= \frac{1}{1 + \frac{4ab'}{[1+2(ab')^{1/2}V^{-1/2}]V} - \frac{2(ab')^{3/2}}{[1+2(ab')^{1/2}V^{-1/2}]^2V^{3/2}}}. \quad \text{(D.19)}
\end{aligned}$$

To simplify the above equation, we define

$$x = \frac{ab'}{V} = ab, \quad \text{(D.20)}$$

then

$$\frac{\langle(\Delta N)^2\rangle}{\bar{N}} = \frac{1}{1 + \frac{4x}{1+2x^{1/2}} - \frac{2x^{3/2}}{(1+2x^{1/2})^2}}. \quad \text{(D.21)}$$

The last equation (D.21) cannot be directly applied to the multiplicity fluctuations say of protons, since we know most of those fluctuations are due to fermion quenching. In fact the protons and neutrons multiplicity fluctuations are very similar when observed in the perpendicular direction to the beam, see Fig. 5.1. In practice one could apply Eq. (D.21) to the difference between p and n or ^3H, ^3He multiplicity fluctuations which we could not do because of the small differences in the model case.

D.3 Quadrupole Momentum Fluctuation and Multiplicity Fluctuation with Coulomb correction for Fermions in Quantum Case

For the quantum case, assuming particles follow the Fermi-Dirac distribution,

$$f(p) = \frac{1}{e^{[\varepsilon + \frac{1.44\times 4\pi\hbar^2 Z_p Z_s}{Vp^2} - \mu]/T} + 1}, \tag{D.22}$$

where $\varepsilon = \frac{p^2}{2m}$ is the energy , μ is the chemical potential, T is the temperature. The average number of particles is

$$\begin{aligned} \bar{N} &= \frac{g}{h^3}\int d^3x d^3p f(p) \\ &= \frac{gV}{h^3} 4\pi \int_0^\infty dp p^2 f(p). \end{aligned} \tag{D.23}$$

Let's make the integral variable transformation,

$$\varepsilon = \frac{p^2}{2m}, \quad p = (2m\varepsilon)^{\frac{1}{2}}, \quad dp = \frac{m}{\sqrt{2m\varepsilon}} d\varepsilon. \tag{D.24}$$

Thus Eq. (D.23) becomes

$$\begin{aligned} \bar{N} &= \frac{gV}{h^3} 4\pi \int_0^\infty dp p^2 f(p) \\ &= \frac{gV}{h^3} 4\pi \frac{(2m)^{\frac{3}{2}}}{2} \int_0^\infty d\varepsilon \varepsilon^{\frac{1}{2}} f(\varepsilon) \\ &= \frac{gV}{h^3} 4\pi \frac{(2m)^{\frac{3}{2}}}{2} \int_0^\infty d\varepsilon \varepsilon^{\frac{1}{2}} \frac{1}{e^{[\varepsilon + \frac{1.44\times 4\pi\hbar^2 Z_p Z_s}{Vp^2} - \mu]/T} + 1} \\ &= \frac{gV}{h^3} 4\pi \frac{(2m)^{\frac{3}{2}}}{2} \int_0^\infty d\varepsilon \varepsilon^{\frac{1}{2}} \frac{1}{e^{[\varepsilon + \frac{1.44\times 4\pi\hbar^2 Z_p Z_s}{2mV\varepsilon} - \mu]/T} + 1} \\ &= \frac{gV}{h^3} 4\pi \frac{(2m)^{\frac{3}{2}}}{2} \int_0^\infty d\varepsilon \varepsilon^{\frac{1}{2}} \frac{1}{e^{[\varepsilon + \frac{A}{\varepsilon} - \mu]/T} + 1}, \end{aligned} \tag{D.25}$$

where $A = \frac{1.44\times 4\pi\hbar^2 Z_p Z_s}{2mV}$. Let's make the integral variable transformation again

$$y = \frac{\varepsilon}{T}, \quad \nu = \frac{\mu}{T}. \tag{D.26}$$

Therefore, Eq. (D.25) becomes

$$\bar{N} = \frac{gV}{h^3} 4\pi \frac{(2mT)^{\frac{3}{2}}}{2} \int_0^\infty dy y^{\frac{1}{2}} \frac{1}{e^{y+\frac{A}{yT^2}-\nu}+1}. \tag{D.27}$$

The multiplicity fluctuation is (this definition is equivalent to Eq. (D.19) if the density $\frac{\bar{N}}{V}$ is function of P and T only [1])

$$\langle (\Delta N)^2 \rangle = T(\frac{\partial \bar{N}}{\partial \mu})_{T,V} = (\frac{\partial \bar{N}}{\partial \nu})_{T,V}. \tag{D.28}$$

Substituting Eq. (D.27) into Eq. (D.28), one can obtain

$$\langle (\Delta N)^2 \rangle = \frac{gV}{h^3} 4\pi \frac{(2mT)^{\frac{3}{2}}}{2} \int_0^\infty dy y^{\frac{1}{2}} \frac{e^{y+\frac{A}{yT^2}-\nu}}{(e^{y+\frac{A}{yT^2}-\nu}+1)^2}. \tag{D.29}$$

Dividing Eq. (D.29) by Eq. (D.27), one can get

$$\begin{aligned} \frac{\langle (\Delta N)^2 \rangle}{\bar{N}} &= \frac{\frac{gV}{h^3} 4\pi \frac{(2mT)^{\frac{3}{2}}}{2} \int_0^\infty dy y^{\frac{1}{2}} \frac{e^{y+\frac{A}{yT^2}-\nu}}{(e^{y+\frac{A}{yT^2}-\nu}+1)^2}}{\frac{gV}{h^3} 4\pi \frac{(2mT)^{\frac{3}{2}}}{2} \int_0^\infty dy y^{\frac{1}{2}} \frac{1}{e^{y+\frac{A}{yT^2}-\nu}+1}} \\ &= \frac{\int_0^\infty dy y^{\frac{1}{2}} \frac{e^{y+\frac{A}{yT^2}-\nu}}{(e^{y+\frac{A}{yT^2}-\nu}+1)^2}}{\int_0^\infty dy y^{\frac{1}{2}} \frac{1}{e^{y+\frac{A}{yT^2}-\nu}+1}}. \end{aligned} \tag{D.30}$$

In the same framework, we also calculate the quadrupole momentum fluctuation

$$\begin{aligned}\langle Q_{xy}^2 \rangle &= \frac{\int d^3p (p_x^2 - p_y^2)^2 \frac{1}{e^{[\frac{p^2}{2m} + \frac{1.44\times 4\pi\hbar^2 Z_p Z_s}{p^2 V} - \mu]/T} + 1}}{\int d^3p \frac{1}{e^{[\frac{p^2}{2m} + \frac{1.44\times 4\pi\hbar^2 Z_p Z_s}{p^2 V} - \mu]/T} + 1}} \\ &= (2mT)^2 \frac{4}{15} \frac{\int_0^\infty dy y^{\frac{5}{2}} \frac{1}{e^{y + \frac{A}{yT^2} - \nu} + 1}}{\int_0^\infty dy y^{\frac{1}{2}} \frac{1}{e^{y + \frac{A}{yT^2} - \nu} + 1}}. \end{aligned} \tag{D.31}$$

APPENDIX E

SKYRME NEOS

E.1 The General Expressions of Different Quantities for Skyrme NEOS

One of the most popular NEOS used in the literature is the Skyrme interaction. Hundreds of interactions have been proposed. They have the same form with different parameters determined by fitting experimental data. Here we will show the general expressions of different quantities for Skyrme NEOS. In order to avoid the confusion, we will keep the same notation in the literature.

E.1.1 Energy per Nucleon E/A

For Skyrme NEOS of asymmetric NM, with $Y_p = \frac{Z}{A}$ or $I = \frac{N-Z}{A}$, the energy per nucleon is

$$\begin{aligned}\frac{E}{A}(Y_p \text{ or } I, \rho) &= \frac{3}{5}\frac{\hbar^2}{2m}(\frac{3\pi^2}{2})^{2/3}\rho^{2/3}F_{5/3} + \frac{1}{8}t_0\rho[2(x_0+2) - (2x_0+1)F_2] \\ &+\frac{1}{48}t_3\rho^{\sigma+1}[2(x_3+2) - (2x_3+1)F_2] + \frac{3}{40}(\frac{3\pi^2}{2})^{2/3}\rho^{5/3}[aF_{5/3} + bF_{8/3}],\end{aligned} \tag{E.1}$$

where

$$a = t_1(x_1+2) + t_2(x_2+2), \quad b = \frac{1}{2}[t_2(2x_2+1) - t_1(2x_1+1)], \tag{E.2}$$

$$\sigma = \alpha, \tag{E.3}$$

$$F_n(Y_p) = 2^{n-1}[Y_p^n + (1-Y_p)^n], \quad F_n(I) = \frac{1}{2}[(1+I)^n + (1-I)^n]. \tag{E.4}$$

The parameters are $t_0, t_1, t_2, t_3, x_0, x_1, x_2, x_3, \sigma$. Recently, a more complicated form of Skyrme NEOS has been proposed and has more parameters [95], it is an extension

of the present form we discussed here.

E.1.2 Pressure P

Using Eq. (1.7), the pressure is

$$\begin{aligned} P &= \rho^2 \frac{\partial \frac{E}{A}(I,\rho)}{\partial \rho} \\ &= \frac{3}{5}\frac{\hbar^2}{2m}(\frac{3\pi^2}{2})^{2/3}\frac{2}{3}\rho^{5/3}F_{5/3} + \frac{1}{8}t_0\rho^2[2(x_0+2)-(2x_0+1)F_2] \\ &\quad + \frac{1}{48}t_3(\sigma+1)\rho^{\sigma+2}[2(x_3+2)-(2x_3+1)F_2] + \frac{3}{40}(\frac{3\pi^2}{2})^{2/3}\frac{5}{3}\rho^{8/3}[aF_{5/3}+bF_{8/3}]. \end{aligned} \tag{E.5}$$

E.1.3 Incompressibility K

The incompressibility is

$$\begin{aligned} K &= 9\frac{\partial P}{\partial \rho}\bigg|_{\rho=\rho_0} \\ &= 9\times\Big\{\frac{3}{5}\frac{\hbar^2}{2m}(\frac{3\pi^2}{2})^{2/3}\frac{2}{3}\frac{5}{3}\rho^{2/3}F_{5/3} + \frac{1}{8}t_0 2\rho[2(x_0+2)-(2x_0+1)F_2] \\ &\quad + \frac{1}{48}t_3(\sigma+1)(\sigma+2)\rho^{\sigma+1}[2(x_3+2)-(2x_3+1)F_2] \\ &\quad + \frac{3}{40}(\frac{3\pi^2}{2})^{2/3}\frac{5}{3}\frac{8}{3}\rho^{5/3}[aF_{5/3}+bF_{8/3}]\Big\}\bigg|_{\rho=\rho_0}. \end{aligned} \tag{E.6}$$

E.1.4 Symmetry Energy S(ρ)

Before we calculate the expression for symmetry energy, we easily show that the function $F_n(I)$ satisfies

$$\frac{\partial^2 F_n(I)}{\partial I^2} = n(n-1)F_{n-2}(I). \tag{E.7}$$

The symmetry energy is

$$\begin{aligned} S(\rho) &= \frac{1}{2}\frac{\partial^2 \frac{E}{A}(I,\rho)}{\partial I^2}\Big|_{I=0} \\ &= \frac{1}{2}\times\Big\{\frac{3}{5}\frac{\hbar^2}{2m}(\frac{3\pi^2}{2})^{2/3}\rho^{2/3}\frac{5}{3}\frac{2}{3}F_{-1/3}+\frac{1}{8}t_0\rho[-2(2x_0+1)] \\ &\quad +\frac{1}{48}t_3\rho^{\sigma+1}[-2(2x_3+1)]+\frac{3}{40}(\frac{3\pi^2}{2})^{2/3}\rho^{5/3}[a\frac{5}{3}\frac{2}{3}F_{-1/3}+b\frac{8}{3}\frac{5}{3}F_{2/3}]\Big\}\Big|_{I=0} \\ &= \frac{1}{3}\frac{\hbar^2}{2m}(\frac{3\pi^2}{2})^{2/3}\rho^{2/3}-\frac{1}{8}t_0(2x_0+1)\rho-\frac{1}{48}t_3(2x_3+1)\rho^{\sigma+1}+\frac{1}{24}(\frac{3\pi^2}{2})^{2/3}(a+4b)\rho^{5/3}. \end{aligned} \tag{E.8}$$

E.1.5 Curvature of Symmetry Energy L

The curvature of symmetry energy L is

$$\begin{aligned} L &= 3\rho_0\frac{\partial S(\rho)}{\partial\rho}\Big|_{\rho=\rho_0} \\ &= \frac{2}{3}\frac{\hbar^2}{2m}(\frac{3\pi^2}{2})^{2/3}\rho_0^{2/3}-\frac{3}{8}t_0(2x_0+1)\rho_0-\frac{1}{16}t_3(\sigma+1)(2x_3+1)\rho_0^{\sigma+1}+\frac{5}{24}(\frac{3\pi^2}{2})^{2/3}(a+4b)\rho_0^{5/3}. \end{aligned} \tag{E.9}$$

E.1.6 Incompressibility of Symmetry Energy K_{sym}

The incompressibility of symmetry energy K_{sym} is

$$\begin{aligned} K_{sym} &= 9\rho_0^2\frac{\partial^2 E_{sym}}{\partial\rho^2}\Big|_{\rho=\rho_0} \\ &= -\frac{2}{3}\frac{\hbar^2}{2m}(\frac{3\pi^2}{2})^{2/3}\rho_0^{2/3}-\frac{3}{16}t_3(\sigma+1)\sigma(2x_3+1)\rho_0^{\sigma+1}+\frac{5}{12}(\frac{3\pi^2}{2})^{2/3}(a+4b)\rho_0^{5/3}. \end{aligned} \tag{E.10}$$

APPENDIX F

DOUBLE RATIO THERMOMETER AND COALESCENCE MODEL

F.1 General Equation for Double Ratio Thermometer

In double ratio thermometer calculation, the assumption is that a thermodynamic equilibrium is established between free nucleons and composite fragments [260]. The fragments satisfy Maxwell-Boltzmann distribution. The yield of one specie fragment is

$$\begin{aligned}
Y(A,Z) &= N(A,Z) \\
&= \sum_i \frac{(2s_i(A,Z)+1)e^{-\frac{E_i(A,Z)}{T}}}{h^3}\int_0^\infty e^{-\frac{E}{T}}e^{\frac{\mu(A,Z)}{T}}d^3xd^3p \\
&= \Big[\sum_i (2s_i(A,Z)+1)e^{-\frac{E_i(A,Z)}{T}}\Big]\frac{V}{h^3}e^{\frac{\mu(A,Z)}{T}}\int_0^\infty e^{-\frac{E}{T}}d^3p \\
&= \omega(A,Z)\frac{V}{h^3}e^{\frac{\mu(A,Z)}{T}}4\pi\int_0^\infty e^{-\frac{E}{T}}p^2dp \\
&= \omega(A,Z)\frac{V}{h^3}e^{\frac{\mu(A,Z)}{T}}4\pi\frac{(2m_A)^{3/2}}{2}\int_0^\infty e^{-\frac{E}{T}}E^{1/2}dE \\
&= \omega(A,Z)\frac{V}{h^3}e^{\frac{\mu(A,Z)}{T}}4\pi\frac{(2m_A)^{3/2}}{2}\frac{\sqrt{\pi}}{2}T^{3/2} \\
&= \omega(A,Z)\frac{V}{h^3}e^{\frac{\mu(A,Z)}{T}}(2\pi m_A T)^{3/2} \\
&= V\omega(A,Z)\frac{A^{3/2}}{h^3}e^{\frac{\mu(A,Z)}{T}}(2\pi mT)^{3/2} \\
&= V\omega(A,Z)\frac{A^{3/2}}{\lambda_T^3}e^{\frac{\mu(A,Z)}{T}}, \qquad \text{(F.1)}
\end{aligned}$$

where

$$\omega(A,Z)=\sum_i(2s_i(A,Z)+1)e^{-\frac{E_i(A,Z)}{T}}, \quad \lambda_T=\frac{h}{\sqrt{2\pi mT}}. \qquad \text{(F.2)}$$

λ_T is the thermal wavelength. $s_i(A,Z)$ are the ground- and excited-state spins and $E_i(A,Z)$ are energies of these states, m is the mass of nucleon. $\mu(A,Z)$ is the chemical potential

$$\mu(A,Z) = Z\mu_{pF} + (A-Z)\mu_{nF} + B(A,Z), \tag{F.3}$$

where μ_{pF} and μ_{nF} are the chemical potentials of free proton and neutron respectively, $B(A,Z)$ is the binding energy of the fragment. Therefore

$$\begin{aligned}
\rho(A,Z) &= \frac{N(A,Z)}{V} \\
&= \omega(A,Z)\frac{A^{3/2}}{\lambda_T^3} e^{\frac{\mu(A,Z)}{T}} \\
&= \omega(A,Z)\frac{A^{3/2}}{\lambda_T^3} e^{\frac{Z\mu_{pF}+(A-Z)\mu_{nF}+B(A,Z)}{T}}.
\end{aligned} \tag{F.4}$$

We can write the densities of free proton and neutron from Eq. (F.4) respectively.

$$\rho_p = \frac{2}{\lambda_T^3} e^{\frac{\mu_{pF}}{T}} \rightarrow e^{\frac{\mu_{pF}}{T}} = \frac{\lambda_T^3}{2}\rho_p, \tag{F.5}$$

$$\rho_n = \frac{2}{\lambda_T^3} e^{\frac{\mu_{nF}}{T}} \rightarrow e^{\frac{\mu_{nF}}{T}} = \frac{\lambda_T^3}{2}\rho_n. \tag{F.6}$$

Substituting Eqs. (F.5, F.6) into Eq. (F.4), we obtain

$$\begin{aligned}
\rho(A,Z) &= \omega(A,Z)\frac{A^{3/2}}{\lambda_T^3} e^{\frac{Z\mu_{pF}+(A-Z)\mu_{nF}+B(A,Z)}{T}} \\
&= \omega(A,Z)\frac{A^{3/2}}{\lambda_T^3} (\frac{\lambda_T^3}{2}\rho_p)^Z (\frac{\lambda_T^3}{2}\rho_n)^{(A-Z)} e^{\frac{B(A,Z)}{T}} \\
&= \omega(A,Z)\frac{A^{3/2}}{2} (\frac{\lambda_T^3}{2})^{A-1} \rho_p^Z \rho_n^{(A-Z)} e^{\frac{B(A,Z)}{T}} \\
&= \omega(A,Z)\frac{A^{3/2}}{2} (\frac{\lambda_T^3}{2})^{A-1} \rho_p^Z \rho_n^N e^{\frac{B(A,Z)}{T}}.
\end{aligned} \tag{F.7}$$

We have written the number of neutron $N = A - Z$. If we ignore the excited states, then

$$\omega(A, Z) = 2s(A, Z) + 1, \tag{F.8}$$

and

$$\rho(A, Z) = [2s(A, Z) + 1]\frac{A^{3/2}}{2}(\frac{\lambda_T^3}{2})^{A-1}\rho_p^Z\rho_n^N e^{\frac{B(A,Z)}{T}} \tag{F.9}$$

F.2 Coalescence Model

F.2.1 Coalescence Model without Coulomb Correction

The basic assumption of the coalescence model is that complex particles are formed by the coalescence of nucleons which happen to share the same volume element of momentum space [269, 270]. The critical radius P_0 is treated as a free parameter. The probability P for finding one primary nucleon in the coalescence volume centered at momentum per nucleon $\vec{p}$ is

$$P = \frac{4\pi}{3}P_0^3\frac{1}{\bar{m}}\frac{d^3N(\vec{p})}{dp^3}, \tag{F.10}$$

where $\frac{d^3N(\vec{p})}{dp^3}$ is the differential nucleon multiplicity distribution and $\bar{m}$ is the average nucleon multiplicity.

For a given multiplicity m, the probability to find n of them in the coalescence volume is given by the binomial distribution

$$P(n|m) = C_m^n P^n(1 - P)^{m-n}. \tag{F.11}$$

Since each multiplicity m will have a probability $f(m)$, the average probability for

finding n nucleons in the coalescence volume is

$$\langle P(n)\rangle = \sum_{m\geq n} f(m)P(n|m) = \sum_{m\geq n} f(m)C_m^n P^n(1-P)^{m-n}. \tag{F.12}$$

Assuming a Poisson distribution of multiplicities

$$f(m) = \frac{(\bar{m})^m}{m!}e^{-\bar{m}}. \tag{F.13}$$

Then we obtain

$$\begin{aligned}
\langle P(n)\rangle &= \sum_{m\geq n} f(m)C_m^n P^n(1-P)^{m-n} \\
&= \sum_{m\geq n} \frac{(\bar{m})^m}{m!}e^{-\bar{m}}C_m^n P^n(1-P)^{m-n} \\
&= \sum_{m\geq n} \frac{(\bar{m})^m}{m!}e^{-\bar{m}}\frac{m!}{n!(m-n)!}P^n(1-P)^{m-n} \\
&= \frac{P^n e^{-\bar{m}}}{n!}\sum_{m\geq n}\frac{(\bar{m})^m}{(m-n)!}(1-P)^{m-n} \\
&= \frac{P^n(\bar{m})^n e^{-\bar{m}}}{n!}\sum_{m\geq n}\frac{(\bar{m})^{m-n}}{(m-n)!}(1-P)^{m-n} \\
&= \frac{P^n(\bar{m})^n e^{-\bar{m}}}{n!}\sum_{\nu}\frac{[\bar{m}(1-P)]^\nu}{n!} \\
&= \frac{P^n(\bar{m})^n e^{-\bar{m}}}{n!}e^{\bar{m}(1-P)} \\
&= \frac{(\bar{m}P)^n}{n!}e^{-\bar{m}P} \\
&\approx \frac{(\bar{m}P)^n}{n!}.
\end{aligned} \tag{F.14}$$

The approximation at the last step is because $\bar{m}P$ is very small usually. Then the average probability to have N neutrons and Z protons in the coalescence sphere is

$$\langle P(Z,N)\rangle = \langle P(0,Z)\rangle\langle P(N,0)\rangle$$

$$
\begin{aligned}
&= \frac{(\bar{m}_Z P_Z)^Z}{Z!}\frac{(\bar{m}_N P_N)^N}{N!} \\
&= \frac{(\bar{m}_Z P_Z)^Z}{Z!}\frac{(\bar{m}_N P_N)^N}{N!} \\
&= \frac{1}{N!Z!}[\frac{4\pi}{3}P_0^3\frac{d^3N(1,0)}{dp^3}]^Z[\frac{4\pi}{3}P_0^3\frac{d^3N(0,1)}{dp^3}]^N \\
&= \frac{1}{N!Z!}(\frac{4\pi}{3}P_0^3)^A[\frac{d^3N(1,0)}{dp^3}]^Z[\frac{d^3N(0,1)}{dp^3}]^N. \qquad \text{(F.15)}
\end{aligned}
$$

We have used the relation Eq. (F.10) for proton and neutron respectively. Since the neutron distributions typically are not measured, we assume that they have the same shapes as the proton distributions but are weighted by the N/Z ratio of the composite system

$$
\frac{d^3N(0,1)}{dp^3} = \frac{N_p + N_t}{Z_p + Z_t}\frac{d^3N(1,0)}{dp^3} = R_{np}\frac{d^3N(1,0)}{dp^3}, \qquad \text{(F.16)}
$$

where $R_{np} = \frac{N_p+N_t}{Z_p+Z_t}$. Then

$$
\begin{aligned}
\langle P(Z,N)\rangle &= \frac{1}{N!Z!}(\frac{4\pi}{3}P_0^3)^A[\frac{d^3N(1,0)}{dp^3}]^Z[\frac{d^3N(0,1)}{dp^3}]^N \\
&= \frac{1}{N!Z!}(\frac{4\pi}{3}P_0^3)^A[\frac{d^3N(1,0)}{dp^3}]^Z[R_{np}\frac{d^3N(1,0)}{dp^3}]^N \\
&= R_{np}^N\frac{1}{N!Z!}(\frac{4\pi}{3}P_0^3)^A[\frac{d^3N(1,0)}{dp^3}]^A. \qquad \text{(F.17)}
\end{aligned}
$$

The momentum distribution of cluster (Z, N) is

$$
\frac{d^3N(Z,N)}{dp_A^3} = \frac{\langle P(Z,N)\rangle}{\frac{4\pi}{3}P_0^3} = R_{np}^N\frac{1}{N!Z!}(\frac{4\pi}{3}P_0^3)^{A-1}[\frac{d^3N(1,0)}{dp^3}]^A. \qquad \text{(F.18)}
$$

where we assume $p_A = Ap$.

F.2.2 Coalescence Model with Coulomb Correction

The energies of particles we measured in experiment include the Coulomb contribution. Then

$$\frac{p_A^2}{2mA} = \frac{p_{A_0}^2}{2mA} + ZE_C, \tag{F.19}$$

where E_C is the Coulomb energy per unit charge of the composite particle, p_{A_0} is the momentum of the composite particle at the nuclear surface and p_A is the momentum of particle in the laboratory [271]. Then we have

$$p_{A_0} = p_A(1 - \frac{2mAZE_C}{p_A^2})^{1/2}, \tag{F.20}$$

$$p_{A_0}dp_{A_0} = p_A dp_A. \tag{F.21}$$

Therefore

$$\begin{aligned}
\frac{d^3N(Z,N)}{dp_{A_0}^3} &= \frac{d^2N(Z,N)}{p_{A_0}^2 dp_{A_0} d\Omega_{A_0}} \\
&= \frac{d^2N(Z,N)}{p_{A_0}p_{A_0} dp_{A_0} d\Omega_{A_0}} \\
&= \frac{d^2N(Z,N)}{p_A(1-\frac{2mAZE_C}{p_A^2})^{1/2} p_A dp_A d\Omega_A} \\
&= \frac{d^2N(Z,N)}{(1-\frac{2mAZE_C}{p_A^2})^{1/2} p_A^2 dp_A d\Omega_A}.
\end{aligned} \tag{F.22}$$

It is assumed that the Coulomb field doesn't change the angular distribution $d\Omega_{A_0} = d\Omega_A$. Since

$$E_A = \frac{p_A^2}{2mA}, \tag{F.23}$$

we have

$$p_A = \sqrt{2mAE_A}, \quad dp_A = \sqrt{2mA}\frac{dE_A}{2\sqrt{E_A}}. \tag{F.24}$$

Substituting Eq. (F.24) into Eq. (F.22), we obtain

$$\begin{aligned}\frac{d^3N(Z,N)}{dp_{A_0}^3} &= \frac{d^2N(Z,N)}{(1-\frac{2mAZE_C}{p_A^2})^{1/2}p_A^2dp_Ad\Omega_A} \\ &= \frac{d^2N(Z,N)}{(1-\frac{ZE_C}{E_A})^{1/2}2mAE_A\sqrt{2mA}\frac{dE_A}{2\sqrt{E_A}}d\Omega} \\ &= \frac{d^2N(Z,N)}{[2m^3(E_A-ZE_C)]^{1/2}A^{3/2}dE_Ad\Omega} \\ &= \frac{1}{[2m^3(E_A-ZE_C)]^{1/2}A^{3/2}}\frac{d^2N(Z,N)}{dE_Ad\Omega}. \end{aligned} \tag{F.25}$$

For the protons with Coulomb correction, we have

$$\frac{d^3N(1,0)}{dp_0^3} = \frac{1}{[2m^3(E-E_C)]^{1/2}}\frac{d^2N(1,0)}{dEd\Omega}. \tag{F.26}$$

In the coalescence model, we have Eq. (F.18)

$$\begin{aligned}\frac{d^3N(Z,N)}{dp_{A_0}^3} &= R_{np}^N\frac{1}{N!Z!}(\frac{4\pi}{3}P_0^3)^{A-1}[\frac{d^3N(1,0)}{dp_0^3}]^A \\ &= R_{np}^N\frac{1}{N!Z!}(\frac{4\pi}{3}P_0^3)^{A-1}\Big[\frac{1}{[2m^3(E-E_C)]^{1/2}}\frac{d^2N(1,0)}{dEd\Omega}\Big]. \end{aligned} \tag{F.27}$$

Comparing Eq. (F.25) with Eq. (F.27), we obtain

$$\frac{1}{[2m^3(E_A-ZE_C)]^{1/2}A^{3/2}}\frac{d^2N(Z,N)}{dE_Ad\Omega} = R_{np}^N\frac{1}{N!Z!}(\frac{4\pi}{3}P_0^3)^{A-1}\Big[\frac{1}{[2m^3(E-E_C)]^{1/2}}\frac{d^2N(1,0)}{dEd\Omega}\Big]^A. \tag{F.28}$$

Since we have

$$E_A - ZE_C = E_{A_0} = \frac{p_{A_0}^2}{2mA} = A\frac{p_0^2}{2m} = AE_0 = A(E-E_C). \tag{F.29}$$

We can rewrite Eq. (F.28) as

$$\begin{aligned}\frac{d^2N(Z,N)}{dE_Ad\Omega} &= [2m^3(E_A-ZE_C)]^{1/2}A^{3/2}R_{np}^N\frac{1}{N!Z!}(\frac{4\pi}{3}P_0^3)^{A-1}\Big[\frac{1}{[2m^3(E-E_C)]^{1/2}}\frac{d^2N(1,0)}{dEd\Omega}\Big]^A \\ &= [2m^3(E-E_C)]^{1/2}A^2R_{np}^N\frac{1}{N!Z!}(\frac{4\pi}{3}P_0^3)^{A-1}\Big[\frac{1}{[2m^3(E-E_C)]^{1/2}}\frac{d^2N(1,0)}{dEd\Omega}\Big]^A \\ &= R_{np}^N\frac{A^2}{N!Z!}\Big\{\frac{\frac{4\pi}{3}P_0^3}{[2m^3(E-E_C)]^{1/2}}\Big\}^{A-1}\Big[\frac{d^2N(1,0)}{dEd\Omega}\Big]^A. \end{aligned} \tag{F.30}$$

If we define $P_0' = P_0A^{\frac{1}{A-1}}$, then we can write Eq. (F.30) into the form used in literature

$$\frac{d^2N(Z,N)}{dE_Ad\Omega} = R_{np}^N\frac{1}{N!Z!A}\Big\{\frac{4\pi P_0'^3}{3[2m^3(E-E_C)]^{1/2}}\Big\}^{A-1}\Big[\frac{d^2N(1,0)}{dEd\Omega}\Big]^A. \tag{F.31}$$

F.2.3 The Relation between P_0 and V

From section F.1, we have

$$N(A,Z) = V\omega(A,Z)\frac{A^{3/2}}{\lambda_T^3}e^{\frac{\mu(A,Z)}{T}}, \tag{F.32}$$

and

$$\omega(A,Z) = \sum_i(2s_i(A,Z)+1)e^{-\frac{E_i(A,Z)}{T}}, \quad \mu(A,Z) = Z\mu_{pF} + (A-Z)\mu_{nF} + B(A,Z). \tag{F.33}$$

The details are given in section F.1. Therefore we have

$$N(1,0) = V\frac{2}{\lambda_T^3}e^{\frac{\mu_{nF}}{T}}, \quad N(1,1) = V\frac{2}{\lambda_T^3}e^{\frac{\mu_{pF}}{T}}. \tag{F.34}$$

Then we can write Eq. (F.32) as

$$\begin{aligned} N(A,Z) &= V\omega(A,Z)\frac{A^{3/2}}{\lambda_T^3}e^{\frac{\mu(A,Z)}{T}} \\ &= V\omega(A,Z)\frac{A^{3/2}}{\lambda_T^3}e^{\frac{Z\mu_{pF}+(A-Z)\mu_{nF}+B(A,Z)}{T}} \\ &= V\omega(A,Z)\frac{A^{3/2}}{\lambda_T^3}e^{\frac{B(A,Z)}{T}}e^{\frac{Z\mu_{pF}}{T}}e^{\frac{(A-Z)\mu_{nF}}{T}} \\ &= V\omega(A,Z)\frac{A^{3/2}}{\lambda_T^3}e^{\frac{B(A,Z)}{T}}[\frac{N(1,1)\lambda_T^3}{2V}]^Z[\frac{N(1,0)\lambda_T^3}{2V}]^N \\ &= \omega(A,Z)A^{3/2}e^{\frac{B(A,Z)}{T}}\frac{1}{2^A}(\frac{\lambda_T^3}{V})^{A-1}N(1,1)^ZN(1,0)^N \\ &= R_{np}^N\omega(A,Z)A^{3/2}e^{\frac{B(A,Z)}{T}}\frac{1}{2^A}(\frac{\lambda_T^3}{V})^{A-1}N(1,1)^A. \end{aligned} \tag{F.35}$$

The particles are following Maxwell-Boltzmann distribution

$$\frac{d^3N(A,Z)}{dp_A^3} = N(A,Z)\frac{1}{(2\pi AmT)^{3/2}}e^{-E_A/T}, \tag{F.36}$$

$$\frac{d^3N(1,1)}{dp^3} = N(1,1)\frac{1}{(2\pi mT)^{3/2}}e^{-E/T}. \tag{F.37}$$

Therefore we have

$$\begin{aligned} \frac{d^3N(A,Z)}{dp_A^3} &= N(A,Z)\frac{1}{(2\pi AmT)^{3/2}}e^{-E_A/T} \\ &= R_{np}^N\omega(A,Z)A^{3/2}e^{\frac{B(A,Z)}{T}}\frac{1}{2^A}(\frac{\lambda_T^3}{V})^{A-1}N(1,1)^A\frac{1}{(2\pi AmT)^{3/2}}e^{-E_A/T} \\ &= R_{np}^N\omega(A,Z)e^{\frac{B(A,Z)}{T}}\frac{1}{2^A}(\frac{\lambda_T^3}{V})^{A-1}[(2\pi mT)^{3/2}]^{A-1}[N(1,1)\frac{1}{(2\pi mT)^{3/2}}e^{-E/T}]^A \\ &= R_{np}^N\omega(A,Z)e^{\frac{B(A,Z)}{T}}\frac{1}{2^A}(\frac{h^3}{V})^{A-1}\Big[\frac{d^3N(1,1)}{dp^3}\Big]^A. \end{aligned} \tag{F.38}$$

We have used the assumption

$$p_A = Ap, \tag{F.39}$$

$$E_A = \frac{p_A^2}{2mA} = A\frac{p^2}{2m} = AE. \tag{F.40}$$

If we ignore the excited states, then

$$\omega(A, Z) = 2s_A + 1, \tag{F.41}$$

$$\frac{d^3N(A, Z)}{dp_A^3} = R_{np}^N \frac{2s_A + 1}{2^A} e^{\frac{B(A,Z)}{T}} (\frac{h^3}{V})^{A-1} [\frac{d^3N(1, 1)}{dp^3}]^A. \tag{F.42}$$

Comparing Eq. (F.18) with Eq. (F.42), we obtain

$$\frac{1}{N!Z!}(\frac{4\pi}{3}P_0^3)^{A-1} = \frac{2s_A + 1}{2^A} e^{\frac{B(A,Z)}{T}} (\frac{h^3}{V})^{A-1}. \tag{F.43}$$

Solving for V, we obtain

$$V = [\frac{N!Z!}{2^A}(2s_A + 1)e^{\frac{B(A,Z)}{T}}]^{1/(A-1)} \frac{3h^3}{4\pi P_0^3}. \tag{F.44}$$

Using the relation $P_0' = P_0 A^{\frac{1}{A-1}}$, we can obtain the form used in the literature

$$V = [\frac{N!Z!A^3}{2^A}(2s_A + 1)e^{\frac{B(A,Z)}{T}}]^{1/(A-1)} \frac{3h^3}{4\pi P_0'^3}. \tag{F.45}$$